Title

Designing Active Electro-Catalysts and Reactors for Electrochemical CO$_2$ Transformation

Permalink

https://escholarship.org/uc/item/8rk4g5vp

Author

Kim, Taewoo

Publication Date

2022

UNIVERSITY OF CALIFORNIA SAN DIEGO

Designing Active Electro-Catalysts and Reactors for Electrochemical CO_2 Transformation

A dissertation submitted in partial satisfaction of the
requirements for the degree Doctor of Philosophy

in

Chemical Engineering

by

Taewoo Kim

Committee in charge:

Professor David P. Fenning, Chair
Professor Zheng Chen
Professor Clifford P. Kubiak
Professor Andrew C. Kummel
Professor Ping Liu

2022

The Dissertation of Taewoo Kim is approved, and it is acceptable in quality and form for publication on microfilm and electronically.

University of California San Diego

2022

TABLE OF CONTENTS

LIST OF FIGURES

LIST OF TABLES

ACKNOWLEDGEMENTS

First of all, I would like to thank my advisor, Professor David P. Fenning, for the continuous support of my PhD journey, his patience, trust, motivation, enthusiasm, and immense knowledge. His guidance helped me in all the time of research and made this dissertation possible. He was always there whenever I got lost in my research and encouraged me to be motivated again. Besides my advisor, I would like to thank the rest of my thesis committee: Prof. Zheng Chen, Prof. Clifford P. Kubiak, Prof. Andrew C. Kummel, and Prof. Ping Liu, for their insightful comments on my research that helped a lot to strengthen my thesis.

Secondly, I would like to express my deep appreciation to all of my past and current colleagues in the Fenning lab and at UC San Diego, in no particular order: Grace Luo, Rishi Kumar, Vivek Devalla, Sara Dorr, Pedra Abbassi, Isabel Albelo, Moses Kodur, Deniz Cakan, Wayne Neilson, Rajasekhar Medapalli, and Jeffrey Brock. You are so talented and kind enough to save me and help me whenever I feel I am lost.

Finally, I would like to thank my family for their endless support and understanding. I also want to thank my friends, in no particular order: Hyunchul Jung, Jihyun Jang, Jungwha Hong, Gayea Hyun, Myeong Hwan Lee, Hyun Ko, Min-cheol Kim, Hyojung Yoon, Jin Yu, Junhee Park, Woojin Choi, Jungming Ha, Jungho Ha, Byoung-Sun Lee, Minjae Jung, Yikyung Yu, my previous advisor prof. Seong-Hyun Baeck, and my mentor Yong-il Choi.

Chapter 2, in full, is a reprint of the material ”How Strain Alters CO_2 Electroreduction on Model Cu Surfaces” as it appears in ACS Catalysis, Taewoo Kim, Rishi E. Kumar, Jeffrey A. Brock, Eric E. Fullerton, and David P. Fenning, 2021, 11 (11), 6662. The dissertation author was the primary investigator and author of this material.

Chapter 3, in full, is a reprint of the material ”Enhancing C_2–C_3 Production from CO_2 on Copper Electrocatalysts via a Potential-Dependent Mesostructure” as it appears in ACS Applied Energy Materials, Taewoo Kim, Alireza Kargar, Yanqi Luo, Ragad Mohammed, Erick Martinez-Loran, Aditi Ganapathi, Priyasha Shah, and David P. Fenning, 2018, 1 (5), 1965. The dissertation author was the primary investigator and author of this material.

Chapter 4, in part, is currently being prepared for submission for publication of the material ”Tuning oxidation state of Sn oxides for electrochemical CO_2 to formate conversion in the catholyte–free electrolzyer”, Taewoo Kim, Vivek S. Devalla, Sean P. Dunfield, Sara Dorr, Moses Kudor, and David P. Fenning. The dissertation author was one of the primary investigators and author of this material.

VITA

2006-2014	B.S. in Chemical Engineering, Inha University, Incheon, South Korea
2014-2016	M.E. in Chemical Engineering, Inha University, Incheon, South, Korea
2016-2022	Ph.D. in Chemical Engineering, University of California San Diego, CA, USA

PUBLICATIONS

T. Kim, V. S. Devalla, S. P. Dunfield, S. Dorr, M. Kudor, D. P. Fenning, ”Tuning oxidation state of Sn oxides for electrochemical CO_2 to formate conversion in the catholyte–free electrolzyer” *in preparation*

P. Abbasi, M. R. Barrone, M. P. C. Jauregui, D. V. Padilla, H. Paik, **T. Kim**, L. Kornblum, D. G. Schlom, T. A. Pascal, D. P. Fenning, ”Ferroelectric Modulation of Surface Electronic States in $BaTiO_3$ for Enhanced Hydrogen Evolution Activity,” *Nano Letters*, 22 (10), 4276, 2022

M. Kodur, Z. Dorfman, R. A. Kerner, J. H. Skaggs, **T. Kim**, S. P. Dunfield, A. Palmstrom, J. J. Berry, D. P. Fenning, ”Electrochemical Screening of Contact Layers for Metal Halide Perovskites,” *ACS Energy Letters*, 7 (2), 683, 2022

T. Kim, R. E. Kumar, J. A. Brock, E. E. Fullerton, D. P. Fenning, ”How Strain Alters CO_2 Electroreduction on Model Cu(001) Surfaces,” *ACS Catalysis*, 11 (11), 6662, 2021

C. M. Coaty, A. A. Corrao, V. Petrova, **T. Kim**, D. P. Fenning, P. G. Khalifah, P. Liu, ”Anisotropic nanoporous morphology of ZnO-supported Co that enhances catalytic activity,” *Nanoscale*, 13, 8242, 2021

T. Kim†, A. Kargar†, Y. Luo, R. Mohammed, E. M. Loran, A. Ganapathi, P. Shah, D. P. Fenning, ”Enhancing C_2–C_3 Production from CO_2 on Copper Electrocatalysts via a Potential-Dependent Mesostructure,” *ACS Applied Energy Materials*, 1 (5), 1965, 2018 (†- co-first author)

Before UC San Diego

T. Kim, G. P. Kim, J. Jang, S. E. Shim, W. S. Ahn, S. H. Baeck, ”Electrochemical Oxidation of Organic Matter in the Presence of Chloride Over Ti/SnO_2–Sb_2O_5 Prepared via Sol–Gel Methods,” *Journal of Nanoscience and Nanotechnology*, 16 (10), 10892, 2016

I. Park, **T. Kim**, H. Park, M. Mun, S. E. Shim, S. H. Baeck, ”Preparation and Electrochemical Properties of Pt–Ru/Mn_3O_4/C Bifunctional Catalysts for Lithium-Air Secondary Battery,” *Journal of Nanoscience and Nanotechnology*, 16 (10), 10453, 2016

J. Jang, **T. Kim**, Y. I. Choi, I. Park, D. Lim, S. E. Shim, S. H. Baeck, ”Preparation and Characterization of Nanostructured Manganese Oxide for Supercapacitors,” *Journal of Nanoscience and Nanotechnology*, 16 (5), 5195, 2016

H. Hwang, D. Lim, **T. Kim**, D. Lee, S. E. Shim, S. H. Baeck, ”Electro-Catalytic Activity of RuO_2–IrO_2–Ta_2O_5 Mixed Metal Oxide Prepared by Spray Thermal Decomposition for Alkaline Water Electrolysis,” *Journal of Nanoscience and Nanotechnology*, 16 (5), 4405, 2016

T. Kim, G. P. Kim, J. Jang, S. E. Shim, W. S. Ahn, S. H. Baeck, ”An investigation on the selective hydrodealkylation of C_9^+ aromatics over alkali-treated Pt/H-ZSM-5 zeolites,” *Catalysis Science Technology*, 6, 5599, 2016

T. Kim, H. Hwang, J. Jang, I. Park, S. E. Shim, S. H. Baeck, ”Synthesis and Electrochemical Analyses of Manganese Oxides for Super-Capacitors,” *Journal of Nanoscience and Nanotechnology*, 15 (11), 8890, 2015

D. Lim, J. Jang, **T. Kim**, S. E. Shim, S. H. Baeck, ”Selective hydrodealkylation of C_9^+ aromatics to benzene, toluene, and xylenes (BTX) over a Pt/H-ZSM-5 catalyst,” *Journal of Molecular Catalysis A: Chemical*, 407, 147, 2015

D. Lim, H. Hwang, **T. Kim**, S. E. Shim, S. H. Baeck, ”Fabrication and Characterization of Amorphous Cobalt-Doped Molybdenum Sulfide for Hydrogen Evolution Reaction,” *Journal of Nanoscience and Nanotechnology*, 15 (10), 8257, 2015

I. Park, J. Jang, D. Lim, **T. Kim**, S. E. Shim, S. H. Baeck, ”Synthesis and Characterizations of $Mn_1 + XCo_2 - XO_4$ Solid Solution Catalysts for Highly Efficient Li/Air Secondary Battery,” *Journal of the Korean Electrochemical Society*, 18 (4), 137, 2015

ABSTRACT OF THE DISSERTATION

Designing Active Electro-Catalysts and Reactors for Electrochemical CO_2 Transformation

by

Taewoo Kim

Doctor of Philosophy in Chemical Engineering

University of California San Diego, 2022

Professor David P. Fenning, Chair

Electrochemical CO_2 conversion into value-added chemical feedstocks, if powered with renewable electricity, is a promising path to approach carbon neutrality. However, developing active and selective catalysts is necessary to enable energy efficient conversion. In this thesis, I provide strategies to design active electrocatalysts with enhanced selectivity for CO_2 electrolysis via tuning of the local reaction environment. First, I show that modulating the surface strain of a model Cu (001) catalyst epitaxially grown on a single-crystal Si substrate results in an increase of the Cu 3*d* band center position. This change in the electronic structure causes a suppression of the CO production pathway, increasing selectivity to multi-carbon products. I demonstrate that multi-carbon products can be further selected for by an operando restructuring of the micro- and

nanoscale morphology of Cu-based catalysts. An electrochemically reduced $Cu(OH)_2$ nanowire catalyst enhances the selectivity of multi-carbon products at moderate electrolysis potentials where a hierarchical morphology evolves. A final level is the tuning of the chemical state of the catalyst surface. By switching the initial surface oxidation state of tin oxide catalysts to be Sn^{II}-rich, the selectivity and energy efficiency of formate generation are promoted, offering a possible nearest-term path to carbon-negative CO_2 electrolysis. Optimizing electrolyzer design is also crucial to facilitate mass transport of CO_2 to reach industrial relevance. The importance of the mass transport of CO_2 to enhance overall activity is also demonstrated by controlling flow rate of partially concentrated CO_2 stream. These findings reveal the importance of surface strain, morphology and chemical state on designing efficient CO_2 catalysts, providing fundamental guidelines and direction toward carbon neutral CO_2 conversion.

Chapter 1

Introduction

1.1 A Brief Introduction to Electrochemical CO_2 Transformation

According to NASA, the global surface temperature has been increased as compared to the 1950-1980 average temperatures as shown in Figure 1.1A.[1] Comparing the increase in the global temperature and the trend in the atmospheric CO_2 concentration observed at Mauna Loa observatory (Figure 1.1B)[2] highlights the fact that the amount of atmospheric CO_2 is critically co-related to the global warming. The electrochemical conversion of CO_2 to carbonaceous chemicals is a potential strategy to mitigate global warming with an advantage of readily accessible renewable energy.[3, 4, 5] The electrochemical CO_2 reduction in aqueous media can produce variety of carbonaceous chemicals from single-carbon products (CO, HCOOH, and CH_4) to multi-carbon products (C_2H_4, acetate, EtOH, and n-PrOH). Those anticipated products from the process have benefits of high volumetric energy density and facile integration with current industrial infrastructure that enables to accommodate the greater need of carbon-based feedstocks that helps to achieve net negative carbon emission.[6, 7, 8] Also, coupling it with renewable energy can use chemical bonds as a medium to store the intermittent energy and perhaps leads to economic benefits. According to California Independent System Operator (ISO), the emerging penetration of renewable energy into the grid system occasionally lowers the price of the electricity and the price temporarily becomes negative during the daytime where high

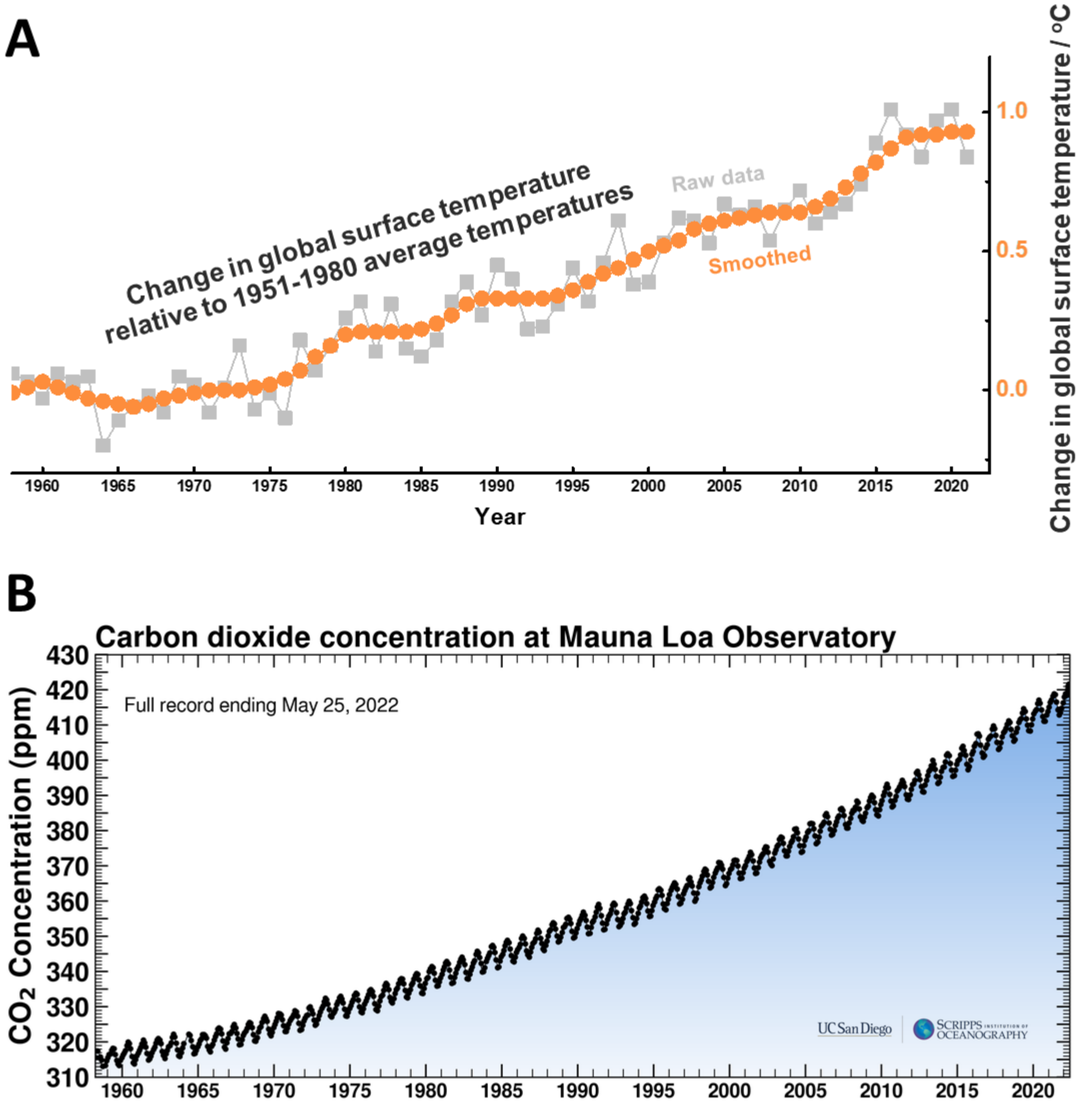

Figure 1.1. Changes in (A) the global surface temperature and (B) atmospheric CO_2 amount.[1, 2]

penetration of renewables to the grid system appears.[9] The recent techno-economic-analysis foresees the impact of electrochemical CO_2 reduction on global warming.[10] According to the study, current production of carbon-based feedstocks from fossil-based sources are one of main sources of CO_2 emission, which indicates a great impact of e-synthesized chemicals on carbon neutrality. In case of producing multi-carbon products (e.g., C_2H_4 and EtOH), an attractive economic benefit is expected from their global market size of \$230 and \$75 billions, along with possible reduction of 860 and 550 metric tons of CO_2 emissions if produced via electrochemical approach, respectively. However, due to their high energy densities, producing multi-carbon compounds from electrochemical CO_2 conversion requires significant energy input from the existing grid system, which is detrimental to the carbon neutrality. In this context, single carbon products generation (e.g., formate and CO) might be an alternative way to achieve carbon neutrality as they requires less energy and if no further penetration of the renewables to the grid system is expected. De luna et al.[10] speculates that increasing energy efficiency of the CO_2 conversion system is the most important toward carbon neutrality. Increasing selectivity and lowering kinetic overpotential of the CO_2 reduction reaction are critical to improve the overall energy efficiency since it is a function of selectivity (Faradaic efficiency) and cell voltage ($E_{cathode}$–E_{anode}). To achieve those goals, designing active catalysts and optimizing electrolyzer are necessary steps, and they will be discussed in the following sections.

1.2 Designing CO_2 Conversion Catalysts

Electrochemical CO_2 reduction involves multiple reaction pathways.[11] Similar to the electrochemical hydrogen evolution[12], electrochemical CO_2 conversion also sensitive to the reaction intermediates and their binding energy to the catalyst surface. To enhance CO_2 conversion activities in terms of current density, an optimal binding energy of the key reaction intermediate is important. In general, it is suggested that the first intermediate of CO_2 reduction is either *COOH or *OCHO, as shown in Figure 1.2, and the entire reaction path is determined

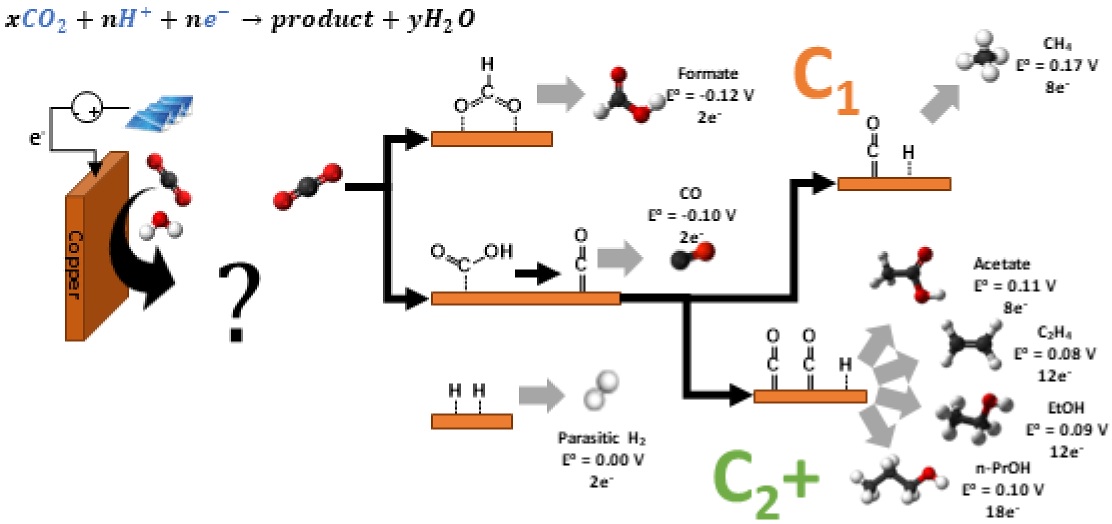

Figure 1.2. Scheme of the electrochemical CO_2 reduction pathways.

whether CO_2 is bound to the surface with carbon atom or oxygen atom. If starts with oxygen bound intermediate, *OCHO, CO_2 reduction is directed to the formate generation, and it is widely suggested that *OCHO is a key reaction intermediate for formate generation. Among transition metals, Sn, Bi, In, and Pb tend to preferably bind *OCHO instead *COOH, resulting in high preference of formate generation. In case CO_2 binds with carbon atom, *COOH, the transition from *COOH to *CO occurs quickly. Toward highly energy dense products, binding energy of *CO takes important role as it determines the rest of reaction paths. As *CO binds weakly on the catalyst surface, *CO is readily released as a final products, CO, and this appears on the surface of Ag and Au. If *CO binds to the surface extremely strong, further reduction is substantially suppressed due to the surface poisoning. Among other transition metals, Cu is capable of producing value-added products such as hydrocarbons and oxygenates owing to its moderate adsorption energy to *CO, while its poor selectivity is a main challenge to overcome.[4, 13, 14, 15] Among Cu-based catalysts, defect abundant surface with enriched strong *CO binding sites have been reported to show a correlation with CO_2 reduction selectivity to multi-carbon products.[16, 17] Strong *CO adsorption is accompanied with an increase in its surface population that promotes CO-CO dimerization to form *COCO intermediate.[18] In

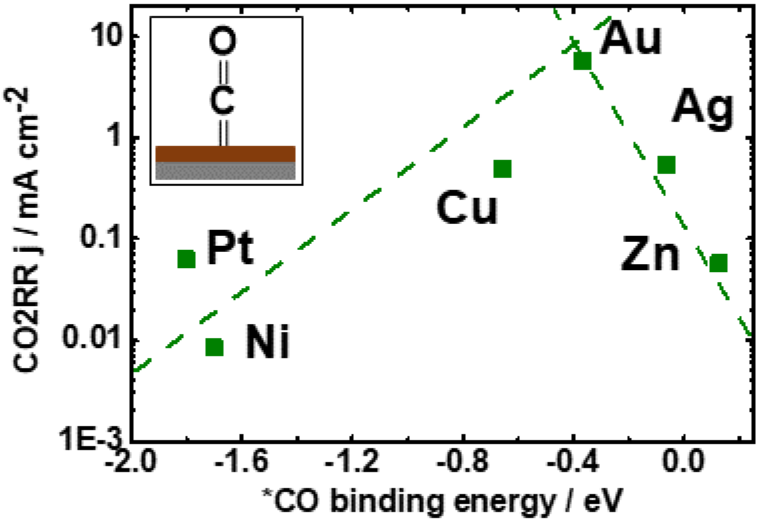

Figure 1.3. *CO binding energy dependency of CO_2 reduction reaction.[14]

the mean time, parasitic hydrogen evolution is inevitable as the most of CO_2 electrolysis system involves aqueous medium.

As mentioned in the above section, the ultimate goal toward carbon neutrality is to increase overall energy efficiency of the CO_2 conversion system, and this requires designing active electrode catalysts. In this section, I briefly introduce three strategies that enhance selectivity, lowers kinetic barrier, increase activities. First, Tuning *CO binding energy on Cu surface can be a way to enhance selectivity toward multi-carbon products. As shown in Figure 1.3, overall CO_2 reduction reaction has volcano-type relationship with *CO binding energy. To promote multi-carbon products selectivity, I hypothesize that non-optimized *CO binding energy on Cu induces poor selectivity. However, tuning *CO binding energy is not the first idea. Electrodeposited polycrystalline Cu thin layer on polycrystalline Pt substrate shows inhibited CH_4 production while favorable C-C bond formation.[19] It is assumed that surface lattice tensile strain between Cu film and Pt substrate may induce the change in the adsorption energy of essential intermediates. Nanoparticle synthesis provides ample opportunity for developing strained surfaces. Pd icosahedra nanoparticle experiences tensile strain on its surface that induces decreased Gibbs free energy of *COOH formation, resulting in increased CO formation.[20]

Examining the electrochemical CO stripping voltammetry reveals the increased adsorption of *CO in the presence of tensile strain in the nanoparticle. However, one of the practical challenges to understanding the effect of changing adsorption energy of *CO on CO_2 reduction activity is that there are difficulties to exclude geometric contributions in the experimental conditions such as surface defect, surface roughness, and nanoparticles. In Chapter 2, I will discuss this in detail.

Secondly, structuring surface morphology of Cu can enhance overall CO_2 reduction activity.[5] Besides atomically flat surface, the structured morphology can provides abundant defects such as undercoordinated sites on the high index facets, nanoscale transport of the reaction intermediates within pore structure along with the increased retention time, and increasing local pH due to limited mass transport of proton, which are favorable reaction environment for multi-carbon products formation. Cu nanoparticles with rough surfaces show higher ratio of multi-carbon products to single carbon products formation than planar Cu surfaces.[21]. Electrochemically deposited Cu with high surface area also shows possibility of improving multi-carbon products generation.[22]. Also, the nanowire morphology seems to be an optimal surface structure toward multi-carbon products generation.[23] In Chapter 3, I will discuss the effect of hierarchical surface morphology derived from electrochemically reduced $Cu(OH)_2$ nanowires on overall CO_2 conversion efficiency.

Lastly, chemical state of the Sn oxides takes an important role to enhance selectivity toward formate. Sn is one of the most active transition metals showing CO_2-to-formate conversion.[24] The Sn oxides seems to be necessary to avoid parasitic hydrogen evolution and to enhance overall selectivity toward CO_2 reduction products as compared to the metallic Sn.[25] The improved CO_2 conversion to formate is demonstrated as Sn monoxide is co-existed with Sn dioxides.[26] In Chapter 4, I will discuss the importance of the initial oxidation state of the thermally evaporated Sn oxides for CO_2 conversion to formate.

1.3 The CO_2 Electrolysis System

For decades, most of efforts are made to unravel fundamental understandings on reaction mechanisms and parameters of catalyst design in conventional aqueous-phase batch-type CO_2 conversion reactors. In general, the batch-type CO_2 conversion reactors are consisting of three electrodes system with a working electrode (cathode), a reference electrode, and a counter electrode (anode). Figure 1.4 shows a scheme of the half of the reactor. Electrolyte is split into catholyte and anolyte separated by membrane. A thin polymeric sheet with ion channels toward either cation or anion is used as membrane. In my Ph.D. research, especially for the batch-type reactor, a Ag/AgCl(KCl gel) electrode (low profile, 3.5 mm OD, 74 mm length, Pine research) and platinum gauze (100 mesh, 99.9% metal basis, Sigma-Aldrich) is used as a reference electrode and a counter electrode, respectively. Also, anion exchange membrane (AEM, Selemion) is mainly used as it was confirmed that cation exchange membrane (CEM, Nafion) gave high ohmic resistance from the preliminary test in the lab. A conductive planar sheet is used as current collector and substrate for cathode where catalytic materials are grown/coated on the surface. CO_2 is continuously supplied into the electrolyte to maximize CO_2 availability to the catalytic sites.

Given low solubility of CO_2 in aqueous electrolyte ($\sim$34 mM), mass transport of CO_2 onto the catalytic sites is limited that gives substantial challenges to enhance catalytic activities in terms of current density. CO_2 conversion with a high current density is critical to meet industrial level performance where more than 500 mA cm^{-2} is required.[10] To overcome this obstacle, gas diffusion layer (GDL) is introduced to the electrolysis system. GDL is typically constructed by two layers: macro- and micro-porous layer.

The macro-porous layer consists of cross-linked carbon fibers, giving sufficient porosity where CO_2 gas can diffuse into the catalyst surface (Figure 1.5A). On top of the macro-porous layer, the micro-porous layer takes place and it consists of fine-size carbon particles with varying content of PTFE-coating (depending on the manufacturer) to control hydrophobicity, eventually

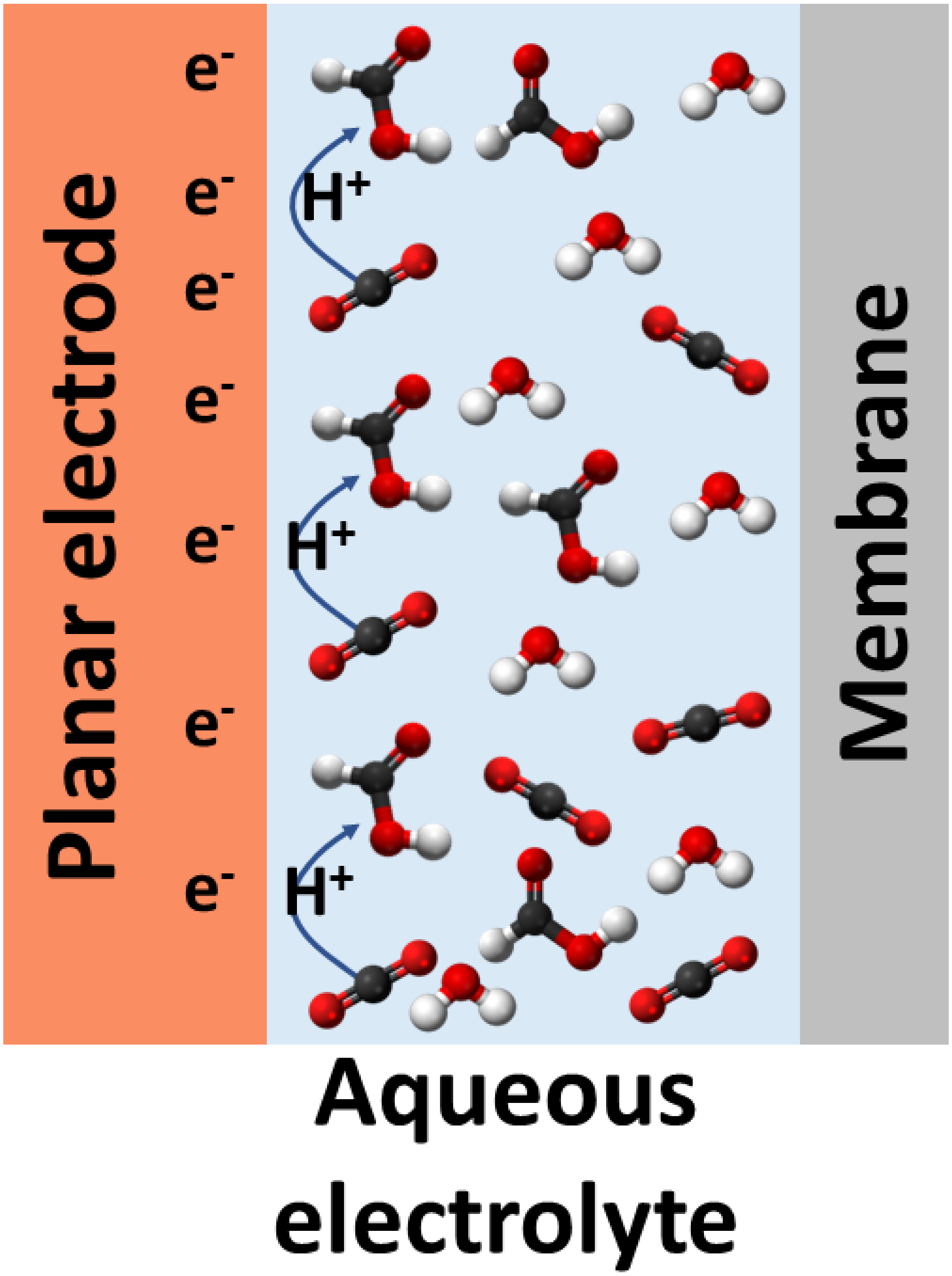

Figure 1.4. Scheme of half cell batch-type reactor consists of planar electrode, aqueous eletrolyte and membrane. The Conversion of CO_2 to formate is illustrated.

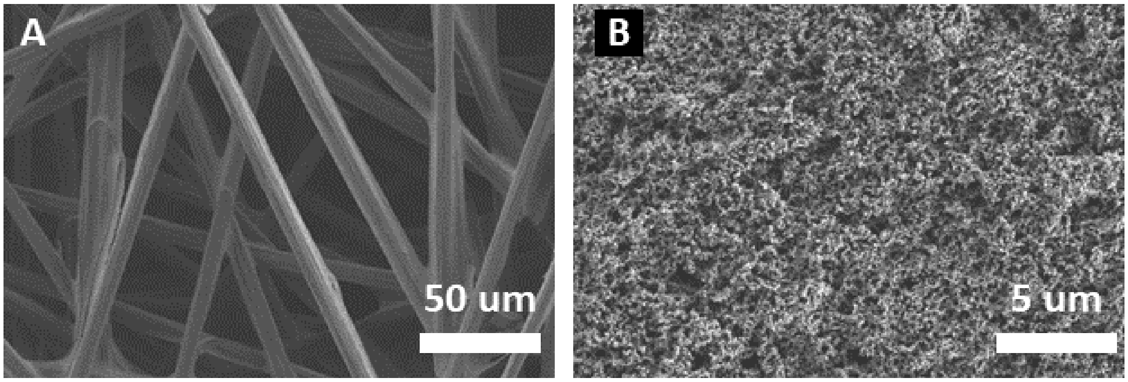

Figure 1.5. Scanning electron microscopy images of GDL surfaces. (A) Macro-porous layer (Toray carbon paper 060 with 10% PTFE content). (B) micro-porous layer (AvCarb GDS2230).

avoiding a flooding over long-term electrolysis (Figure 1.5B). Mass transport of CO_2 will be suppressed if the pore structure is blocked by water.

Gas diffusion electrode (GDE) is prepared after a layer of catalyst is coated on top of the GDL. A schematic of a GDE-incorporated electrolyzer is shown in Figure 1.6, which shows how gaseous CO_2 is supplied directly to the interface between a layer of catalyst and electrolyte. This configuration facilitates the rapid mass transport of CO_2 to the reaction site, where proton and electron are also engaged to complete the CO_2 reduction reaction. Although GDE promotes facile mass transport, this type of electrolyzer is limited to the gaseous products. If liquid products (i.e., formate, acetate, EtOH, or n-PrOH) are targeted, the presence of aqueous electrolyte remains diluted products which leads to additional seperation process.

In following section, I will briefly describe the batch-type electrolzyer and the GDE incorporated electrolyzer in the lab. Also, I will describe approaches to effectively quantify CO_2 reduction products that I have developed and used to study CO_2 reduction reaction during my Ph.D. research.

1.3.1 Batch-type Electrolysis Cell

Introduction to the Cell Compartments. The design of each polycarbonate compartment in Figure 1.7 (i.e., anolyte and catholyte chamber, cathode holder, glassy carbon disk

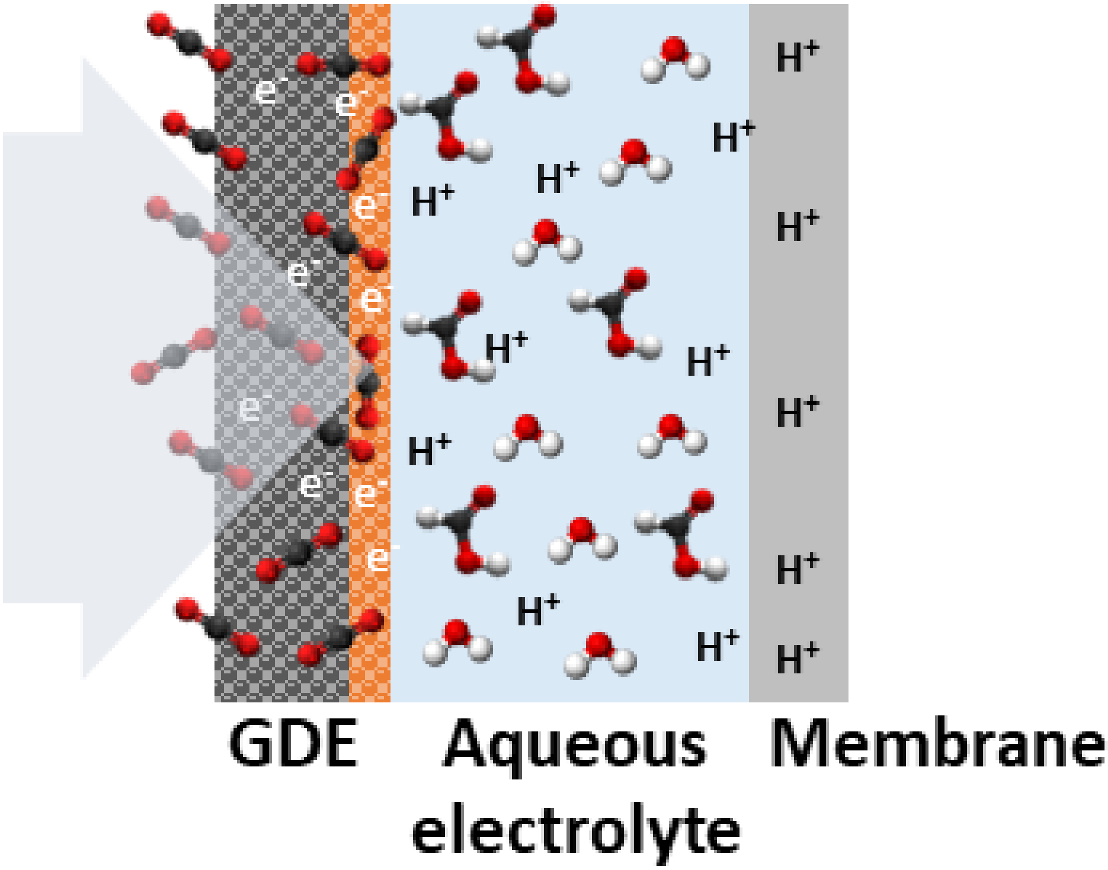

Figure 1.6. Scheme of a half cell electrolyzer with gas diffusion electrode incorporated. The Conversion of CO_2 to formate is illustrated. The membrane represents a cation exchange membrane.

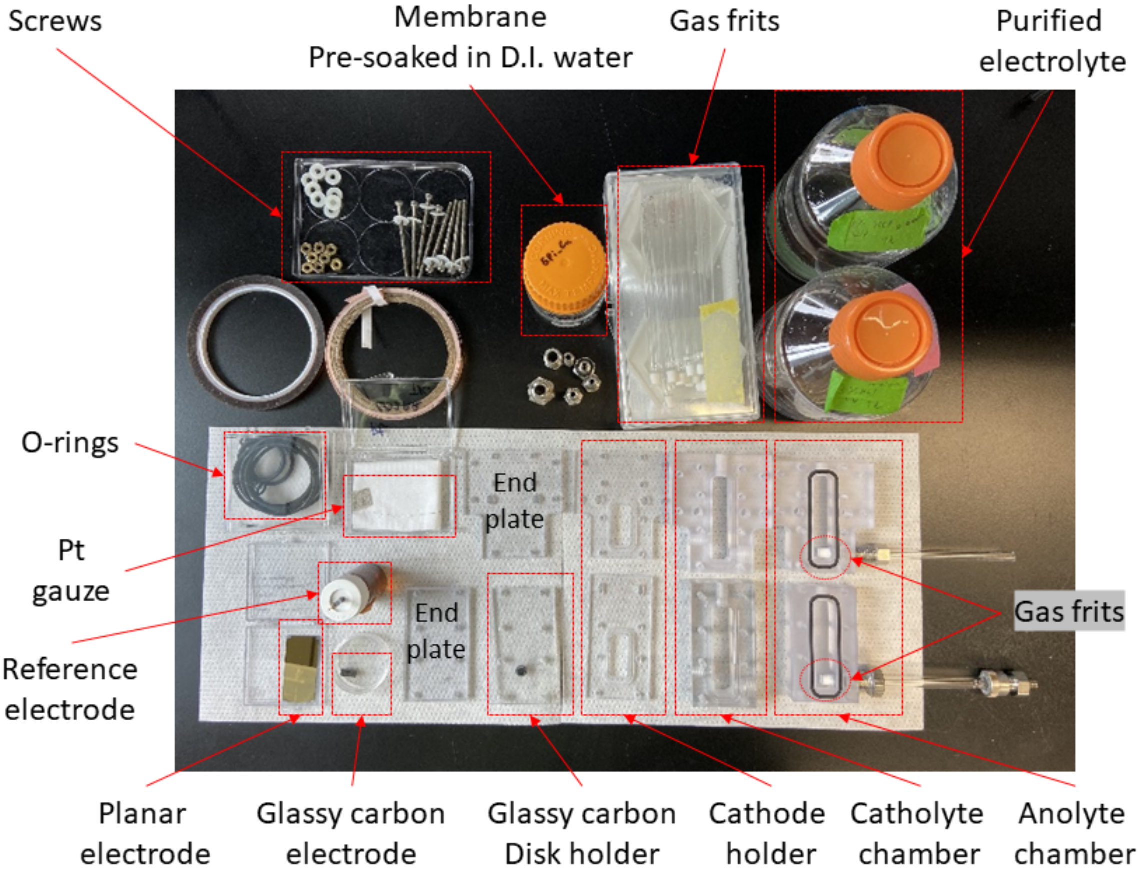

Figure 1.7. Components of the batch-type reactor in the lab.

holder, and end plates) are based on the previous work [4] and machined after modification. The polycarbonate is chosen since it has chemical compatibility with potassium bicarbonate with a range of pH from 6 to 8, which is used as electrolyte in the system. All of CO_2 electrolysis is performed with CO_2-saturated 0.1 M $KHCO_3$ solution as electrolyte. The pH of the electrolyte is changed from weak alkaline to weak acidic condition (from 8.2 to 6.8) after 30 min of CO_2 purging process. Purification of electrolyte prior to any CO_2 electrolysis is necessary to remove metallic impurities.

The electrolyte purification process takes 3 steps with regeneration of Chelex regin (product No. 1421253). To purify 250 ml of 0.1 M $KHCO_3$ solution, 9.38 g of Chelex regin is used. Chelex is regenerated in 1 M HCl solution for 12 hrs under vigorous stirring, followed by washing and filtering with 5 L of D.I. water and using 0.45 micron filter (Corning polystyrene) . Subsequently, the filtered regin is immersed in 1 M KOH solution at 60 °C for 24 hrs under vigorous stirring, and then washed and filtered again until the pH of the filtered solution reaches to neutral. During the 24 hours of stirring, a condenser is used to avoid change in concentration from any solvent evaporation. During the neutralizing process, the heated KOH solution should be cooled down to room temperature to facilitate the process. Finally, the purified 0.1 M$KHCO_3$ solution is prepared by mixing the as-prepared 0.1 M $KHCO_3$ solution with the regenerated Chelex regin for 24 hrs under vigorous stirring and subsequent filtering.

Dry CO_2 gas stream is fed into the catholyte chamber through gas dispersion tubes with fine size pores (5x135 mm, porosity E filter, Aceglass) to facilitate mass transport. The CO_2 gas feed is also supplied to the anolyte chamber to achieve pH balance.

Preparation of the cell components. The purity of the inside of the batch-type reactor is important to CO_2 electrolysis. Any trace amount of metal components from the previous electrolysis can be deteriorate for the next electrolysis. The CO_2 electrolysis of planar electrode with limited active site is sensitive to the trace amount of contaminant especially when Cu-based electrode is used as catalyst.[27] It is encouraged to clean the polycarbonate body with diluted 10 vol.% HCl solution at least an hour after each electrolysis. More than 3 hours of immersion of the polycarbonate body in the HCl solution may cause etching the surface, so should be avoided. Meanwhile, the gas dispersion tube from the catholyte chamber should be cleaned in the concentrated HCl solution (20 vol.%) for overnight. After cleaning in the HCl solution, there should be no residue acid solution on the cell body and the gas dispersion tube after rinsing them with D.I. water otherwise it causes critical changes in the reaction environment during the electrolysis.

Ensuring air-tightness of the electrolysis system is important to perform accurate quantification of the gas products and precise evaluation of the catalyst activity coupled with current density. To have leak-free system, tightening volts and nuts with evenly distributed torque securing each component is necessary to balance pressure throughout the cell. Digitized torque wrench is used to assemble the component in this consideration and 4.10 in–lb of torque is applied. Rule of thumb is that overtightening is not an answer toward leak–free and this may worsen the system via deformation of the thread, cutting the tube, or cracking the cell body materials. Another approach that should be considered is clean surface of O-rings. In the batch-type electrolyzer in the lab, Viton O-rings are used. This polymer–based O-rings are chemically inert and helps air-tight via concentrated force along with the perimeter. However, if the surface of the O-rings are not properly prepared (i.e., surface crack and dust on the surface) it can be a source of the leak. To prepare clean surface, Ultra-sonication in D.I. water for at least 20 min and rinsing with IPA solution is required prior to use. In case surface is cracked, it should be replaced to fresh one.

Preparation of membrane. The membrane should be cut to fit the area between anolyte and catholyte chamber. The total area of membrane needs to be adjusted to cover the O-ring but not reach to screws. Before assembling the cell, the membrane should be thoroughly rinsed with D.I. water. After rinsing, it is necessary to do ultra-sonication in D.I water for 20 min, followed by D.I water rinsing. Then, the cleaned membrane should be stored in D.I. water unless it is used for the next CO_2 immediately.

1.3.2 The GDE-incorporated Electrolyzer

Introduction to the Cell Compartments. The customized membrane electrode assembly (MEA) type electrolyzer (Fuel Cell Technology, Inc.) is designed to enhance overall activities of CO_2 conversion system via facilitating a rapid mass transport of CO_2 to the catalyst sites. To take advantage of facile mass transport from GDE and to optimize electrolzyer design for liquid products (formate in this thesis), a catholyte-free electrolzyer is developed via benchmarking the membrane-electrode-assembly type electrolyzer. The catholyte-free electrolzyer is sandwiching GDE with flow field and membrane. In this thesis, cation exchange membrane (Nafion 117, Fuelcellstore) is applied to feed protons from the anode chamber to the cathode chamber diffusing through the membrane. Due to the direct contact of catalyst layer to the membrane, the ohmic resistance of the electolyzer is maintained around 3 ohm. The nafion membrane is pre-cut ($1.5\times1.5cm^2$) and stored in the anolyte at least 12 hours prior to electrolysis after DI water sonication for 20 min. The interdigitated flow pattern is used to achieve well-distributed CO_2 feed and anolyte circulation. A sodium phospate buffer solution (0.5 M, pH 3) is used as an anolyte and it is circulated via analogue peristaltic pump. Considering the standard reduction potential (Pourbaix diagram), graphite and Ti are used as materials for cathodic and anodic flow field. The produced gas products and liquid product at the interface between the membrane and the catalyst layer are diffused out from the GDE, as shown in Figure 1.8. Air-tightness is achieved via PTFE gaskets and O-rings. The gaskets has a window to accomodate $1\times1cm^2$ area of GDE. IrO_2 coated Ti mesh is used as an anode. Gold-plated thin metal plates are used as a current collector and all of the components are clamped via end plates as shown in Figure 1.9.

1.3.3 Quantification of CO_2 Reduction Products

Separate efforts have been made to quantify gas and liquid products generated in the electrolyzer. In the current CO_2 electrolysis system, the expected gas products are CO, C_1–C_2 hydrocarbons (CH_4, C_2H_4, and C_2H_6) and parasitic H_2. In case of liquid products, formate, EtOH, n-ProH, and acetate are the major products that have been reported and detected during my research.

The gas products are formed on the catalyst surface and they are simultaneously delivered to the sampling loop in the gas chromatograph (GC, SRI GC, 8610C) through outlet of the electrolyzer via unreacted CO_2 gas stream as a carrier gas. Once 1 ml of gas samples are collected from the inner loop of GC, Ar carrier gas (at 15 psi) transports the sample gases into columns equipped in the oven (temperature range from 50 to 90 °C). A molecular sieve 5A is used to separate H_2 and a haysep D column is used to separate CO, CH_4, C_2H_4, and C_2H_6. A thermal conductivity detector (TCD) for H_2 detection and a flame ionization detector (FID) for CO, CH_4, C_2H_4, and C_2H_6 detection are applied. CO is detected via methanizer that is equipped to the FID (separate H_2 gas pressure to the methanizer is set to be 20 psi). Within an hour of CO_2

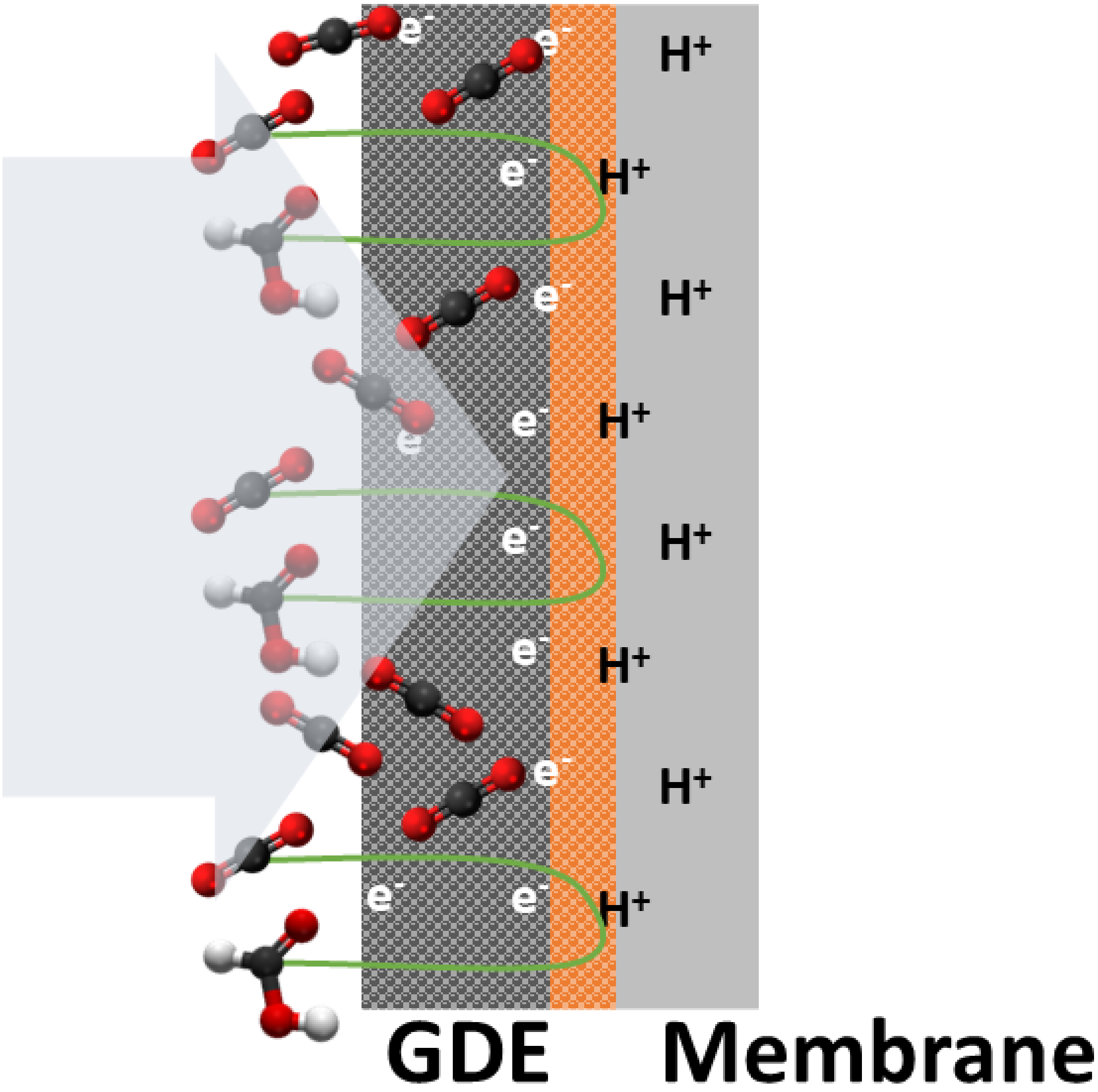

Figure 1.8. Scheme of a half cell electrolyzer with membrane-electrode-assembly configuration. The Conversion of CO_2 to formate is illustrated. The membrane represents a cation exchange membrane.

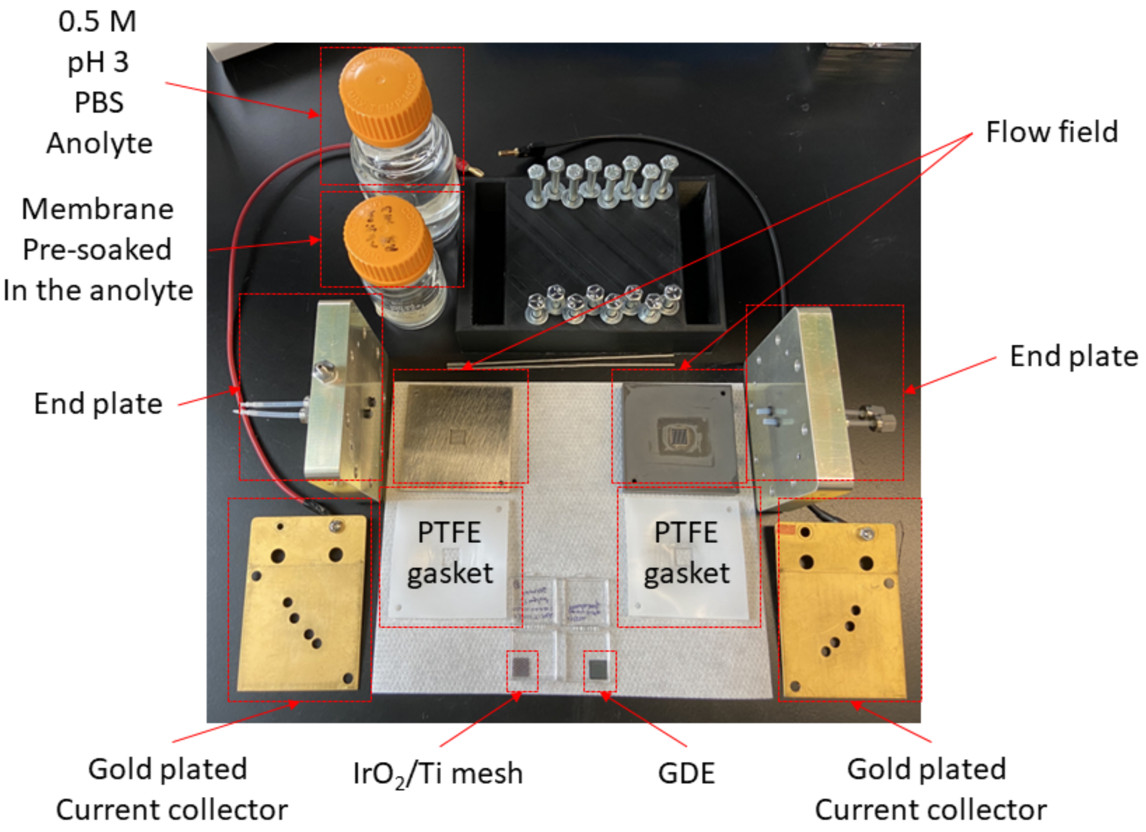

Figure 1.9. Components of the membrane-electrode-assembly type reactor in the lab.

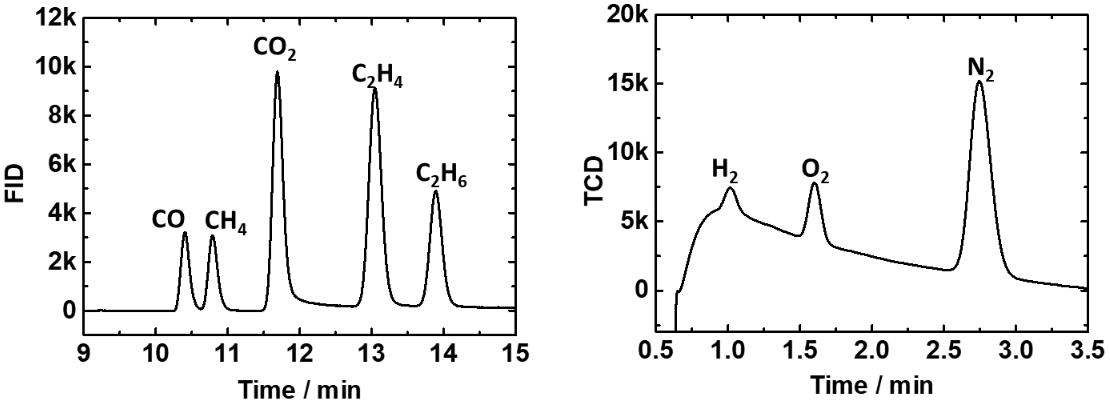

Figure 1.10. GC spectrums of gas compounds from FID and TCD channels using calibration gas.

electrolysis, 4 times of online quantification is designed to ensure repeatability and also monitor the activity of the catalysts as a function of the electrolysis time. Prior to the CO_2 electrolysis per day, GC is calibrated by using calibration gas mixtures. The standards contains 100 ppm of CO, CH_4, C_2H_6, and H_2, 200 ppm of C_2H_4, and 400, 2500, and 17000 ppm of CO_2, oxygen, and Nitrogen, balanced with Ar, respectively. The corresponding gas chromatography is shown in Figure 1.10. GC columns are baked at 250 °C on weekly basis to remove any residue compounds in the columns.

The liquid products are accumulated in the catholyte chamber (the batch-type reactor) and liquid products resolvior (the catholyte-free electrolzyer) during the electrolysis, and sampled at the end of electrolysis to ensure air-tightness of the electrolyzer. To quantify, two instruments of ^1H nuclear magnetic resonance (NMR) is utilized (AVA300, Bruker and ECA500, JEOL). The calibration curves are shown in Figure 2.5. Additional details are described in the Experimental procedures of the Chapter 2 and Kim et al..[5]

1.4 Acknowledgement

Chapter 1, in part, is a reprint of the material ”Enhancing C_2–C_3 Production from CO_2 on Copper Electrocatalysts via a Potential-Dependent Mesostructure” as it appears in ACS Applied Energy Materials, Taewoo Kim, Alireza Kargar, Yanqi Luo, Ragad Mohammed, Erick Martinez-Loran, Aditi Ganapathi, Priyasha Shah, and David P. Fenning, 2018, 1 (5), 1965. The dissertation author was the primary investigator and author of this material.

Chapter 2

Role of Strain: the Importance of Controlling Reaction Intermediate

2.1 Tuning CO_2 Reduction Pathway via Introducing Tensile Strain on Model Cu (001) Surfaces

Carbon dioxide electrolysis powered by renewable energy is a potentially attractive approach to close the carbon cycle and produce key chemical feedstocks. Here, we demonstrate the substantial influence of tensile strain on the selectivity of CO_2 reduction toward higher value-added, multi-carbon products by modulating the residual mismatch strain of Cu (001) thin film catalysts grown epitaxially on single crystal Si substrates. By decreasing film thickness from 100 nm to 20 nm, up to 0.22% tensile strain is introduced in-plane, shifting the measured Cu d-band center at the surface upward, in good agreement with theory. CO_2 electrolysis at moderate overpotential (-0.9 V vs RHE) in 0.1 M $KHCO_3$ electrolyte reveals that the shift in d-band center results in the suppression of single-carbon products, while activity for multi-carbon products is maintained. Examination of the ratio of partial current densities for multi-carbon products relative to CO and CH_4 suggests increased CO insertion and hydrogenation on the tensile-strained Cu (001) surface, driven by a change in the adsorbate bonding because of an increased interaction with the upshifted d-band. This work provides direct experimental evidence on model thin film CO_2 catalysts that strain can be systematically manipulated as a valuable tool – independent of catalyst composition – for the design of efficient CO_2 electrocatalysts toward energy dense products.

2.2 Introduction

The electrochemical reduction of CO_2 to carbonaceous fuels and chemical feedstocks is a potential strategy to mitigate global warming, leveraging readily accessible renewable energy.[4, 3, 5] CO_2 electrolysis in aqueous media can produce a variety of carbonaceous chemicals from single-carbon (C_1) products (CO, formate, and CH_4) to multi-carbon (C_2^+) products (C_2H_4, acetate, EtOH, and n-PrOH). In general, these products have high volumetric energy density and potentially facile integration with current industrial infrastructure. If produced using renewable sources of electricity, they have the potential to provide carbon-bearing feedstock chemicals with net negative carbon emission.[6, 7, 8]

Among transition metals, Cu is capable of producing value-added products such as C_2H_4 and oxygenates, while its poor selectivity is a key challenge.[4, 13, 14] Among many intermediates during electrochemical CO_2 reduction, it is widely suggested that *CO is a selectivity-determining intermediate for formation of C_2^+ products.[28, 29, 30, 31, 32, 33, 34] Defect-rich Cu surfaces with strong *CO binding sites have been reported to show enhanced CO_2 reduction selectivity to C_2^+ products.[16, 17] Strong *CO adsorption is accompanied with an increase in its surface population, which promotes CO-CO dimerization to form *OCCO intermediate.[18] Extensive efforts have been made to understand the reaction pathway to improve selectivity toward various target products. For example, abundant low-coordinated sites on small Cu nanoparticles increase chemisorption of CO_{ad} and H_{ad}, leading to increased syngas formation.[35] Metal substitution can induce weakened *H binding energy, leading to increased selectivity for liquid carbonyl products.[36] However, pathways to C_2^+ products are still in need of clarifying experiments to validate theoretical predictions regarding the reaction intermediates. Furthermore, testing of model catalyst surfaces, excluding structural and compositional complexities, can help isolate the effect of binding energy of key intermediate that tunes overall catalytic activity.

Remnant strain that arises from catalyst growth on a lattice-mismatched substrate has been proposed as one way to alter product distribution by modulating the adsorption strength of the selectivity-determining intermediates on the catalyst surface.[37, 19, 20] The effect of strain on the catalytic reactivity of a metal surface can be attributed to the change in the electronic structure. *d*-band theory[38, 39, 40] suggests that tensile strain on late transition metals shifts the *d*-band center up closer to the Fermi level and narrows the bandwidth. This shift decreases electron occupation in the anti-bonding states of the metal-adsorbate interaction and therefore results in stronger adsorbate binding on the metal surface. Prior study of CO_2 reduction on an electrodeposited polycrystalline Cu thin layer on a polycrystalline Pt substrate shows inhibited CH_4 production and favorable C-C bond formation, suggesting the possible contribution of strain on the product distribution.[19] A computational study of nanoparticle Pd icosahedra reveals that tensile strain at their surface induces a decreased Gibbs free energy of *COOH formation, which is a precursor of the *CO intermediate.[20] One of the practical challenges to understanding the effect of strain on the adsorption energy of CO_2 reduction intermediates is the experimental difficulty in excluding structural contributions such as surface defects,[16] surface roughness,[17] and nanoparticulate geometry.[41] Well-defined planar surfaces such as single crystal Cu[42] and epitaxially grown Cu[43, 44] can be used as model catalysts to evaluate the effect of strain on CO_2 reduction activity. First-principles calculations suggest that terrace of Cu (100) surface has a relatively lower reaction barrier for CO-CO coupling reaction as compared to closed-pack Cu (111) surface that facilitates activity of C_2^+ products formation.[18, 45] As tensile strain is applied on Cu (100) surface, the *CO adsorption energy is predicted to increase, increasing its coverage on the surface, which may improve CO dimerization or chemical coupling reactions with nearby C_1 intermediates.[18] One can also expect an increase in *H adsorption with tensile strain due to the scaling relations that indicate its adsorption energy scales with *CO across surfaces.[46] Increased *H can foster hydrogenation of reaction intermediates, which is proposed to be an essential step for formation of C_2^+ products.[18]

Herein, we demonstrate the role of strain on catalytic activity in the electrochemical CO_2 reduction on Cu (001) surface by adopting a series of epitaxially-grown Cu films. The magnitude of strain is controlled by varying Cu film thickness, which modulates the relaxation of tensile strain originating from lattice mismatch between the Cu film and Si substrate.[19, 47, 48] As film thickness decreases, increased tensile strain leads to an upshift in d-band center. This change in electronic structure at the surface leads to reduced activity toward single-carbon products while activity for C_2^+ products is maintained, resulting in greatly improved selectivity. The results suggest that tensile strain on the epitaxially grown Cu (001) surface increases adsorption energy of both *CO and *H, hindering the generation of single-carbon products but sustaining dimerization and hydrogenation to C_2^+ products in the face of abundant hydrogen evolution. This work demonstrates that the overall activity and selectivity of electrochemical CO_2 reduction on Cu (001) surfaces can be modulated by tuning the magnitude of tensile strain, resulting from changes in the d-band center that enhance the adsorption energy and population of key reaction intermediates on the surface.

2.3 Experimental Procedures

Preparation of Epitaxial Cu (001) on Single Crystal Si (001) Substrate. Single-side polished Si (001) wafers (University Wafers, p-type, 1-100 ohm cm) are used as a substrate to achieve epitaxial growth of Cu (001) films. The wafers are diced into $2.15 \times 4.5 cm^2$ sized pieces that are sonicated in a mixture of Acetone:IPA:DI water (6:3:1 v/v), followed by DI water for 10 min each, and subsequently dried with a N_2 gun. To remove the native oxide layer and trace amount of metal impurities, the substrates are immersed in 20 vol% of HF for 5 min and then transferred to 20 vol% of HCl solution for 5 min. Prior to Cu deposition, the cleaned substrates are submerged into 20 vol% of HF solution again to establish an H-terminated surface. Immediately after HF treatment, the Si substrates are transferred into an ultra-high vacuum ($\sim 4 \times 10^{-9}$ Torr) chamber for sputter deposition of Cu in an AJA ATC Orion DC

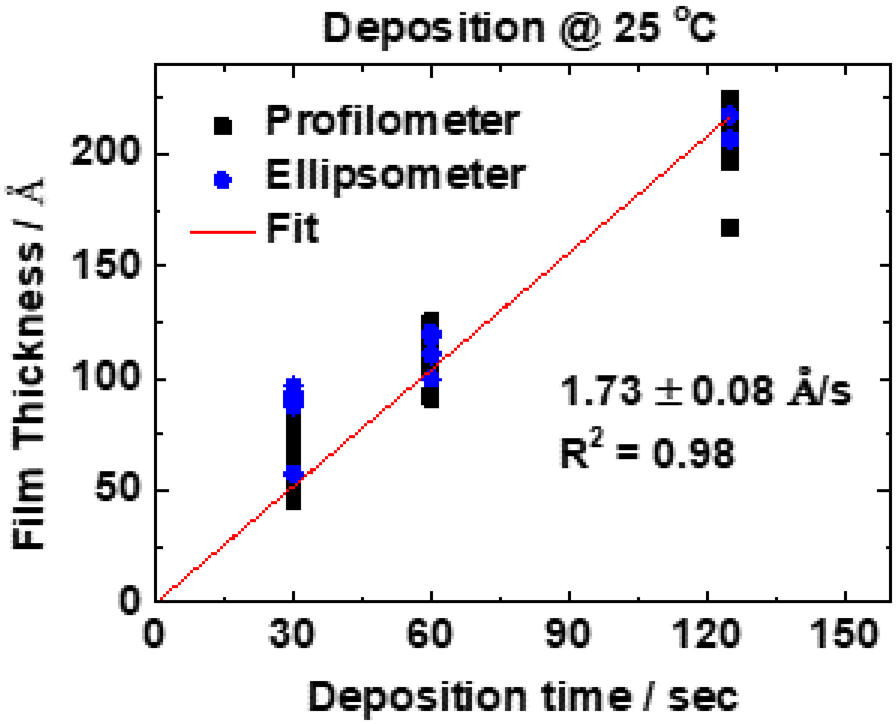

Figure 2.1. Film thickness and sputtering rate determination by profiler and ellipsometer

magnetron sputtering system. The pressure and flow rate of Ar are set to be 3 mTorr and 10 sccm, respectively. Cu (99.999%, AJA) is sputtered at a rate of 1.73(8) Å s^{-1} at room temperature to fabricate 20, 30, 40, and 100 nm of Cu films. The thickness of the films and sputtering rate are carefully determined by a Dektak 150 surface profiler and J.A. Woollam M-2000D spectroscopic ellipsometer (Figure 2.1). For the film annealed post-growth, we grow 100 nm epitaxial Cu (001) film on a Si substrate at room temperature and subsequently anneal it at 65 ^{o}C for 14 hrs in the high vacuum chamber (1.7×10^{-8} Torr). The as-prepared film catalysts are individually stored in a vacuum bag when not in use to inhibit partial oxidation of the film in ambient air.

Physical Characterization of Films Out-of-plane and in-plane crystalline texture of the epitaxial Cu (001) film is examined by X-ray diffractometry (XRD, Rigaku, Smartlab) using Cu-Kα radiation. The medium resolution parallel beam optics are used for the analysis. The tensile strain is calculated from the bulk lattice constant of Cu and the estimated lattice constant at the surface of the films measured via in-plane grazing-incidence X-ray diffraction (GI-XRD).

The X-ray angle of incidence is selected to be the critical angle (0.4°) where the X-ray interaction produces only an evanescent wave at the surface, producing diffraction patterns specific to the surface. The Bragg angle of the Cu (200) peak decreases with decreasing film thickness (the inset of Figure 2.7A), indicating that the epitaxial mismatch results in in-plane tension at the surface of the Cu thin films. Out-of-plane X-ray diffraction confirms a Cu (001) surface on the Si substrate with a native Cu oxide layer present (Figure 2.2). The oxide layer is formed upon air exposure during transportation of the films from the vacuum growth chamber. The surface morphologies are characterized by scanning electron microscopy (SEM, Zeiss, Sigma 500) and atomic force microscopy (AFM, Veeco, Dimension 3100), operating in "tapping mode". Surface valence band and core-level electronic structure of the as-prepared films are determined by Ultra-violet photoelectron spectroscopy (UPS) and angle-resolved X-ray photoelectron spectroscopy (XPS) with 90° emission angle with respect to film surface (Kratos, AXIS Supra) with He-1 and Al-Kα radiation, respectively. The UPS and XPS spectra are recorded using pass energies of 160 eV for the XPS survey and 20 eV for the UPS and XPS narrow scans. The binding energies are calibrated using both Fermi edge (-0.06 eV) and the Au 4f 7/2 second-order peak (84 eV).

Caron Dioxide Electrolysis The electrochemical reduction of carbon dioxide is carried out in a customized electrochemical cell[5] using a three-electrode setup at room temperature and ambient pressure. The working and counter electrode compartments are separated by an anion exchange membrane (Selemion AMV, AGC inc.). Pt gauze (100 mesh, 99.9% metal basis, Sigma-Aldrich) and Ag/AgCl (in KCl gel, Pine Research) are used as a counter and reference electrode, respectively. CO_2-saturated aqueous 0.1 M $KHCO_3$ solution ($\geq$ 99.95% metal basis, Sigma-Aldrich) is applied as an electrolyte (pH = 6.8). Additional purification of electrolyte is carried out to remove metallic impurities by using chelating agent (Chelex 100, Bio-Rad Laboratories, Inc.) prior to CO_2 electrolysis.[49] Research grade CO_2 is continuously purged into the electrolyte at flow rate of 5 sccm during CO_2 electrolysis, controlled via mass flow controller (Smart Track 100, Sierra). The electrochemical analysis of the electrodes is conducted using a potentiostat (VSP-300, biologic). The potentials reported herein are corrected by 85%

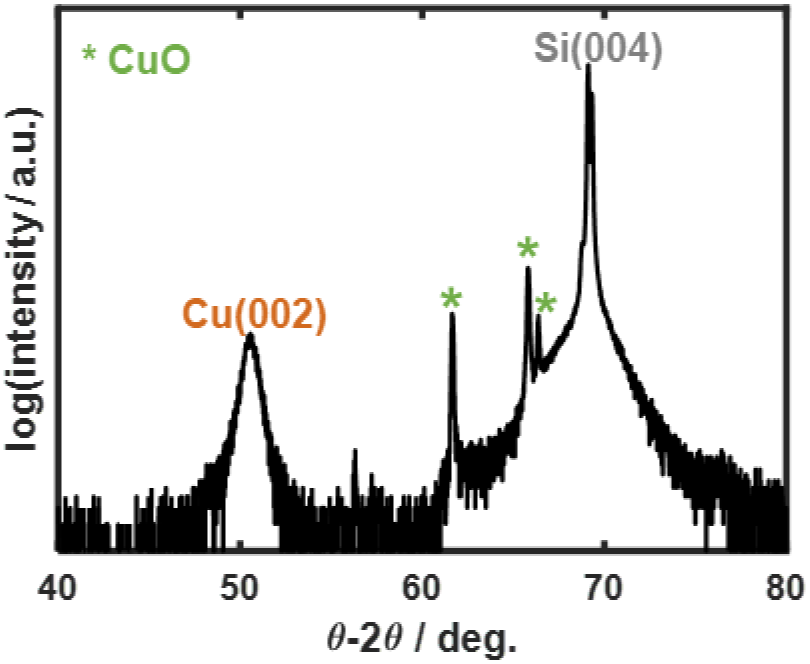

Figure 2.2. Theta-2theta scan of a representative epitaxial Cu (001) film on single crystal Si (001) substrate. Bragg diffraction angles are confirmed by using Cu (ICSD PDF No. 43-493), CuO (ICSD PDF No. 16-025), and Si (ICSD PDF No. 51-688) references.

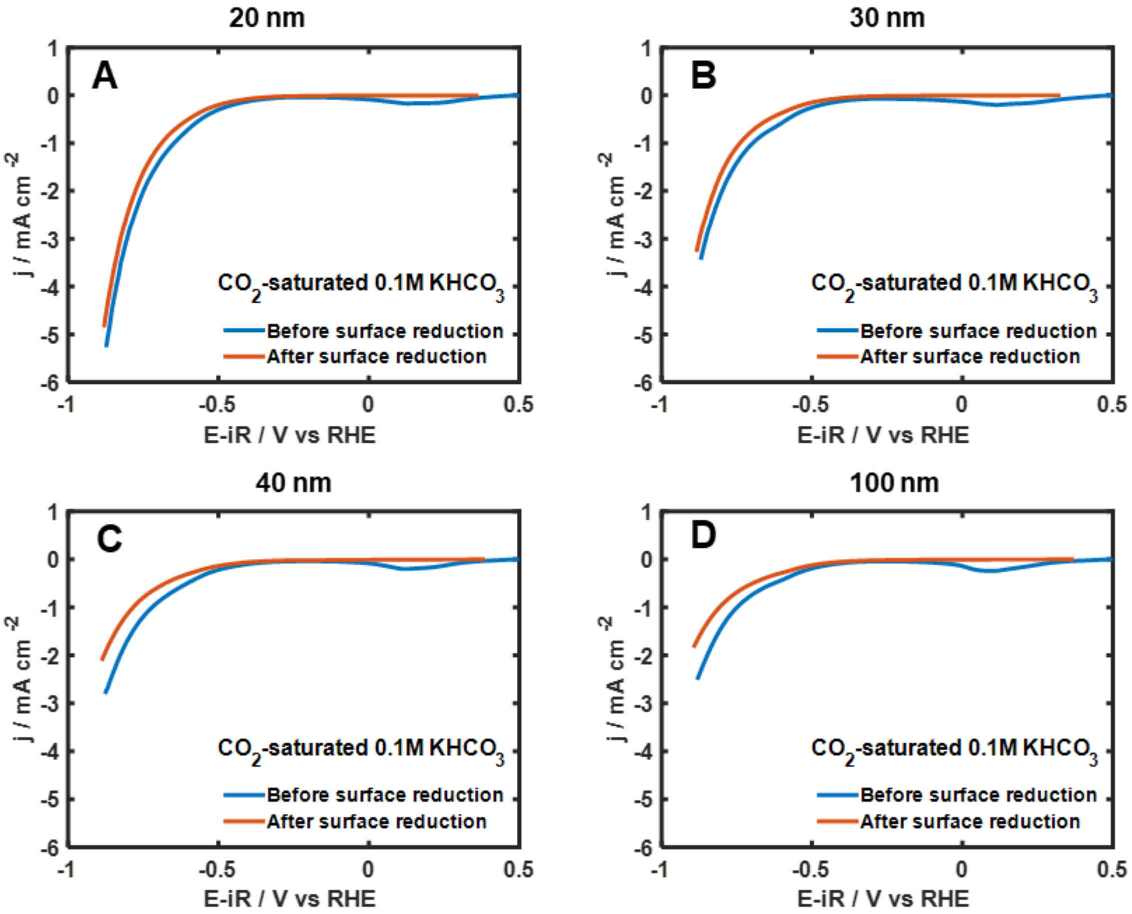

Figure 2.3. Linear sweep voltammogram on epitaxial Cu (001) films with varied thickness at 20 mV s^{-1} of scan rate. (A) 20 nm, (B) 30 nm, (C) 40 nm, and (D) 100 nm. Removal of native oxide layer is confirmed by disappearance of reduction peak at ≥ 0 V vs RHE after 10 min of pre-electrolysis at the corresponding potentials.

automatic iR-compensation and 15% manual compensation and converted to the reversible hydrogen electrode (RHE) scale.[4, 5] Prior to CO_2 electrolysis, the as-prepared epitaxial Cu (001) film surfaces undergo pre-electrolysis for 10 min at the corresponding potentials to remove the native oxide layer, and the corresponding data is shown in Figure 2.3.

Quantification of gas and liquid products At least three electrolyses are performed at each film thickness for repeatability. All gas products produced in the working electrode compartment are collected directly into a gas-sampling loop and quantified by online gas chromatography (GC, SRI 8610C, Sri) (Figure 2.4) with a molecular sieve 5A and a Haysep D

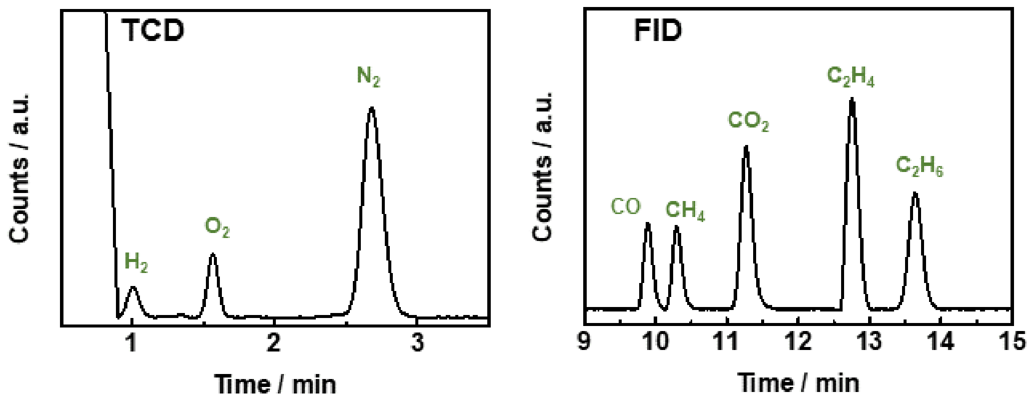

Figure 2.4. GC spectrums of gas compounds from FID and TCD channels using calibration gas.

column, a TCD/FID detector, and using Ar as a carrier gas. The partial current density of each gas product is averaged over 4 GC injections during 1 hr chronoamperometry (CA) measurements. The liquid products from both working and counter electrode compartments (total volume of the cell: 16 ml) are quantified at the end of the electrolysis using ^{1}H nuclear magnetic resonance (NMR) spectroscopy with a 300 MHz spectrometer (AVA300, Bruker), as shown in Figure 2.5. Additional details can be found in our previous work.[5] Geometric partial current density of CO_2 reduction products is calculated from steady state current density during chronoamperometry and quantification of the reaction products by GC-TCD/FID and ^{1}H NMR. The partial current densities, Faradaic efficiencies and the standard-deviations between electrolysis are shown in Table 2.1 and S2, respectively.

Table 2.1. Geometric partial current density of the electrochemical CO_2 reduction products over the epitaxial Cu (001) film catalysts on Si (001) substrates.

Thickness / nm	**Ip strain / %**	***d*-band center / eV**	**j_total / mA c m^{-2}**	**H_2**	**CO**	**CH_4**	**C_2H_4**	**Formate**	**Acetate**	**EtOH**	**n-PrOH**
20	0.22 (0.03)	2.49	4.42 (0.46)	3.36 (0.38)	0.03 (0.01)	0.01 (-)	0.27 (0.06)	0.04 (-)	0.05 (0.01)	0.14 (0.02)	0.12 (0.01)
30	0.10 (0.11)	2.51	2.04 (0.47)	1.52 (0.24)	0.04 (0.01)	0.02 (-)	0.30 (0.05)	0.06 (0.02)	0.04 (-)	0.11 (0.01)	0.08 (0.02)
40	0.03 (0.03)	2.53	1.62 (0.15)	0.77 (0.15)	0.04 (0.01)	0.02 (-)	0.34 (0.03)	0.10 (0.01)	0.06 (0.01)	0.14 (0.02)	0.09 (0.03)
100	0.01 (0.03)	2.57	1.38 (0.09)	0.58 (0.11)	0.04 (0.01)	0.04 (0.01)	0.30 (0.06)	0.10 (-)	0.05 (0.02)	0.13 (0.01)	0.10 (0.04)

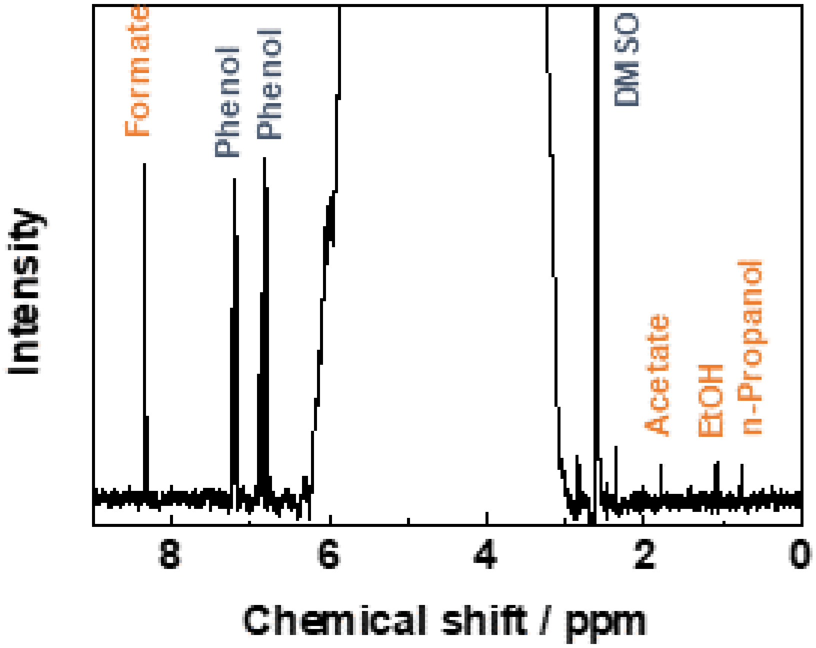

Figure 2.5. ^{1}H NMR spectrum of electrolyte after 1 hr of electrolysis on epitaxial Cu (001) film (100 nm of thickness) on Si (001) substrate at -0.9 V vs RHE in CO_2-saturated 0.1M $KHCO_3$ electrolyte.

2.4 Changes in the Electronic Structure via In-plane Tensile Strain

Strained epitaxial Cu (001) thin films of thickness 20 to 100 nm are grown on single crystal Si (001) substrates, leveraging the epitaxial relationship between the rotated lattices.[43, 50, 51, 52] The epitaxial relationship of Cu thin films and Si substrate is confirmed by phi scans as shown in Figure 2.6A, indicating the expected 45° in-plane rotation of Cu lattice with respect to Si substrate.[52]

Surface-sensitive grazing-incidence X-ray diffraction conducted at the critical angle reveals 0.22% in-plane tensile strain in the 20 nm film, which decreases to 0% at the surface of the 100 nm film, as shown in Figure 2.7A. These data indicate that changing film thickness can modulate the remnant tensile strain at the surface.

The tensile strain is a function of film thickness, since the critical thickness where misfit dislocation appear is in principle only several nanometers from the Cu (001)/Si (001) interface.[53] This is consistent with the results (Figure 2.7A) in which decreasing tensile strain is observed with increasing film thickness, indicating strain relaxation.[19, 47, 48] Figure 2.6B shows the in-plane texture of the as-prepared films measured with an incidence angle of 0.5°, above the critical angle for external reflection. The corresponding in-plane tensile strain samples the bulk of the film (Figure 2.6C) and is larger in magnitude than the surface-specific measurement (Figure 2.7A), confirming the strain gradient from the growth interface to the surface.

Comparison of the valence band (VB) spectra from ultraviolet photoelectron spectroscopy (UPS) as a function of film thickness reveals systematic alteration of the surface electronic structure. The spectra of Figure 2.7B shows a narrowing bandwidth as a function of tensile strain. This is suggestive of a reduced overlap of the wavefunctions because of the expanded distance between Cu atoms at the surface under tensile strain.[40] We note that the native oxide layer and trace surface contaminants are removed by Ar-ion sputtering (for 90 sec at 5 keV) prior to VB

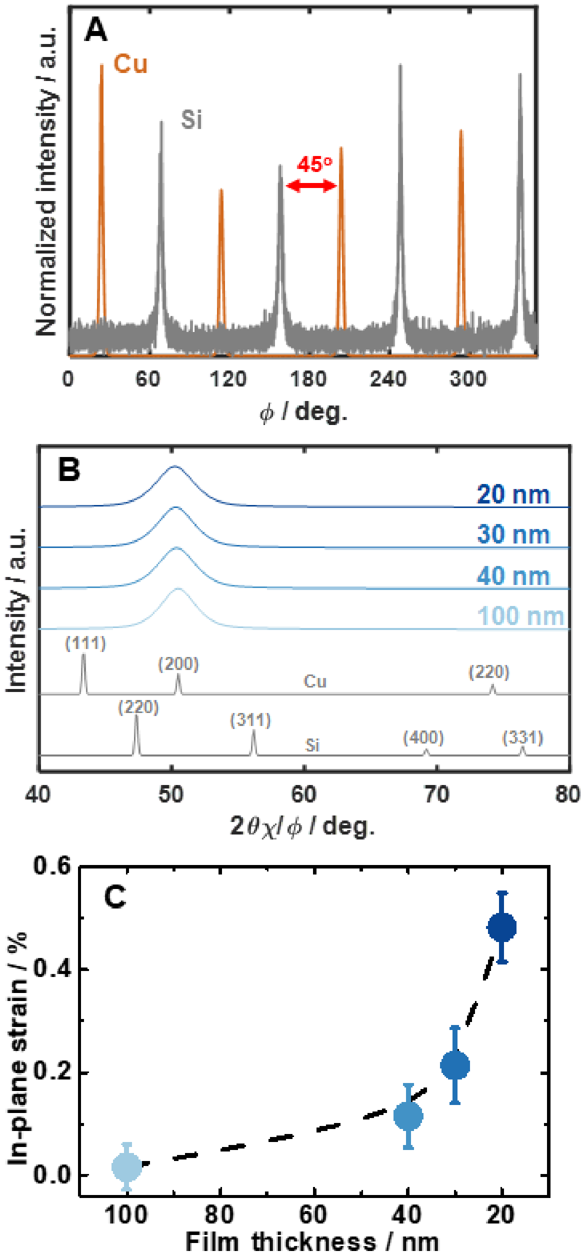

Figure 2.6. X-ray diffractometry on as-prepared epitaxial Cu (001) on single crystal Si substrate. (A) phi scan of a representative epitaxial Cu (001) film on single crystal Si (001) substrate. (B) In-plane X-ray diffraction patterns of each film at 0.5° angle of incidence. (C) Corresponding in-plane strain as a function of film thickness. Bragg diffraction angles are confirmed by using Cu (ICSD PDF No. 43-493) and Si (ICSD PDF No. 51-688) references.

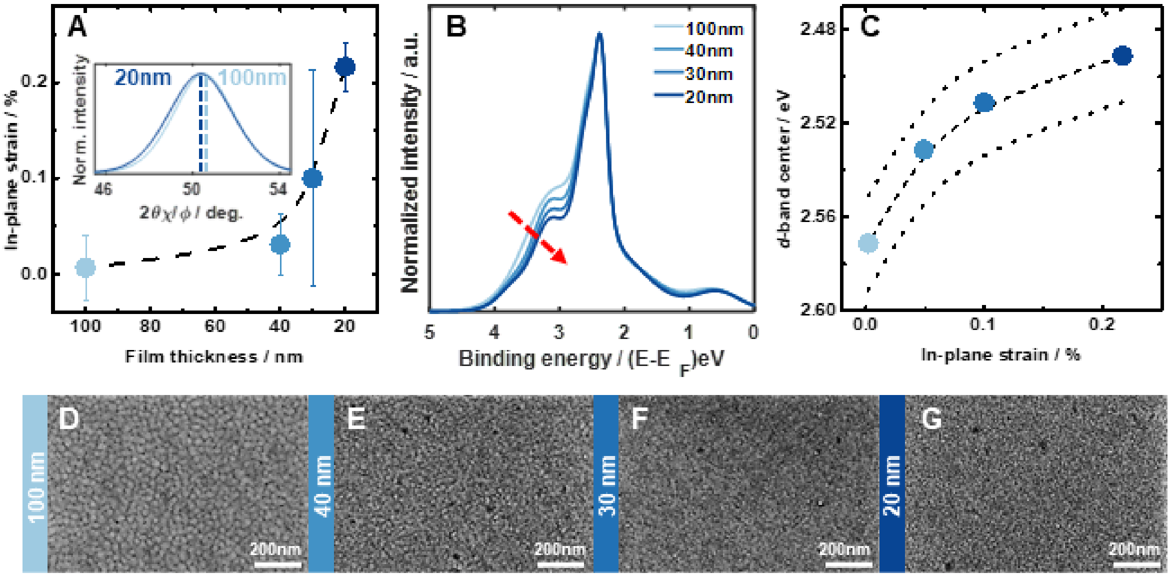

Figure 2.7. Structural properties of as-prepared epitaxial Cu (001) on single crystal Si (001). (A) In-plane strain at the surface measured as a function of film thickness by grazing-incidence X-ray diffraction. The inset shows the shift of the Bragg peak to lower angle with decreasing film thickness. (B) He-I UPS valence band spectra. (C) d-band center from UPS as a function of in-plane strain. The 99% confidence interval is shown with dotted lines. SEM images of Cu (001) films: (D) 100 nm, (E) 40nm, (F) 30nm, and (G) 20 nm.

measurement. Post-cleaning, Cu 2p XPS spectra indicate a surface of purely metallic Cu, as seen in Figure 2.8A-B, analogous to the surface on which the catalytic reaction occurs. We extract the *d*-band center by fitting the VB spectra[54] (Fig. 2.8C), and the resulting *d*-band center is shown as a function of strain at the surface of the catalyst films in Figure 2.7C. The data indicate that the *d*-band center shifts upward toward the Fermi level by about 80 meV as tensile strain at the surface reaches 0.22 %, a trend in agreement with the prediction by *d*-band theory.[38, 39, 40]

The film catalysts exhibit a columnar microstructure, as seen in the scanning electron micrographs of Figure 2.7D-G and Figure 2.9. The average column size decreases with decreasing film thickness, and in all films gaps between the columns exist, with more gaps in thinner films. This microstructures agrees well with the Structure-Zone Model (SZM) for physical vapor deposition at room temperature.[55, 56] While the XRD indicates the crystallites are perfectly textured, the gaps between crystallites may expose step and kink sites. Electric double-layer

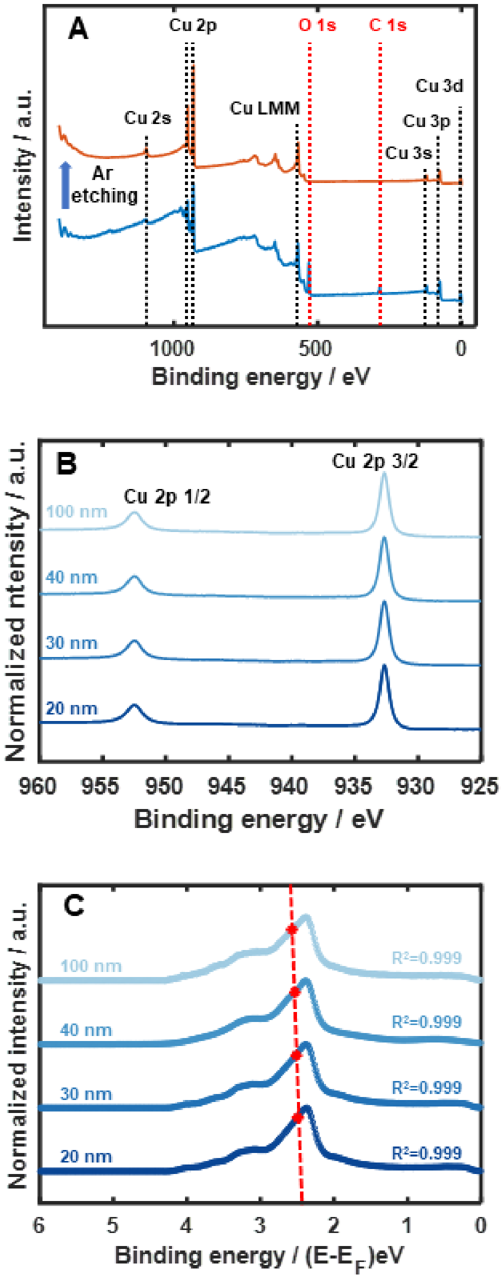

Figure 2.8. Electronic structure of the as-prepared epitaxial Cu (001) films. (A) XPS survey spectra of a representative Cu (001) film on Si substrate before (blue) and after (orange) Ar$^+$ ion etching. All sample surfaces were etched similarly prior to UPS and XPS measurements. (B) Cu 2p XPS spectra of Cu (001) films with varying film thickness. (C) UPS valence band spectra collected using He–I excitation. The red $*$ indicates *d*-band center estimated to the weighted average energy of the valence band spectra.[54]

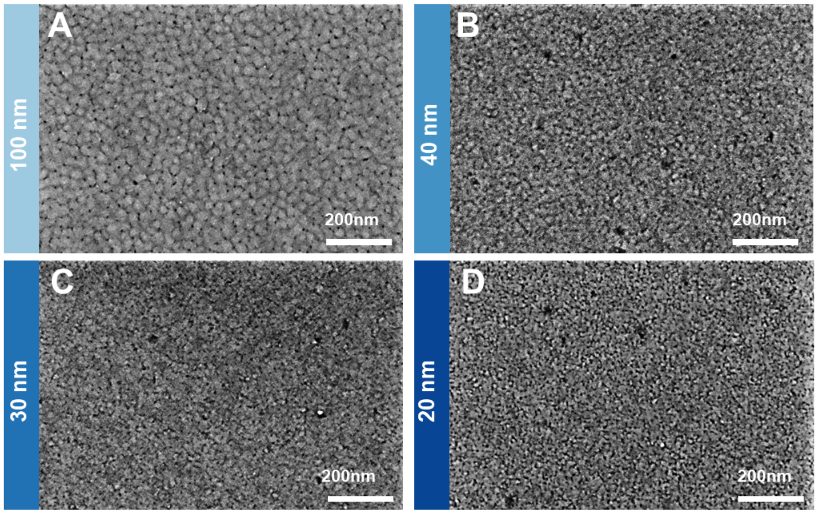

Figure 2.9. Full size SEM images of Cu (001) films: (A) 100nm, (B) 40nm, (C) 30nm, and (D) 20nm.

capacitance (EDLC) measurements of the films yield roughness factors between 1.1 to 1.6, as shown in Figure 2.10, confirming minimal nanoscale roughness.

The strained Cu (001) film catalysts exhibit stable current densities during 1 hr of CO_2 electrolysis at -0.9V vs RHE in 0.1M $KHCO_3$ (Figure 2.11). After the electrolysis, the film morphology remains largely unchanged, though pinholes form across $\leq 5\%$ of the area because of film delamination (SEM shown in Figure 2.12, post-electrolysis EDLC shown in Figure 2.10). The background current from any exposed Si (001) substrate is extremely small ($\sim$4 uA cm^{-2}), indicating that the effect of any possible substrate exposure through the pinhole on CO_2 reduction is negligible.

2.5 Effect of Tensile Strain on CO_2 electrolysis activities

Figure 2.13 shows the dependence of CO_2 reduction activity on the *d*-band center of the strained Cu (001) film catalysts. The corresponding data are detailed in Table 2.1. Grouping CO_2 reduction products according to the number of constituent carbon atoms makes clear in Figure 2.13A that an upshift in the *d*-band center suppresses formation of single-carbon products, while

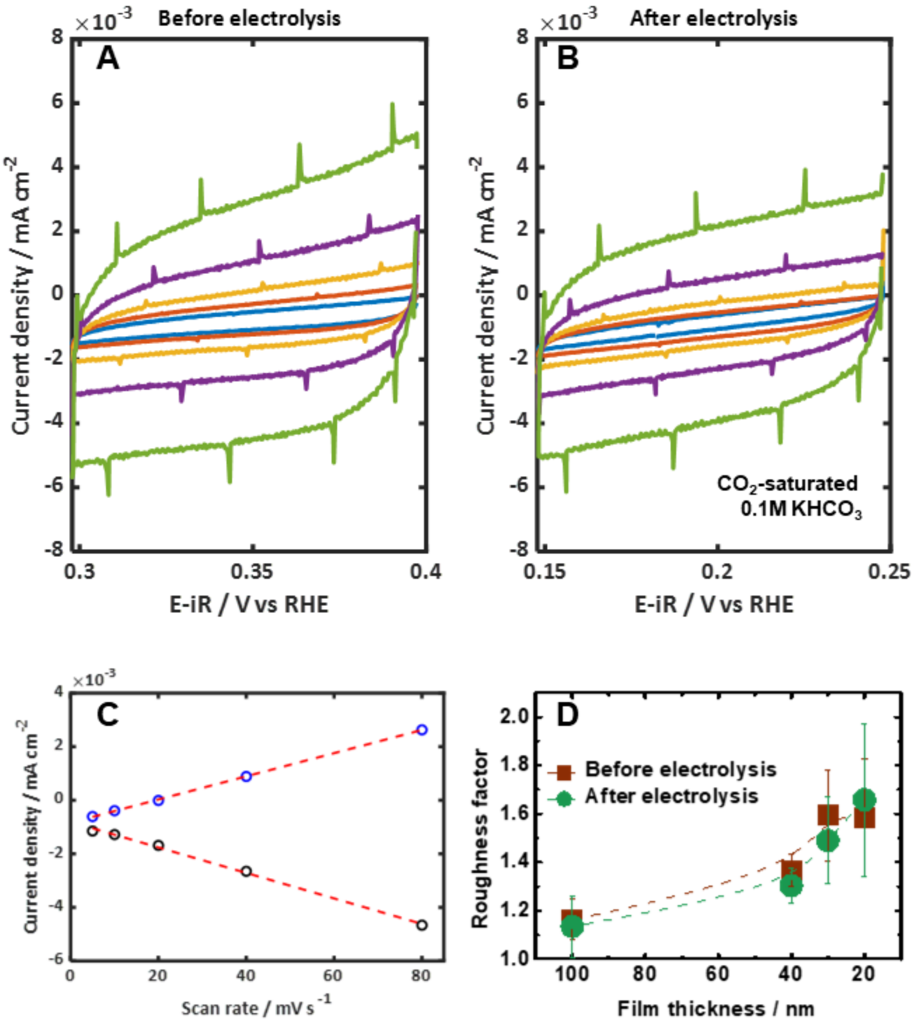

Figure 2.10. Double-layer capacitance of the as-prepared epitaxial films. (A-B) Typical cyclic voltammograms of the epitaxial Cu (001) film before and after 1hr of electrolysis. Scan rates are 5, 10, 20, 40, and 80 mV s^{-1}. (C) Plot of the current density vs scan rates. (D) Roughness factor of the films with respect to film thickness before and after electrolysis. Error bars indicate a standard deviation of measurements across at least three samples. Consistent purging of CO_2 for more than 30 min before and during the analysis ensures no remaining pre–dissolved gases such as oxygen in the electrolyte. The cyclic voltammetry is performed in the potential range where the major current is capacitive current.[42] The capacitance is estimated by $(j_a – j_c)/2$ at the centroid potential of given potential range (where j_a and j_c are the anodic and cathodic current densities, respectively) against the scan rate. The shift in the potential range between before vs. after electrolysis is due to the small alternations of the film surface during electrolysis. The spikes in the voltammogram are simple artifacts coming from the automatic current range setting of the potentiostat and do not affect the analysis. Roughness factor is calculated by using the capacitance of a polycrystalline Cu foil as a reference value of 1.[5]

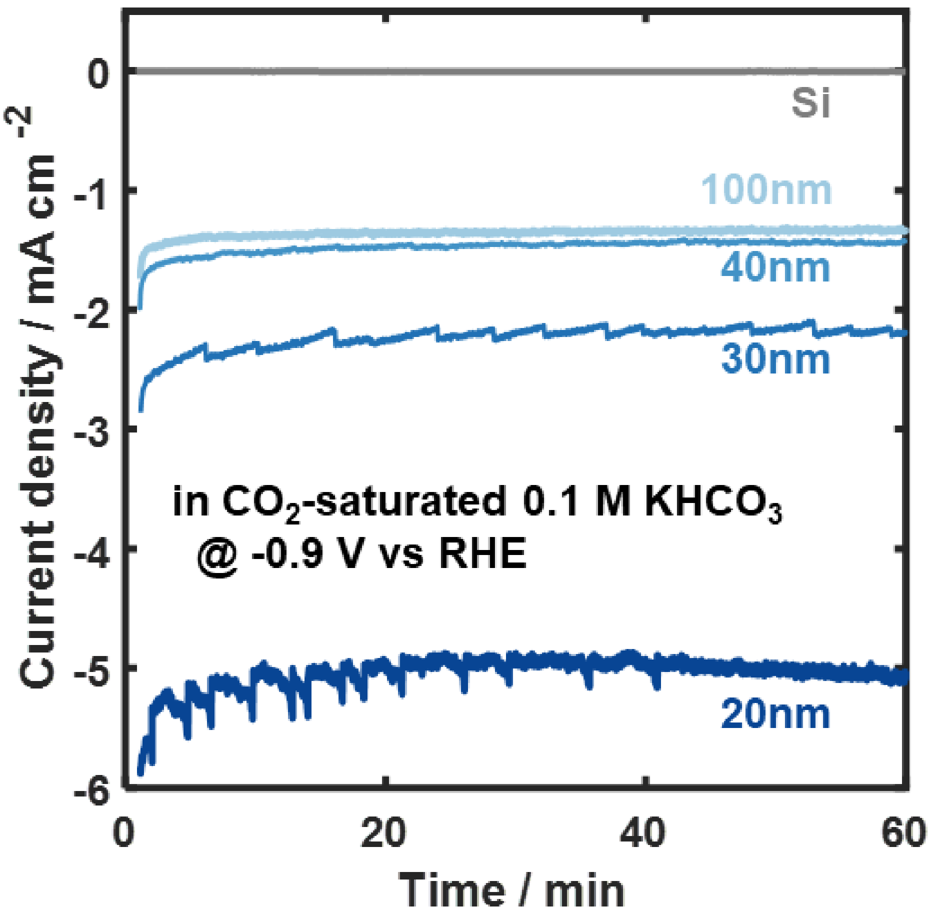

Figure 2.11. Current density profile with respect to electrolysis time.

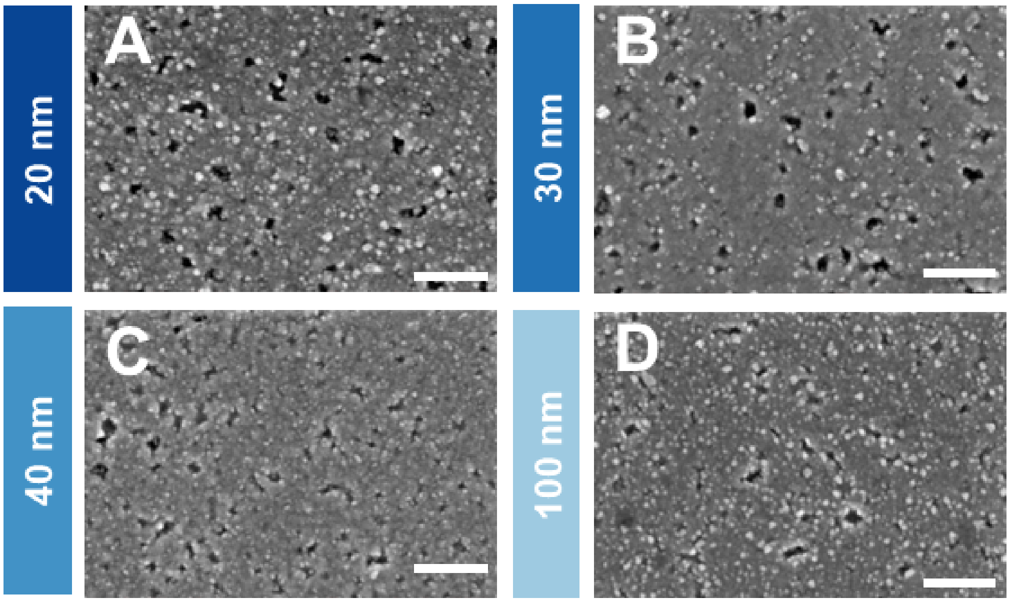

Figure 2.12. SEM images of epitaxial Cu (001) on Si (001) substrate after electrolysis at –0.9 V vs RHE for 1 hr. Scale bars are 200 nm.

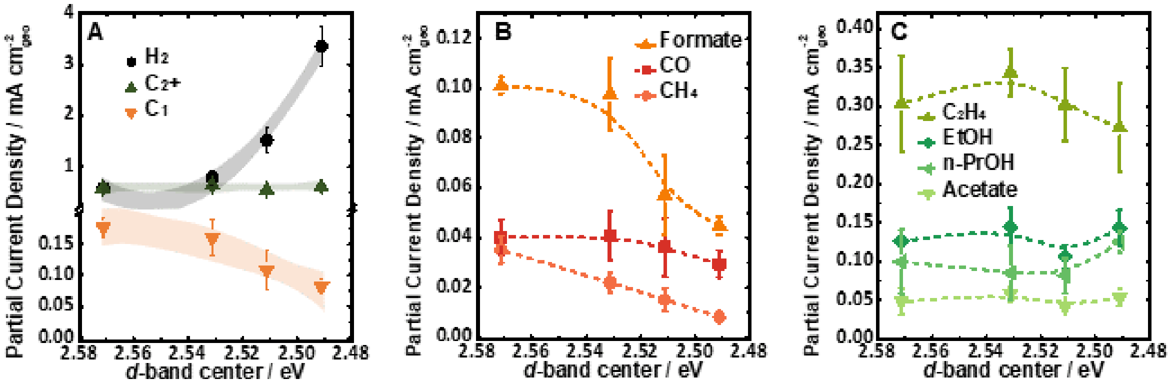

Figure 2.13. Geometric partial current densities of (A) hydrogen, multi-carbon (C_2+), and single-carbon (C_1) products, (B) single-carbon products, and (C) multi-carbon products formation at -0.9 V vs RHE in CO_2-saturated 0.1M $KHCO_3$ electrolyte. The shaded regions indicate a 95% confident interval using a quadratic model to describe the data.

multi-carbon products are sustained despite an increase in hydrogen evolution. We performed a statistical analysis to quantitatively examine whether shift in the *d*-band center is responsible for the changes in the partial current densities of hydrogen, C_2^+, and C_1 products. Ordinary least-squares (OLS) regression is used to fit a quadratic model (equation 2.1) between *d*-band center (d_{center}) and the geometric partial current density (j_{geo}) of hydrogen, C_1, and C_2^+ products. The regression results are subjected to an F–test[57], which quantifies the explanatory power of the regression in comparison to an intercept-only model (i.e. does the independent variable d_{center} influence the dependent variable j_{geo}?). The F–test generates a p–value for the overall regression.

$$j_{geo} = a + b \times d_{center} + c \times d_{center}^2 \tag{2.1}$$

As shown in Figure 2.13A, the confidence intervals for the increase in hydrogen evolution and decrease in C_1 products formation clearly include non-zero coefficients, where the C_2^+ bands include coefficients of zero. This is substantiated by the resulting p–values, where a trend of hydrogen evolution and the C_1 trend with the shift in the *d*-band center are significant at $p < 0.001$ and $p \leq 0.001$, respectively, while there is no meaningful trend for C_2^+ ($p = 0.983$). This confirms the dependence of CO_2 reduction selectivity and activity on the *d*-band center of Cu (001) surfaces.

Focusing more finely on the single-carbon products, Figure 2.13B shows that an 80 meV upshift in *d*-band center reduces the partial current densities for formate by 60% (from 0.10 to 0.04 mA cm^{-2}) and for CH_4 by 75% (from 0.04 to 0.01 mA cm^{-2}). The partial current density for CO also decreases from 0.04 to 0.03 mA cm^{-2}. Single-carbon product formation is clearly sensitive to the change in the electronic structure.

In contrast, the partial current densities for oxygenate products (EtOH, n-PrOH, and Acetate) are steady across *d*-band positions, as shown in Figure 2.13C (at $\sim$0.13, 0.10, and 0.05 mA cm^{-2}, respectively). The partial current density for C_2H_4 is roughly unchanged at $\sim$0.3

mA cm^{-2}, perhaps decreasing modestly ($<$10%) at the highest strains. The flat trend of the C_2^+ products with *d*-band center position suggests that strain on the (001) surface of the catalysts does not dominate the C-C coupling efficiency.

The Faradaic efficiencies of the Cu (001) catalysts as a function of *d*-band center are shown in Figure 2.14 and detailed in Table 2.2. As the *d*-band center shifts upward, the Faradaic efficiencies of all CO_2 electrolysis products decline because of parasitic hydrogen evolution reaction (HER). In the discussion below, we focus on insights into the reaction pathway for CO_2 reduction through analysis of the partial current densities of CO_2 reduction products as a function of strain on the Cu (001) surface. However, we emphasize that at high strains, HER increasingly outpaces CO_2 reduction on Cu (001) and dominates the Faradaic efficiency. Use of a gas diffusion electrode architecture[58, 59] could be a path to circumvent such high parasitic HER and leverage the tuning of CO_2 reduction intermediates by strain. In addition, one can expect that using an alkaline electrolyte would shift the overall overpotential for CO_2 reduction products more positive.[29] While the experiments reported here focused on CO_2 electro-reduction, no substantive shift in overpotential for multi-carbon product formation is expected upon changing the starting reactant from CO_2 to CO, based on previous results indicating CO_2-to-CO conversion is not the rate-limiting step on Cu surfaces.[29]

Table 2.2. Faradaic efficiencies of the electrochemical CO_2 reduction products over the epitaxial Cu (001) film catalysts on Si (001) substrates.

Thickness / nm	Ip strain / %	*d*-band center / eV	FE_total / %	H_2	CO	CH_4	C_2H_4	Formate	Acetate	EtOH	n-PrOH
20	0.22	2.49	91.55	75.91	0.67	0.19	6.24	1.05	1.27	3.44	2.93
	(0.03)		(2.18)	(2.02)	(0.11)	(0.07)	(1.45)	(0.11)	(0.31)	(0.86)	(0.27)
30	0.10	2.51	92.12	64.06	1.95	0.80	15.79	3.10	2.21	5.40	4.16
	(0.11)		(0.01)	(6.04)	(0.88)	(0.31)	(4.47)	(1.37)	(0.64)	(0.85)	(1.14)
40	0.03	2.53	94.44	47.57	2.56	1.39	21.39	5.86	3.58	8.83	5.02
	(0.03)		(2.64)	(5.53)	(0.72)	(0.36)	(1.75)	(0.19)	(0.86)	(2.01)	(1.81)
100	0.01	2.57	96.37	41.60	2.90	2.55	22.18	7.59	3.63	9.48	7.41
	(0.03)		(1.57)	(5.59)	(0.55)	(0.39)	(4.84)	(0.44)	(1.29)	(0.65)	(2.94)

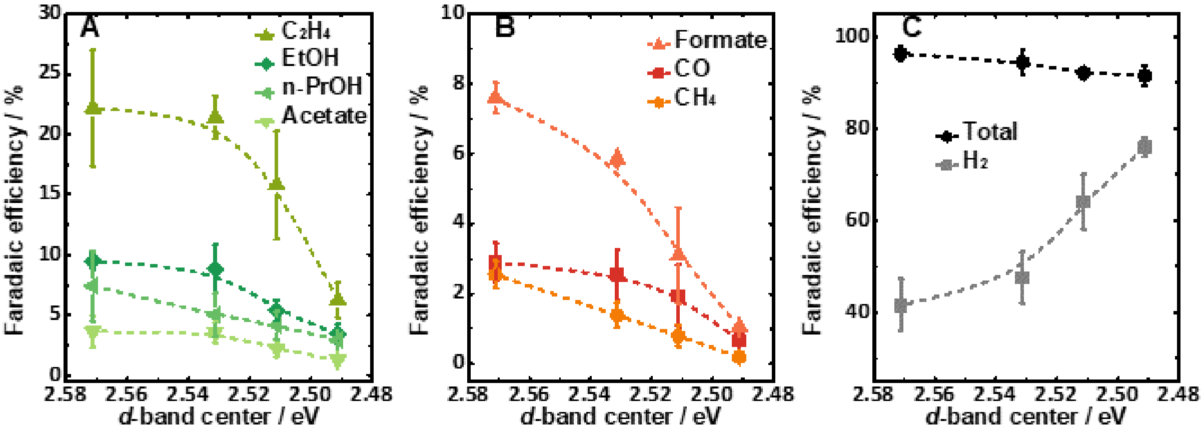

Figure 2.14. Faradaic efficiencies of CO_2 reduction products on epitaxial Cu (001) film catalysts as a function of *d*-band center. (A) multi-carbon, (B) single-carbon products, and (C) Hydrogen and total Faradaic efficiency at -0.9 V vs RHE in CO_2-saturated 0.1 M $KHCO_3$ electrolyte.

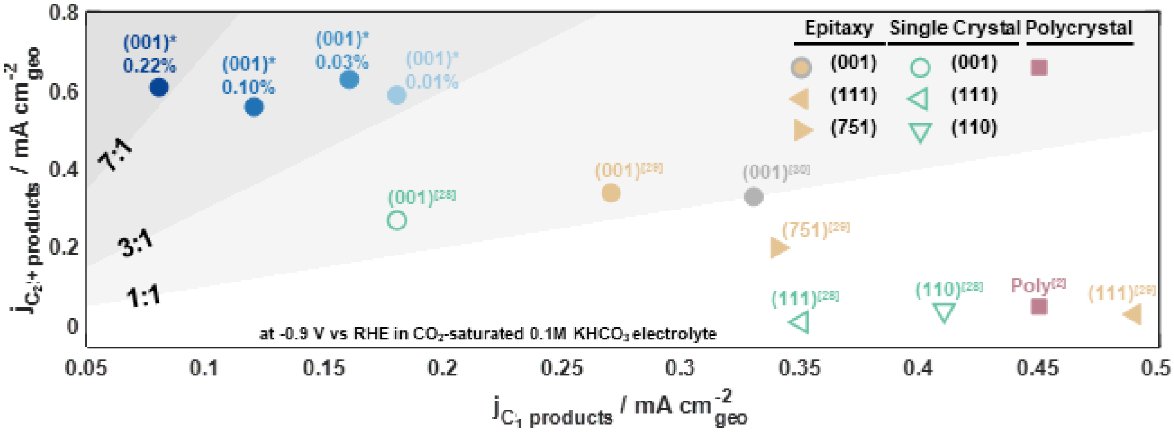

Figure 2.15. Comparison of geometric partial current densities of multi-carbon products and single-carbon products on planar Cu catalysts at -0.9 V vs RHE in CO2-saturated 0.1M KHCO3 electrolyte. Lines indicating a constant ratio of C2+ to C1 partial current density are shown. * indicates this work.

2.6 Comparison to State-of-the-art Catalysts

To examine the trends in CO_2 reduction activity and selectivity for the strained Cu (001) catalysts and compare them with previously reported planar Cu surfaces, we show the geometric partial current density of C_2^+ products vs. that of C_1 products in Figure 2.15. The data is tabulated in Table 2.3. For our strained Cu (001) thin film catalysts, the partial current density for single-carbon products is continuously suppressed as the in-plane tensile strain increases while that for C_2^+ products is rather flat. This leads to a 7-fold higher activity toward C_2^+ products relative to single-carbon products on the 20 nm Cu (001) film catalyst (0.22% tensile strain). In part, the suppression of single-carbon products with increasing tensile strain at the surface could be because of an increase in the rate of hydrogenation of single-carbon intermediates. According to *d*-band theory, the adsorption energy of reaction intermediates, and hence their surface population, can be increased as the density of states near the Fermi level increases upon upshifting of *d*-band center position.[40, 60, 61] Computationally, tensile strain is seen to increase the adsorption energy of CO_2 reduction reaction intermediates, especially *CO, on Cu (001).[18] The predominant hydrogen formation with a higher *d*-band center (Figure 2.13A) indicates that the adsorption energy of *H is also governed by tensile strain on Cu (001). We conclude that upshifting *d*-band center increases the adsorption energy of not only *CO but also *H, as expected from scaling relations.[46] We focus on how the modulation of *H and *CO by strain influences the pathway of CO_2 reduction reaction, since the impact of strain on hydrogen evolution is well demonstrated.[29]

The increase in surface population of *H in the presence of tensile strain may promote hydrogenation of carbonaceous intermediates, e.g. *CO–to–*CHO, leading to reduced desorption of single carbon intermediates and further reduction. It is well-established that the Cu (001) surface facilitates C-C coupling,[42, 43, 44] lead to selectivity above the 1:1 line. A more stable adsorption of *CO on Cu (001) than Cu (111) is found to be energetically favorable to *CO dimerization to the *OCCO intermediate and subsequent C_2^+ products.[18, 45, 62]

Table 2.3. Geometric partial current densities for multi-carbon products and single carbon products on planar model catalysts.

Catalysts	j_C_1 products	j_C_2^+ products
Epitaxial Cu(001) 20nm (this work)	0.08	0.59
Epitaxial Cu(001) 30nm (this work)	0.11	0.53
Epitaxial Cu(001) 40nm (this work)	0.16	0.63
Epitaxial Cu(001) 100nm (this work)	0.18	0.58
Epitaxial Cu(001)[43]	0.27	0.34
Epitaxial Cu(111)[43]	0.49	0.03
Epitaxial Cu(751)[43]	0.34	0.2
Single crystal Cu(001)[42]	0.18	0.27
Single crystal Cu(111)[42]	0.35	0.01
Single crystal Cu(110)[42]	0.41	0.04
Epitaxial Cu(001)[44]	0.33	0.33
Polycrystalline Cu[4]	0.45	0.05

In addition, *CHO formation via hydrogenation of *CO with nearby *H is favored on Cu (001) surface owing to its lower coordination than Cu (111), which in turn increases the coverage of *CHO on the surface.[18] With the increment of *CHO intermediate on the surface, the C-C coupling reaction through OC-CHO or *OHC-CHO are expected to be facilitated producing *COCHO and/or *COCHOH, other selectivity-determining intermediates to C-C bonding products.[32, 63, 64] This reinforces our speculation that the inhibited activity for single-carbon products formation may be because of facile *CHO formation in the presence of strain on Cu (100) surface. We note that epitaxial Cu films in the literature included in Figure 2.15 are over 100 nm in thickness -– at this thickness, mismatch strain would be completely relaxed, resulting in reduced *CO and *H binding energies with respect to the strained film catalysts in this study.

Interestingly, the partial current density for C_2^+ products on the strained (001) Cu film catalysts are substantially higher than those previously reported for Cu (001) catalysts (Figure 2.15). We first presumed that the enhanced activity for C_2^+ products on the film catalysts in this study as compared to the previously reported Cu (001) films results from defects along the edges and sides of the columnar crystallites seen in Figure 2.7D-G. Perhaps similar to these edges, defects at grain boundaries have been shown to play an important role in C-C coupling reaction.[65, 66, 67] To test whether the catalytic activity for C_2^+ products is related to these edge sites, a mild post-growth annealing of the 100nm Cu (001) film is performed at 65°C for 14 hrs to fill the voids, increase columnar grain size, with no change in strain expected.[66]

2.7 Structural Properties And CO_2 Reduction Activities on the Heat-treated Epitaxial Cu (001) Film Catalyst

Figure 2.16A shows AFM images of (i) the as-prepared and (ii) the post-growth annealed 100 nm film catalysts. The AFM height data reveal a collapse of the columnar structure, a reduction of void fraction, and thereby fewer edge sites present the surface after annealing. These outcomes are particularly apparent in the amplitude images in Figure 2.17A-B, in which a decreased density of the columnar grain boundaries upon heat treatment is observed. Consistent with this observation, a densified surface morphology is revealed by SEM imaging after annealing as shown in Figure 2.16B. We confirm that the post-growth annealed 100 nm film catalyst is still purely (001) oriented and exhibits no strain (Figure 2.18A-B), indicating that the epitaxial relationship of the films on the Si (001) substrate is maintained during the mild post-growth anneal.

The surface-area-normalized partial current density for C_2^+ products is modestly reduced in the densified, post-growth annealed 100 nm film catalyst (Figure 2.16C). Because the annealing definitively reduces the exposure of edge sites, this trend suggests that these edge sites contribute some to C_2^+ product formation. The increase in partial current density for single-carbon products and decrease in hydrogen partial current density of the post-growth annealed film may be accounted for by the increase in the area of unstrained (001)–oriented surface in the densified film catalyst. Here we note that the partial current density of Figure 2.16 is normalized by

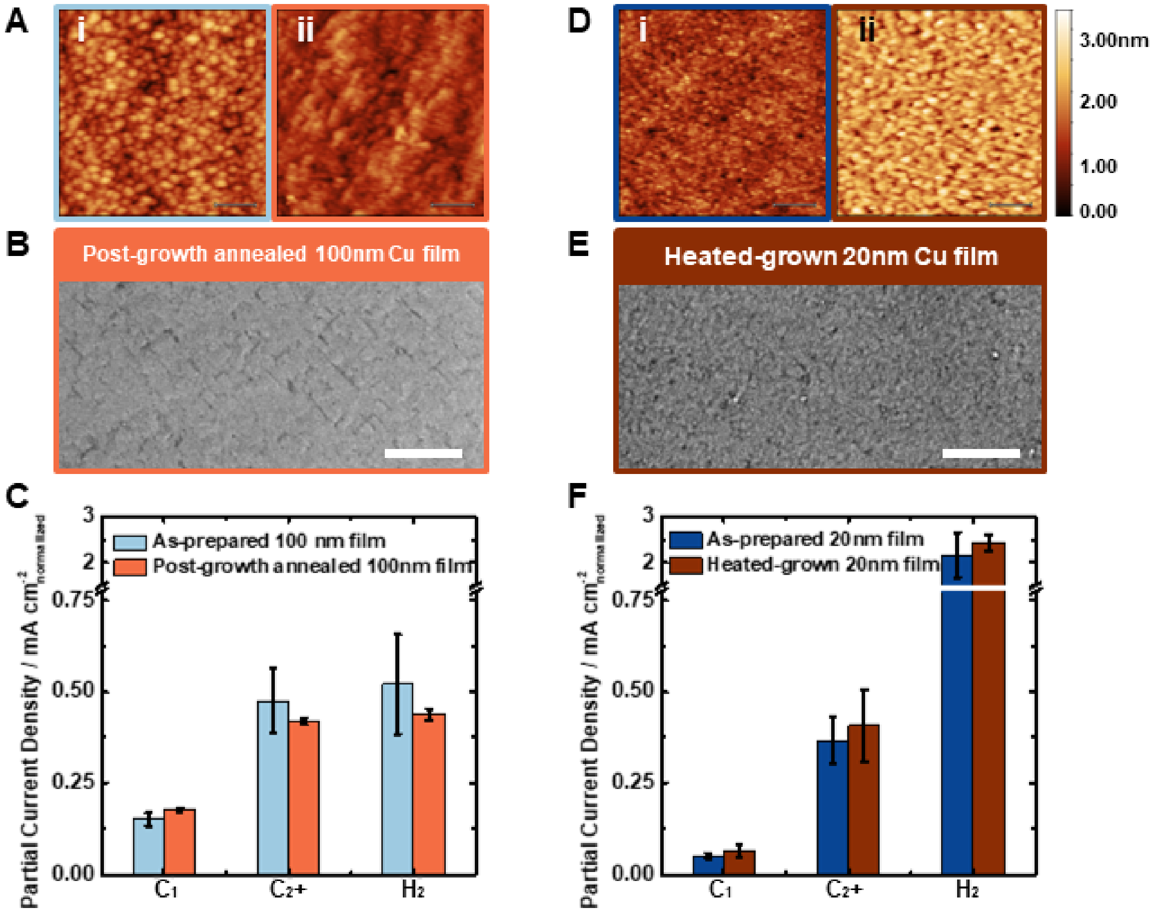

Figure 2.16. A 100nm Cu (001) film with post-growth annealing at 65°C for 14 hrs (orange) and a 20nm Cu (001) film grown at 65°C (dark brown). AFM height images of (A,i) as-prepared 100nm film, (A,ii) post-growth annealed 100nm film, (D,i) as-prepared 20nm film, and (D,ii) the heated-grown 20nm film. Scanned area of 1 um x 1 um at a scan rate of 1 Hz. SEM image of (B) the post-growth annealed 100nm film and (E) the 20nm heated-grown 20nm film. Scale bars indicate 200nm. Comparison of surface-area-normalized current densities for single-carbon, multi-carbon products and hydrogen on (C) the as-prepared and the post-growth annealed 100nm Cu (001) film catalysts and (F) the as-prepared and the heated-grown 20 nm Cu (001) film catalysts.

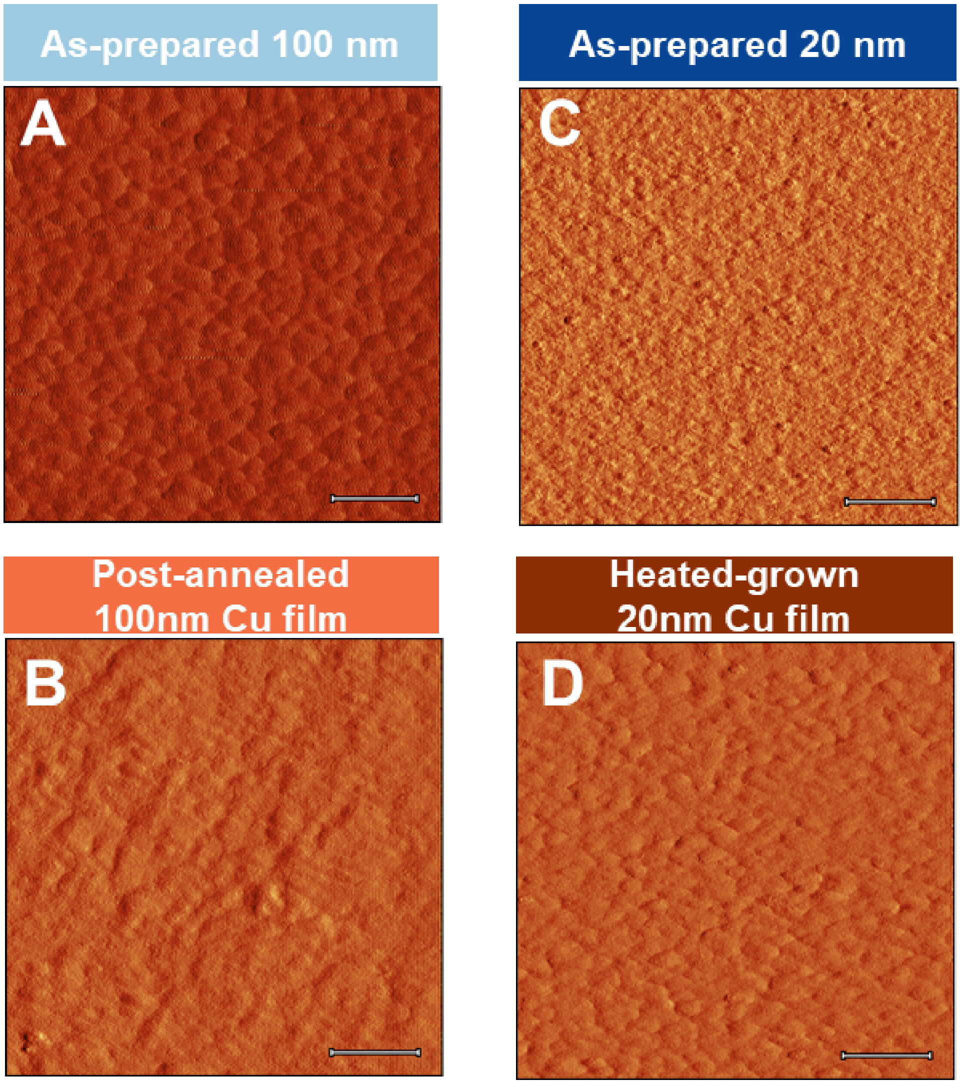

Figure 2.17. AFM amplitude images of the as-prepared and the heat-treated epitaxial Cu (001) films on Si substrate before electrolysis. Scanned area of 1 μm$\times$1μm at a scan rate of 1 Hz. Scale bars indicate 200 nm.

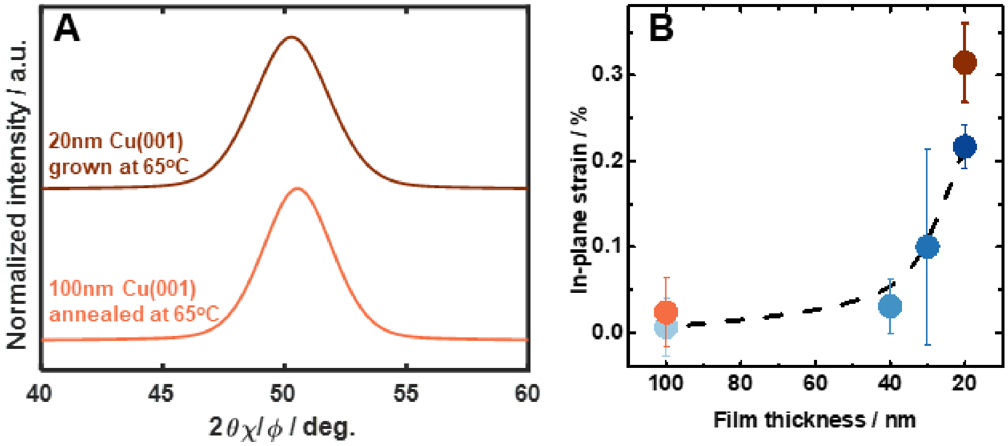

Figure 2.18. Grazing-incidence X-ray diffraction of the epitaxial Cu (001) films on Si substrates. (A) In-plane X-ray diffraction patterns of each film at 0.5° angle of incidence. (B) Corresponding in-plane strain as a function of film thickness.

roughness factor estimated by EDLC (Table 2.4) to exclude possible influence of surface area on this comparison.

Table 2.4. Roughness factor of the as-prepared and the heat-treated Cu (001) films.

Film conditions	Roughness factor by EDLC
As-prepared 20 nm	1.62
Heated-grown 20 nm	1.85
As-prepared 100 nm	1.15
Post-growth annealing 100 nm	1.33

Were the edge sites to dominate catalytic activity towards C_2^+ products, a correlation between the decreasing columnar crystallite size seen in the thinner film catalysts and activity for C_2^+ products would be expected. However, we find rather consistent activity for C_2^+ products across film thickness and increasing activities for HER with thinner films that is in contrast with a previous report.[67] We therefore conclude that we cannot attribute the activity for C_2^+ products predominantly to edge effects.

Secondly, we conjecture that the drop in the activity for single-carbon products on our thinner films is largely attributed to increasing tensile strain. To extend our test of this hypothesis, we grow a 20 nm Cu film on a single crystal Si (001) substrate maintained at 65^{o}C during deposition to increase the expected mismatch strain upon cooling because of the differing coefficients of thermal expansion (CTE).[68, 69]

We compare the surface texture of 20 nm thick Cu (001) film resulting from (i) the baseline room-temperature growth and (ii) the 65°C heated-growth via AFM height and amplitude images, as shown in Figure 2.16D and 2.17C-D. An increase in crystallite size is seen in the heated-growth film, as compared to the as-prepared 20 nm film. The surface morphology ends up similar to the as-prepared 100 nm film. The SEM imaging of Figure 2.16E also shows that the 20 nm film grown at the elevated temperature exhibits reduced void fraction relative to the room-temperature growths (Figure 2.7G). This may suggest fewer edge sites remain on the surface. The modest elevation of substrate temperature works to reduce void fraction, following the SZM.[55] As expected, the heated-grown Cu film maintains (001) oriented crystalline structure and exhibits 0.31% strain (Figure 2.18), larger than the corresponding 20 nm film grown at room temperature (0.22%) because of the increased lattice mismatch due to differing CTE.

However, the differences in activity and selectivity for CO_2 electrolysis between the 20 nm room-temperature and heated-growth film catalysts are marginal, as shown in Figure 2.16F. Even though the surface texture of the 20 nm film catalyst grown at 65°C is quite similar to the as-prepared 100 nm film catalyst, the selectivity of the 20 nm Cu film catalyst grown at 65°C maintains nearly 7-fold enhancement, as estimated by the ratio of current density for C_2^+ products to C_1 products. This result supports our second hypothesis that the tensile strain largely governs the overall CO_2 reduction reaction pathway rather than the amount of edge sites on the catalyst surface. The strain effect may saturate when tensile strain reaches 0.2-0.3% as seen here.

Increased out-of-plane tilting and in-plane twisting is also observed in thinner films as indicated by comparing the full width half maximum (FWHM) of the rocking curve and phi scans in Figure 2.19, respectively. Moreover, the heated-grown 20 nm Cu film shows increased misorientation, while that of the post-growth annealed 100 nm Cu film decreases. The increment in the misorientation may result in an increase in defect density (e.g. step and kink sites) at the surface of the thinner films, resulting from distortion of epitaxial building blocks with respect

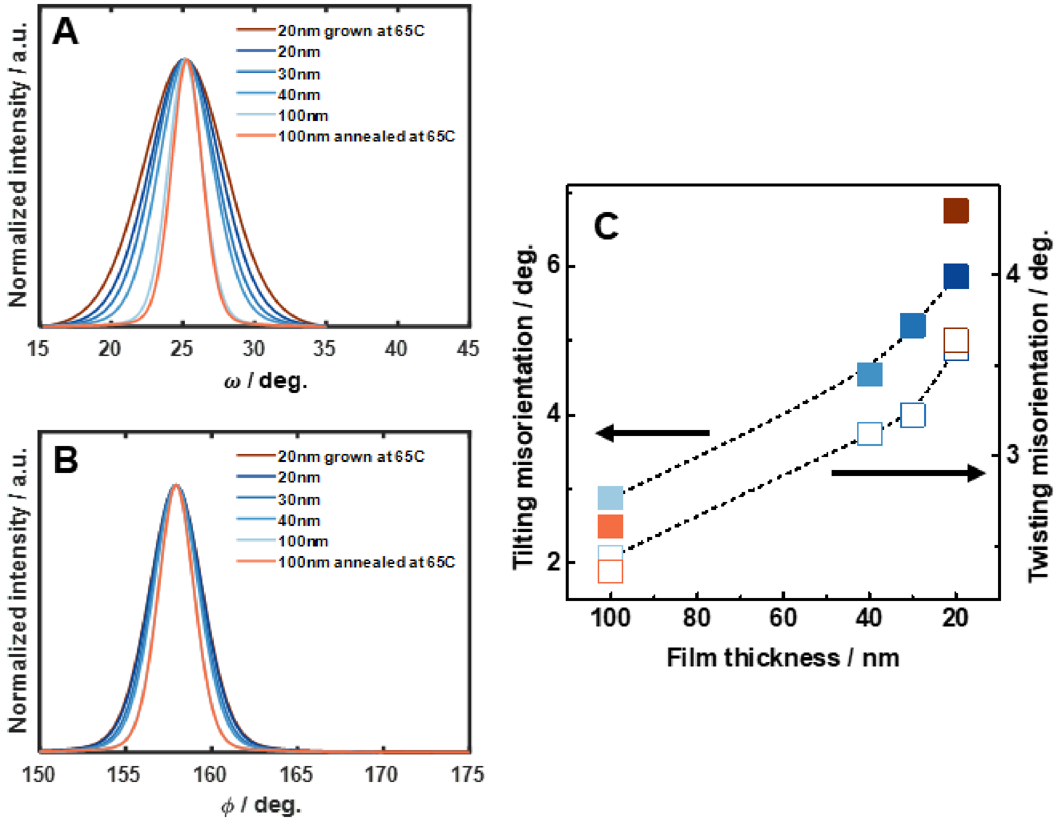

Figure 2.19. Crystalline structure of each Cu film (A) Rocking curves and (B) phi scans of each Cu film with respect to film thickness and deposition condition. (C) Corresponding tilting and twisting misorientation of the Cu films.

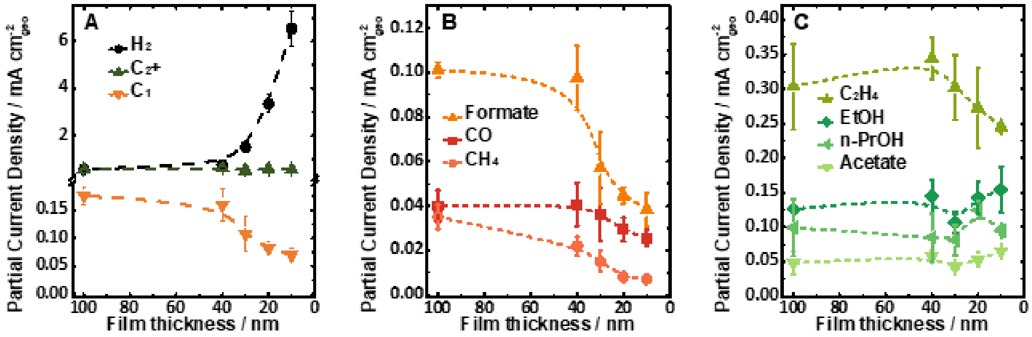

Figure 2.20. CO_2 reduction activity of strained Cu (001) surfaces as a function of film thickness. Geometric partial current densities of (A) hydrogen, multi-carbon (C_2^+), and single-carbon (C_1) products, (B) single-carbon products and (C) multi-carbon products formation at -0.9 V vs RHE in CO_2-saturated 0.1M $KHCO_3$ electrolyte.

to each other.[70] Growing thicker epitaxial films beyond the critical thickness will lead to the generation of threading dislocations that relax the strain energy[71, 72] and increase the microstrain. However, the microstrain in the films here is largest for the thinner films, suggesting it is dominated by the twist/tilt misorientations in the early stages of film growth. We perform additional CO_2 electrolysis on 10 nm Cu (001) films, where a further upshifted *d*-band center is expected (Figure 2.20). We observe that the 10 nm film follows the overall trend for partial current densities of hydrogen, multi-carbon, and single-carbon products. However, diminishing changes are seen in the partial current densities for carbonaceous products on the 10 nm films vs the thicker films. This is consistent with Figure 2.7C, which shows that the shift in *d*-band center position, and hence the catalysis, appears to saturate at higher strains.

Even so, the increasing misorientation in our thinner film catalysts does not correlate with an increased activity for C_2^+ products, although C-C coupling can be expected with increasing step and kink sites revealed on the surface.[73] This further suggests that the defect density at the strained surfaces may not be the dominant factor in the change in the CO_2 reduction reaction activity seen in Figure 2.13 and 2.15. The larger misorientation of our film catalysts (e.g. 100 nm Cu film, FWHM=2.87°) with respect to previously reported (001) Cu films on Si (FWHM=2.1°)[44] may be responsible for the difference in the partial current density for C_2^+ products between our film catalysts and the other Cu (001) model catalysts (Figure 2.15).

2.8 CO_2 Reduction Reaction Mechanism under Tensile Strain

Combining our experimental observations with recent theoretical calculations suggests that the reaction mechanism of CO_2 reduction on Cu (001) is quite strain sensitive. The reaction scheme in Figure 2.21A seeks to identify the role of strain while taking into account previously proposed reaction pathways.[28, 31, 33, 18, 11, 74] We draw *COO–, *OCHO, and *H as starting intermediates since they are the first CO_2 reduction intermediates bound to the surface.

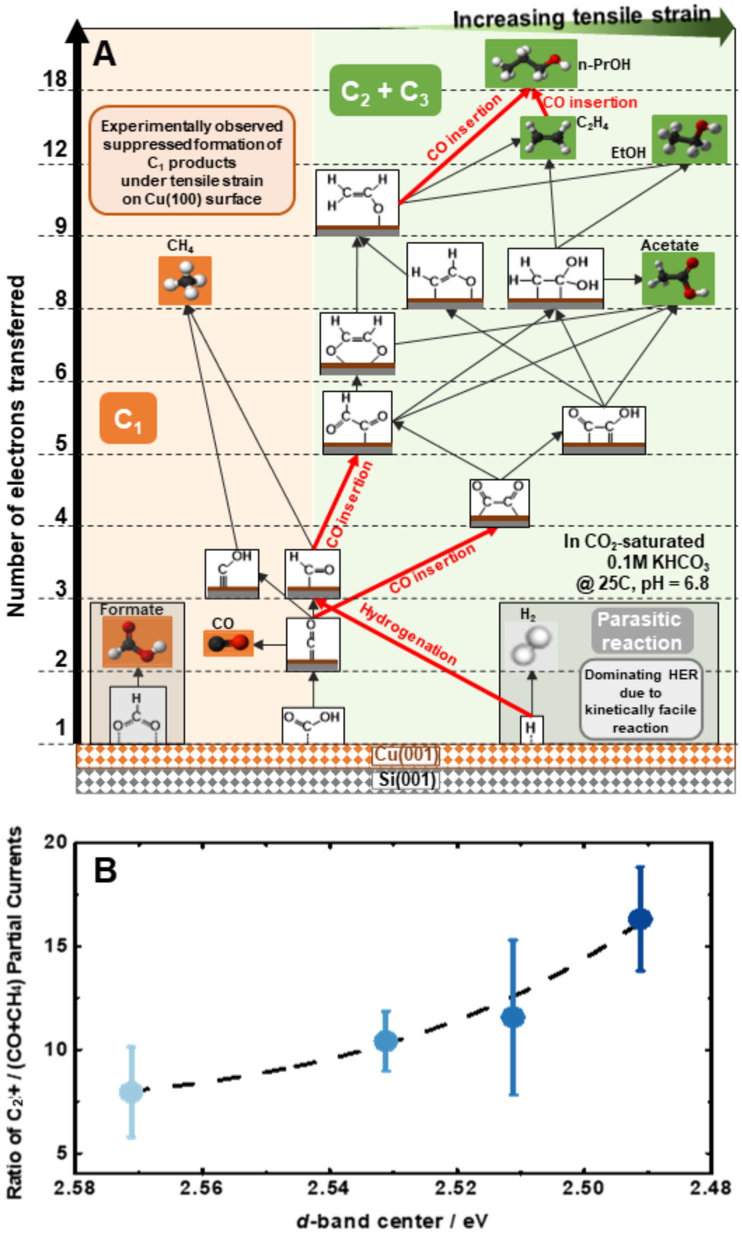

Figure 2.21. Effect of in-plane tensile strain on CO_2 reduction. (A) Summarized CO_2 reduction reaction pathways including parasitic hydrogen evolution reaction.[28, 31, 33, 18, 11, 74] The numbers on y-axis represents number of electrons transferred upon reaction coordinates. All single-carbon products are in the orange color regime and multi-carbon products are in the green color regime. All lines drawn here is a proposed reaction pathway combined recent theoretical insights. Red line indicates a proposed CO insertion reaction or hydrogenation to carbonaceous intermediates and black line indicates proton-electron transfer reaction. (B) Ratio of the geometric partial current density for multi-carbon products to CO and CH_4 with respect to *d*-band center position.

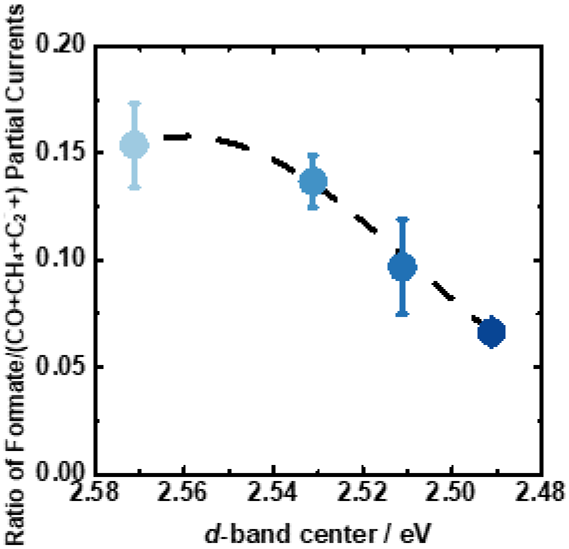

Figure 2.22. Ratio of geometric partial current density for formate to other carbonaceous products with respect to *d*-band center position.

From our results above and previous computational results,[18] we expect an increasing population of both *CO and *H on a tensile–strained Cu (001) surface, promoting not only the *CO coupling reaction but also hydrogenation of *CO to *CHO.[75] This may result in the suppressed formation of single-carbon products and facilitate C–C coupling kinetics,[63] although kinetically-facile HER consumes most of electrons at the highest degrees of strain. The Cu (001) surface is known to have a lower energy barrier for CO_2 reduction to *CO than CO_2 to *OCHO, the formate intermediate, that intrinsically guides the reaction path to hydrocarbon or alcohol formation instead of formate on the strain-free surface.[76] The selectivity to formate is further suppressed on Cu (001) surface with upshifting *d*-band center position, as shown in Figure 2.22, which is probably attributed to the increased surface coverage of *CO and *H. We speculate that hydrogenation of *CO to *CHO can be promoted owing to abundant[77] *H upon introducing tensile strain. Therefore, the increased population of both *CO and *CHO may lead to facile transformation of single-carbon intermediates to multi-carbon intermediates and, thus, accelerate *CO dimerization and/or *CO insertion into *CHO that generates either *OCCO, *OCCHO, or *OCCOH.[28, 31, 33, 18, 74]

The reaction path beyond these C_2 intermediates branches into multiple, complex reaction paths, as shown in Figure 2.21A. The subsequent proton-electron transfer reactions with C-C containing intermediates produce C_2^+ products such as acetate, C_2H_4 and EtOH.[31, 33, 34, 78] The reaction path for C_3 products such as n-PrOH is proposed to be through coupling of *CO with *$OCHCH_2$ or C_2H_4 molecules nearby.[28, 74] We tentatively speculate that the modestly decreasing C_2H_4 activity and rather steady alcohol formation rate (Figure 2.13C) with increasing tensile strain may be attributed to the increasing distance between Cu atoms along that may hamper substitution of oxygen in *$OCHCH_2$, resulting in suppressed C_2H_4 formation.[28, 31, 63]

Ultimately, we conclude that the manipulation of the *d*-band center position of Cu (001) by tensile strain modulates the reaction pathway and alters the product distribution as seen in our experiments above. Comparing activity for C_2^+ products to the activity of CO and CH_4 formation is informative as the reaction path selected after *CO formation heavily relies on the *CO coverage.[79] Figure 2.21B shows ratio of partial current density for C_2^+ products compared to C_1 products, CO and CH_4 with respect to *d*-band center position. It is clearly seen that selectivity for the C_2^+ products is higher on more strained films, where a stronger adsorption energy for reaction intermediates is expected due to the upshifted *d*-band center. Evidently, the ample *CO coverage resulting from tensile strain leads to C-C coupling that hampers both CO and CH_4 formation. We propose that the selectivity for C_2^+ products on Cu (001) surface with higher *d*-band center is largely due to the increased adsorption energy for both *CO and *H, which together with their increasing surface coverages suppresses reaction pathways toward single-carbon products.

2.9 Summary

In summary, we provide quantitative analysis of electrochemical CO_2 reduction on model strained Cu (001) surfaces to demonstrate strain engineering as a path to tune the product distribution. Increasing tensile strain is observed as the film thickness of epitaxially-grown

Cu (001) film on Si (001) single crystal substrates decreases. The tensile strain shifts the *d*-band center toward the Fermi level. The change in electronic structure and resulting adsorbate interaction suppresses the kinetics for CO_2 reduction to single-carbon products, while the activity for C_2^+ products is steady. The higher *d*-band center is positively correlated overall to enhancing selectivity for C_2^+ products relative to CO and CH_4, suggesting an increase in adsorption energy and surface coverage of *CO and *H. At the same time, due to the linear scaling relation between *CO and *H, as tensile strain increases the increasing favorability of hydrogen adsorption leads to hydrogen evolution outstripping the Faradaic current for CO_2 reduction. These experimental demonstrations of the role of strain in model catalysts facilitate the rational design of nanoparticulate CO_2 reduction electrocatalysts. The results of this work highlight the opportunity to design electrocatalysts explicitly using strain engineering to focus the reaction pathway toward highly energy dense CO_2 reduction products.

2.10 Acknowledgement

Chapter 2, in full, is a reprint of the material ”How Strain Alters CO_2 Electroreduction on Model Cu Surfaces” as it appears in ACS Catalysis, Taewoo Kim, Rishi E. Kumar, Jeffrey A. Brock, Eric E. Fullerton, and David P. Fenning, 2021, 11 (11), 6662. The dissertation author was the primary investigator and author of this material.

Chapter 3

Effect of Surface Morphology: Shifting CO_2 Reduction Products Selectivity

3.1 Enhanced Multi-carbon Products Selectivity on the Mesostructured Cu Catalyst

The electrochemical conversion of CO_2 to hydrocarbons and alcohols for use as a renewable energy storage medium is a promising approach to CO_2 utilization and energy sustainability. Herein, we demonstrate that the selectivity of an electrochemically reduced $Cu(OH)_2$ nanowire catalyst towards C_2-C_3 compounds (ethylene, EtOH and n-PrOH) is systemically modified by surface morphology, which is governed by the electrolysis potential. The total Faradaic efficiency of CO_2 reduction to C_2-C_3 compounds is found to be 38% at a moderate potential of -0.81 V vs RHE, and stable electrocatalytic performance is observed for 40 hrs of CO_2 electrolysis. Electro- and physicochemical analysis indicate that the $Cu(OH)_2$ nanowires are completely reduced to metallic Cu forming a mesostructured catalyst after a few minutes of electrolysis. The shift in product selectivity is strongly correlated with this change in mesoscale catalyst morphology, offering additional dimensionality and multiple length scales for catalyst design to achieve efficient CO_2 reduction to valuable C_2-C_3 compounds, especially alcohols.

3.2 Introduction

CO_2 emissions from expanding use of fossil fuels and cement production continue to worsen global warming. To keep global temperatures from increasing above 2 °C, a drastic decline of global carbon emissions (50%) is necessary, requiring yet-to-be-developed technologies.[80, 81] One promising strategy utilizes exhausted CO_2 as an energy storage medium coupled with intermittent solar and wind renewable energy resources.[82, 83, 84] However, the difficult kinetics of CO_2-to-fuel reactions require an effective catalyst, and no sufficiently active, selective, and durable catalyst has been identified.[85, 4] Selectivity continues to be a particularly challenging issue[86, 87] given the many intermediates in the reduction of CO_2 to fuels. Among the CO_2 reduction products, C_2 and C_3 compounds such as ethylene, EtOH, and n-PrOH exhibit higher energy densities and commercial value as compared to C_1 compounds such as methane and carbon monoxide (CO).[88, 89, 90] Furthermore, recycling of CO_2 to highly-valued synthetic precursors can lead to net zero carbon emissions, promising a sustainable carbon resource.[91, 92] Development of active catalysts with high selectivity is necessary to enable a cost-competitive solar-driven CO_2–to–fuel conversion with minimal post-separation processes.

The catalytic activity of Cu electrodes has been the subject of extensive study, owing to their production of hydrocarbons and alcohols with promising reaction rates.[85, 86] However, despite their general activity, Cu electrodes are hampered by their poor selectivity, which consequently yields undesired products and low energetic efficiency.[4, 93] The wide range of C_1-C_3 compounds that is produced on polycrystalline Cu electrode can be ascribed to the heterogeneity of catalytic sites present.[4] Moreover, the rapid degradation of electrocatalytic performance during electrolysis remains a challenge.[22, 94, 95]

The distribution of C_1-C_3 products depends on the micro- and nanostructure of the Cu catalyst.[13, 96, 97, 98, 99, 100, 101, 21] In porous electrodes, pore depth and diameter can affect the selectivity of CO_2 reduction.[96, 97] It is well established in heterogeneous catalysis that pore structure, for example of zeolite catalysts, confines intermediates and leads to an increase in their residence time that enhances product selectivity.[98, 99, 100] In the particular case of CO_2 reduction, reaction selectivity can be improved by reducing Cu_2O materials to create catalysts that present a highly-defective, large-area surface.[101] Such oxide-derived catalysts reveal higher Faradaic Efficiency (FE) of formic acid (31.9%) and CO (20.7%) at -0.65 V vs RHE as compared to polycrystalline Cu electrode[4] (8.6% and 18.4%, respectively) and sustain stable current density and energetic efficiency.

Achieving higher hydrocarbon and alcohol products efficiently remains a significant challenge. Studies on model single–crystal Cu catalysts reveal a strong dependence on crystal orientation for CO_2 reduction.[13] Ethylene formation is favorable on Cu (100), whereas methane is mainly generated on Cu (111). Cu nanoparticle catalysts with rough surfaces can take advantage of higher order facets with undercoordinated sites and show a higher ratio of C_2 to C_1 products than planar Cu catalysts.[21] Selective CO_2 reduction toward C_2 compounds can be also produced by electrodeposition of high surface area Cu catalysts.[22] The favoring of C_2 compounds on such surfaces (C_2H_4 (33.3%) and C_2H_6 (3.7%) at -1.1 V vs RHE) can be attributed to not only the higher specific surface area of the electrode but also suppressed CH_4 formation. Alcohols, as easily-stored and energy dense liquids, are of particular interest. Planar Cu catalysts show a FE of only 6% for EtOH and 4% for n-PrOH at -1.0 V vs RHE.[4] On the other hand, oxide-derived Cu catalysts achieve a 16.4% FE for EtOH at -1.0 V vs RHE.[102] The increased formation of alcohols has been ascribed to the increase in local pH at the electrode-electrolyte interface of these porous catalysts.[102, 103, 104] Furthermore, controlling the density of surface defects can enhance the formation of n-PrOH. Agglomerated Cu nanocrystals exhibit a partial current density for n-PrOH that is $\sim$25 times higher than on a planar Cu electrode at -0.95 V vs RHE, leading to 10.6% of FE for n-PrOH.[105]

Interestingly, the formation of C_2-C_3 alcohols can be favored on nanowire catalysts, where multiple geometric design variables are available such as diameter and aspect ratio.[23, 106, 107] A CuO nanowire array electrode shows the CO_2 conversion to EtOH and n-PrOH with 5% and

9% of FE at -1.1 V vs RHE, respectively, while hydrogen evolution was suppressed (44% FE). The nanowire morphology might contribute to favored CO dimerization due to the increased local pH close to the catalyst surface, leading to selective CO_2 reduction to higher $C2^+$ products, albeit inefficiently at low overpotential.[4, 101, 107, 108, 109]

In this study, we demonstrate an improved electrocatalytic activity and selectivity for CO_2 reduction to C_2-C_3 products using the potential-dependent morphology of a mesostructured Cu catalyst that is derived from $Cu(OH)_2$ nanowires. These mesostructured catalysts exhibit selective production of C_2-C_3 hydrocarbons and alcohols at moderate overpotential. The total FE for alcohols, and n-PrOH in particular, is enhanced relative to the state-of-the-art for Cu catalysts.[4, 101, 103, 105, 23, 107] FE for both EtOH and n-PrOH is $\geq$ 10% with $\geq$ 1 mA cm^{-2} and $\sim$0.5 mA cm^{-2} partial current density, respectively, at -0.81 V vs RHE. Nanowire $Cu(OH)_2$ catalyst precursors are prepared by a facile solution-immersion process, and mesostructured Cu catalysts are formed by reduction of the $Cu(OH)_2$ nanowires after a few minutes at CO_2 electrolysis potentials. The Cu catalyst morphology derived from $Cu(OH)_2$ reduction appears to contribute significantly to the enhanced catalytic performance. The catalysts are also stable for long-term bulk electrolysis, retaining $\geq$ 94% of the original FE for n-PrOH for 40 hrs. The results herein indicate that highly selective and stable CO_2 electroreduction catalysts can be achieved by formation of mesostructured catalysts via reduction of $Cu(OH)_2$ nanowires at select potentials, owing to the change in surface properties and/or mesostructure that arises during electroreduction.

3.3 Experimental Procedures

Fabrication of $Cu(OH)_2$ nanowire electrodes. Cu foil (0.1 mm, 99.9999%, Alfa Aesar) is used as a substrate. The substrate is first mechanically polished using sandpaper (400G, SiC) and cleaned in acetone, iso-propanol, and then distilled water under sonication for 5 min each. $Cu(OH)_2$ nanowire electrodes are fabricated using a one-step solution-immersion method

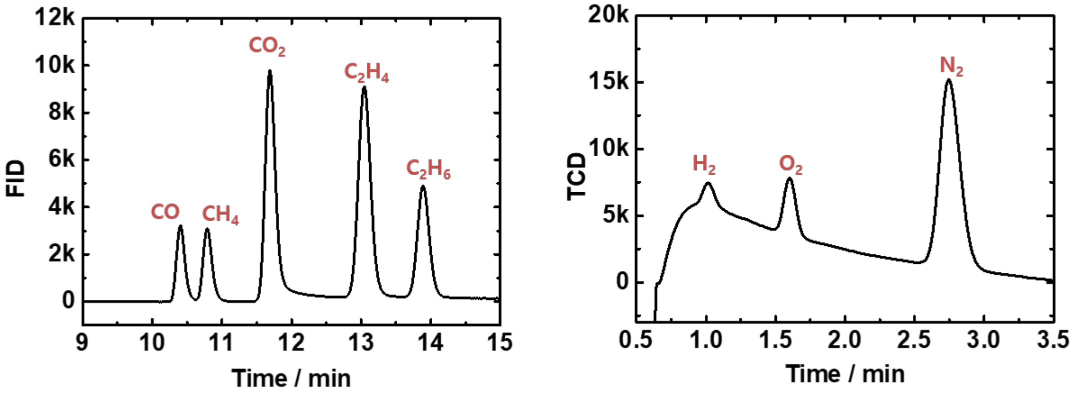

Figure 3.1. GC spectrums of gas compounds from FID and TCD channels using calibration gas.

reported previously.[110] Briefly, a 2.67 M aqueous solution of NaOH ($\geq$ 97.0%, Sigma-Aldrich) is mixed with 0.13 M $(NH_4)2S_2O_8$ ($\geq$ 98%, Sigma-Aldrich) solution while stirring. The mixture is allowed to cool to room temperature under vigorous stirring, and the mechanically polished Cu foil is immersed into the solution for 10 min without agitation. The as-prepared $Cu(OH)_2$ nanowire electrodes are rinsed with distilled water several times and dried with nitrogen. For comparison with the nanostructured catalyst, a planar Cu electrode is mechanically polished, and then electropolished under constant potential of 4 V vs Ti wire (99.99%, Alfa Aesar) at room temperature for 5 min in phosphoric acid (85%, Macron Fine Chemicals).

Catalyst Characterization. The morphology and microstructure of the $Cu(OH)_2$ nanowire electrodes before and after CO_2 electrolysis are obtained by scanning electron microscope (SEM, ZEISS, Sigma 500). The crystallinity and phase are characterized by X-ray diffraction (XRD, Bruker, VANTEC 500). The electrochemical analyses of the catalysts are executed using a potentiostat (VSP-300, bio-logic). Surface roughness factors are examined by measuring electrochemical double-layer capacitance (EDLC) in 0.1 M $KHCO_3$ (99.95%, Sigma-Aldrich) electrolyte under CO_2.

Carbon dioxide electrolysis. The electrochemical reduction of CO_2 is conducted in a customized electrochemical cell based on the design of Kuhl et al.[4] using a three-electrode setup at room temperature and ambient pressure (see section 1.3.1 for details). The working

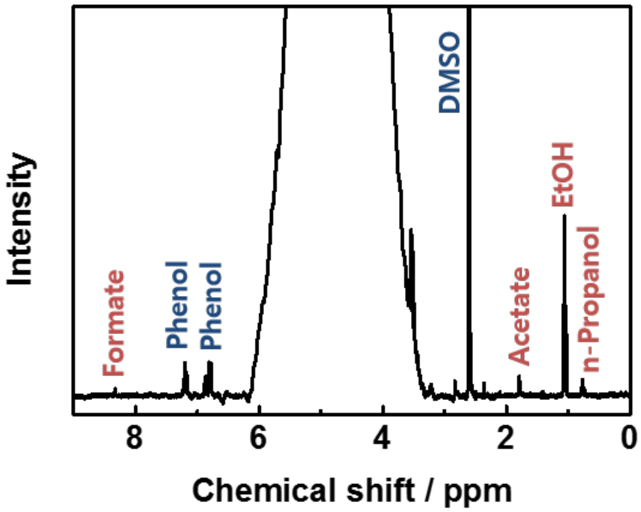

Figure 3.2. ^{1}H NMR spectrum of electrolyte after electrolysis at -0.85 V vs RHE in CO_2-saturated 0.1 M $KHCO_3$ solution.

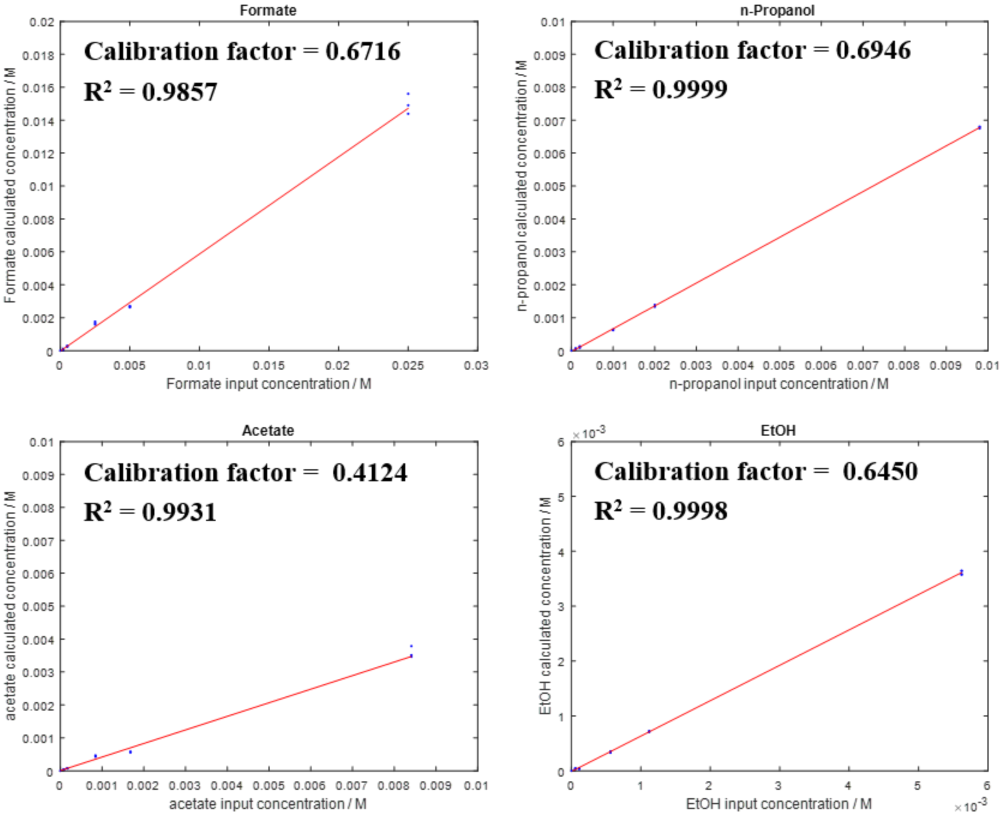

Figure 3.3. Calibration curves for the liquid products.

and counter electrode compartments are separated by an anion exchange membrane (Selemion AMV, AGC Inc.). Ag/AgCl (in KCl gel, Pine Research) and Pt gauze (100 mesh, 99.9% metal basis, Sigma-Aldrich) are applied as a reference electrode and counter electrode, respectively. CO_2-saturated aqueous 0.1 M $KHCO_3$ solution ($\geq$ 99.95% metal basis, Sigma-Aldrich) is used as an electrolyte, and CO_2 is continuously purged into the electrolyte at flow rate of 5 sccm during CO_2 electrolysis, controlled via mass flow controller (Smart Track 100, Sierra). The potentials reported herein are corrected by 85% automatic iR-compensation and 15% manual compensation and converted to the reversible hydrogen electrode (RHE) scale.[4] All gas products formed in the working electrode compartment are collected directly into a gas-sampling loop and quantified by online gas chromatography (GC, SRI 8610C, Sri) (Figure 3.1). In addition, ^{1}H nuclear magnetic resonance (NMR, ava 300, Bruker) is used to identify and quantify the liquid products (spectra and calibrations shown in Figure 3.2 and 3.3). Analysis of liquid products is carried out after completion of CO_2 electrolysis, typically 1 hr in duration.

All potentials in this study are shown against the reversible hydrogen electrode (RHE), and corrected with 85% iR-compensation in addition to 15% post-correction using the following equations: $E_{100\%iR-compensated} = E_{85\%iR-compensated}$ -$15\% \times R_{average} \times I, where V_{100\%iR-compensated}$ and $V_{85\%iR-compensated}$ are the corrected potentials (in volts), $R_{average}$ is the average resistance before and after 1 hr electrolysis (in Ohm), and I is the averaged current at plateau (in amps).[4] The electrochemical double-layer capacitance of the as-prepared catalysts are measured by using cyclic voltammograms in aqueous CO_2-saturated 0.1 M $KHCO_3$ solution with different scan rates in the range from 20 to 120 mV s^{-1}. The current densities are then plotted as respect to the scan rate to obtain a linear plot. The roughness factor is obtained by the ratio of the slope of the as-prepared catalyst to that of the pristine Cu foil. We define the roughness factor for the pristine Cu foil as 1.

At least 2 measurements are carried out at each potential in an attempt to ensure the repeatability of the electrode and compensate the effect of differences in factors such as the electrode surface condition between electrolyses. All gas products are quantified by online gas chromatography (GC, SRI 8610C, SRI) with a molecular sieve 5A and a haysep D column using Ar as a carrier gas. A thermal conductivity detector (TCD) for H_2 detection and a flame ionization detector (FID) for CO, CH_4, CO_2, ethylene, and ethane detection are applied. The GC is calibrated by using calibration gas mixtures (Precision calibration mixtures, GASCO) and the set of representative chromatograms are shown in Figure 3.1. The standards contain 100 ppm of CO, methane, ethylene, ethane, and H_2, and 405, 2500, and 17000 ppm of CO_2, oxygen and nitrogen, respectively. The high signal-to-noise in Figure 3.1 indicates the setup's instrumental sensitivity to CO_2 reduction products. To ensure that the data is collected in a steady-state condition, the analysis is carried out during the current plateau after 10 min of electrolysis and the FEs of each product are averaged over 3 GC injections during 1 hr CA measurements. The FEs and the standard-deviations between electrolysis are shown in Table 3.2. The equations to calculate the FE for the formation of each product can be found in the paper.[5]

The liquid products from both working and counter electrode compartments are analyzed at the end of the electrolysis using ^1H nuclear magnetic resonance (NMR) spectroscopy. To prepare sample of the electrolyte, 700 μl of electrolyte solution is mixed with 300 μl of internal standards solution which consists of 0.5 mM of Phenol (99%, liquified, Fisher scientific) and 23 mM of DMSO ($\geq$ 99.9%, Sigma-Aldrich) dissolved in D2O (99.8 at%, TCI America), and then transferred to a NMR sample tube. ^1H NMR is performed with a 300 MHz spectrometer (ava 300, Bruker) to analyze the liquid products. A typical NMR spectrum and the peak assignments for the liquid products are shown in Figure 3.2 and Table 3.3, respectively. Each spectrum is collected after 256 continuous scans. The peak areas are integrated, and the relative peak area of each product is calculated by comparing with that of the internal standard. The concentration of the liquid products is determined using the calibration curves shown in Figure 3.3.

Table 3.1. Double layer capacitance of the as-prepared electrodes and other electrodes with their respective roughness factors. (* Selected C_2-C_3 compounds: ethylene, ethane, EtOH, and n-PrOH, ** this work)

Electrodes	Capacitance / mF cm^{-2}	Roughness factor	FE for selected C_2-C_3 compounds* at -0.81 V vs RHE
Pristine Cu foil**	0.03	1.00	-
Electropolished planar Cu**	0.13	3.83	2.60%
$Cu(OH)_2$ nanowire**	2.39	79.80	-
Mesostructured Cu (at -0.81 V vs RHE) **	1.12	37.33	35.48%
Mesostructured Cu (at -1.08 V vs RHE) **	0.73	24.33	2.18%
Cu foil[4]	-	2	1.84%
Annealed Cu[101]	13.90	475	19.9%
Electrodeposited Cu_2O[103]	0.14	4.7	12%
Agglomerated Cu Nanocrystals[23]	0.70	24	37.1%

Table 3.2. Faradaic efficiencies of the electrochemical CO_2 reduction products over the mesostructured Cu catalyst.

Potential (RHE)	j (mA cm^{-2})	H_2	CO	Methane	Ethylene	Ethane	Formate	Acetate	EtOH	n-ProH	Total FE
-1.08	39.60	79.27 (1.80)	0.05 (0.01)	0.05 (0.05)	0.90 (0.29)	0.03 (0.01)	-	0.04 (0.01)	1.09 (0.24)	0.11 (0.13)	81.66
-0.93	37.52	79.57 (6.46)	0.05 (0.01)	0.01 (-)	0.44 (0.11)	0.07 (0.04)	-	0.04 (0.01)	0.95 (0.11)	0.21 (0.21)	81.32
-0.85	10.55	43.92 (5.81)	0.54 (0.35)	0.03 (0.01)	12.47 (5.08)	1.26 (1.01)	0.38 (0.02)	1.26 (0.77)	10.39 (0.19)	1.81 (0.03)	72.25
-0.81	6.85	42.74 (1.34)	2.06 (0.53)	-	10.60 (1.37)	3.37 (0.74)	8.94 (2.43)	2.18 (0.17)	9.16 (1.43)	12.36 (1.10)	91.40
-0.75	2.29	34.00 (1.87)	7.73 (0.84)	-	5.67 (1.24)	1.84 (0.01)	25.01 (0.08)	1.89 (0.01)	8.23 (4.98)	11.22 (0.49)	95.59
-0.66	1.01	16.27 (5.61)	20.38 (4.70)	-	3.08 (0.73)	1.13 (0.63)	47.38 (7.57)	2.38 (0.39)	4.41 (3.04)	4.79 (3.58)	99.82
-0.57	0.66	17.90 (4.27)	29.71 (4.84)	-	0.73 (0.02)	0.89 (-)	35.61 (2.40)	2.54 (0.67)	-	-	87.38
-0.45	0.23	53.69 (11.31)	19.92 (5.84)	-	-	-	-	-	-	-	73.60

3.4 Evolution of the Mesostructured Cu Catalysts

During synthesis, a dense layer of $Cu(OH)_2$ nanowires develop on the surface of the Cu foil substrate with random orientation as shown in Figure 3.4A. The randomly-oriented nanowires have a length of over 7 μm and a diameter in the range of 150–400 nm. The crystallinity of the initial $Cu(OH)_2$ nanowires is confirmed by X-ray diffraction (XRD), with peaks indexed

Table 3.3. NMR peak assignments for CO_2 reduction products and standards.

Compounds	Proton (marked in bold font)	Chemical Shift (ppm)	^{1}H splitting	Coupling Constants (Hz)
Formate	HCOO-	8.34	Singlet	-
Phenol	-	7.2	Triplet	7.97
DMSO	-	2.6	Singlet	-
Acetate	$CH_3C(=O)O$-	1.79	Singlet	-
EtOH	CH_3CH_2OH	1.06	Triplet	7.04
n-Propanol	$CH_3CH_2CH_2OH$	0.76	Triplet	7.42

to the orthorhombic $Cu(OH)_2$ (COD card No. 9011547) as shown in Figure 3.4B (bottom, filled squares). Substrate peaks from the Cu foil are marked with filled triangles (COD card No. 9012043).[111, 112, 113]

The operating Cu catalyst forms in situ by reduction of the $Cu(OH)_2$ nanowires within 10 minutes at CO_2 electrolysis potentials. After 1 hr of CO_2 electrolysis at -0.75 V vs RHE, ex situ XRD reveals no crystalline $Cu(OH)_2$ peaks remain, indicating complete reduction of hydroxide during CO_2 electrolysis (Figure 3.4B). Only metallic Cu and Cu_2O peaks appears in the “after electrolysis” diffraction pattern in Figure 3.4B, where a thin, spontaneous Cu_2O layer forms after removing the sample from the electrolyte and en route to diffractometry. No systematic variation in the XRD pattern of the reduced Cu catalysts are observed after 1 hr of CO_2 electrolysis as the electrolysis potential is varied from -0.45 to -1.08 V vs RHE (Figure 3.4C), suggesting similar crystallinity amongst catalysts produced over a wide of potentials. Cu_2O peaks are also measured on pristine Cu foil, indicating XRD detection of a native oxide layer in all cases (Figure 3.4C and D). The $Cu(OH)_2$ diffraction peaks disappear after 10 min of reduction at moderate potential (-0.81 V vs RHE) as shown in Figure 3.4D. Electrochemical impedance spectroscopy (EIS) measurements confirms the transition during CO_2 electrolysis from a resistive $Cu(OH)_2$ surface to a reduced Cu surface within 10 minutes (Figure 3.6). The operating Cu catalysts develop morphologies distinct from the original $Cu(OH)_2$ nanowire morphology after CO_2 electrolysis for 1 hour, with the morphology relatively unique to each reduction potential.

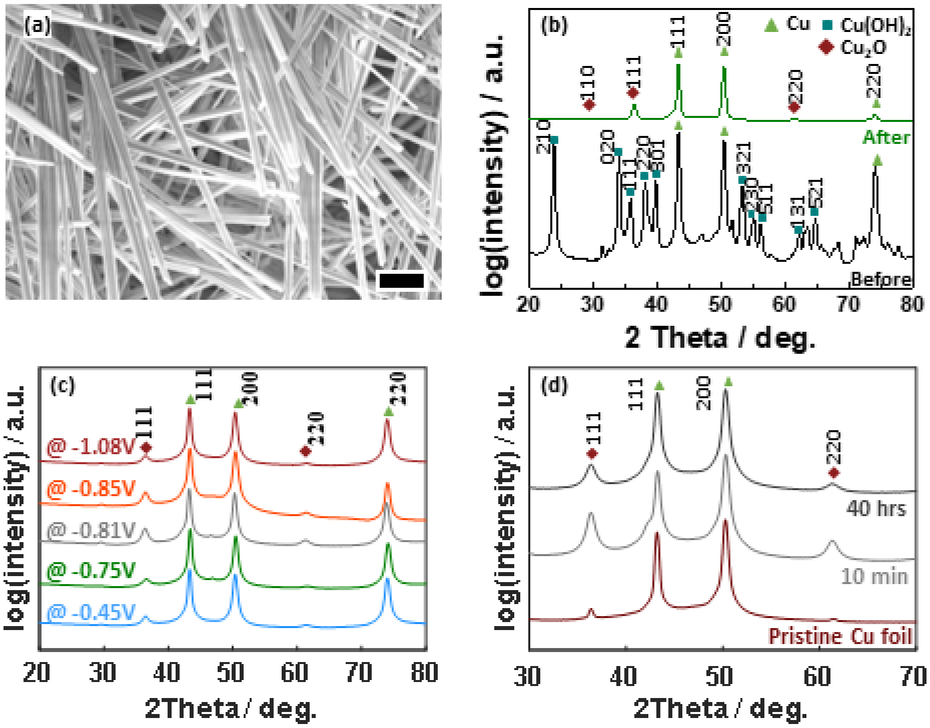

Figure 3.4. Structural properties of Cu(OH)$_2$ nanowire precursors and operando catalysts. (A) 45^o-tilted SEM surface view of Cu(OH)$_2$ nanowires on Cu foil. Scale bar 1 μm. X-ray diffraction patterns of (B) Cu(OH)$_2$ nanowires on Cu foil before CO$_2$ electrolysis and after 1 hr of CO$_2$ electrolysis at -0.75 V vs RHE, (C) The operando Cu catalysts after 1 hr of CO$_2$ electrolysis for all potentials measured, (D) The pristine Cu foil (bottom), the reduced Cu(OH)$_2$ electrode after 10 min of CO$_2$ electrolysis at -0.81 V vs RHE (middle), and the active Cu catalyst after 40 hrs of CO$_2$ electrolysis at -0.81 V vs RHE (top) in CO$_2$-saturated 0.1 M KHCO$_3$ solution.

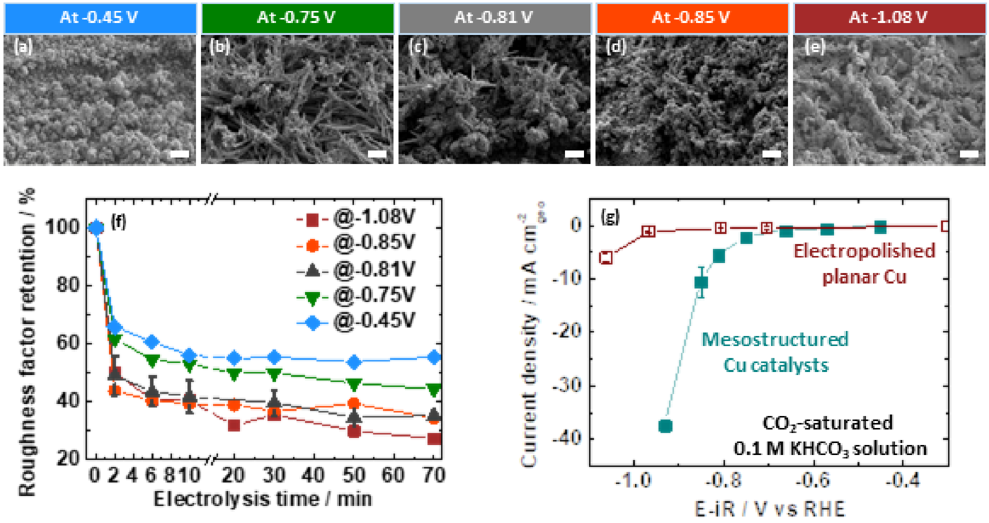

Figure 3.5. Structural and electrochemical properties of the *operando* catalysts. (A)-(E) SEM images of $Cu(OH)_2$ nanowire catalyst after 1 hr CO_2 electrolysis at the representative potentials. Scale bars 2 µm. (F) Roughness factor retention of the mesostructured Cu catalyst with respect to the electrolysis time and potential. (G) Average current density during 1 hr chronoamperometry for mesostructured Cu catalyst (green, filled squares) and electropolished planar Cu (red, open squares) as a function of potential.

3.5 Shifting Selectivity toward Multi-carbon Products

The morphology of the catalysts after 1 hr of CO_2 electrolysis is shown in Figure 3.5A-E, as a function of the CO_2 electrolysis potential. Nanoparticles and nanorods form within the remnants of the original nanowire frameworks, leading to the formation of a complex structure that varies with potential and a corresponding 2–3× decrease in surface area relative to the $Cu(OH)_2$ nanowires as quantified by electrochemical double layer capacitance (Table 3.1).

Measuring the change in the roughness factor relative to Cu foil as a function of time during CO_2 electrolysis clarifies the dynamics of the operando reduction of $Cu(OH)_2$ nanowires. As shown by the relative retention of the original roughness factor vs. time in Figure 3.5F for each potential tested in this work, the roughness factor is reduced in all cases by 40–60% during the first 10 min of electrolysis, consistent with the reduction of the $Cu(OH)_2$ nanowires verified by XRD and EIS (Figure 3.4C-D and 3.6). EIS is carried out with frequencies ranging from 100 mHz to 200 kHz at 0 V vs open circuit voltage (OCV) in CO_2-saturated 0.1 M $KHCO_3$ electrolyte.

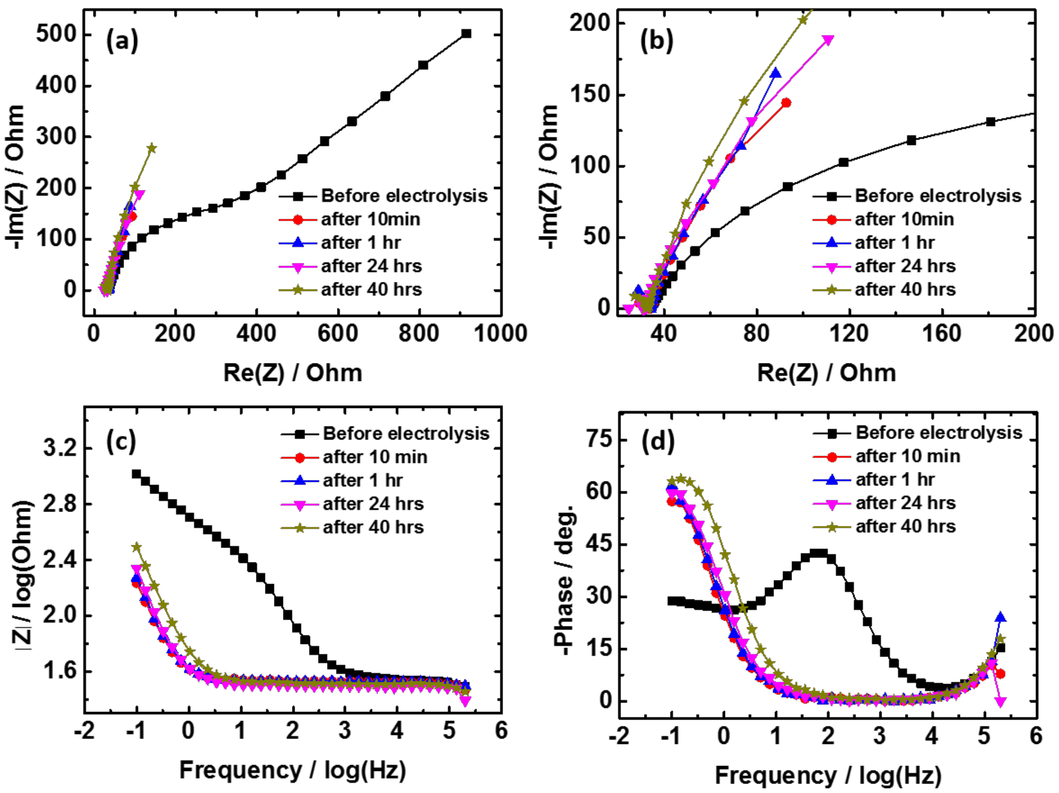

Figure 3.6. EIS of the $Cu(OH)_2$ nanowire precursors and the formation of the active catalysts as a function of electrolysis time measured at -0.81 V vs RHE. (a) Nyquist plots. (b) Nyquistplots at higher magnification near the origin. (c) Impedance magnitude vs. frequency. (d) Phase angle vs frequency.

In the resulting Nyquist plot (Figure 3.6a-b), a higher interfacial resistance for charge-transfer (R_{ct})[114] appears for the pristine catalyst compared to all mesostructured Cu catalysts. Figure 3.6c shows that the impedance after any electrolysis is lower than that of pristine catalyst over the whole frequency range, suggesting the improved surface conductivity as compared to the pristine catalyst. Figure 3.6d shows that the phase angle of the catalysts after electrolysis is higher than that of the pristine catalyst, resulting from lower R_{ct} for the mesostructured Cu catalyst than the pristine catalyst.[**?**] The pristine catalyst shows an additional phase feature at intermediate frequency that is a common property of the oxidized surface, indicating the reduced surface of all mesostructured Cu catalysts that consist of Cu^0[115, 116]

After 10 min of electrolysis, the roughness factor stabilizes for the duration of the 1 hr of CO_2 electrolysis, except for the catalyst measured at –1.08V vs RHE where a slight but consistent continued reduction in surface area is seen. Collectively, these results indicate not only that the $Cu(OH)_2$ nanowires on Cu foil substrates are completely reduced during the first minutes of CO_2 electrolysis ($\leq$ 10 min), but also that the CO_2 electrocatalysis measurements reported below take place on the modified morphology of the reduced catalyst. Based on these observations, the operando catalysts are hereafter denoted as mesostructured Cu catalysts.

Comparison of chronoamperometry (CA) of the *operando* mesostructured Cu catalysts with electropolished planar Cu reveals a clear change in the electrochemical properties (Figure 3.5G). The average current density during 1 hour of CA of the mesostructured Cu catalyst shows a clear turn on of catalytic activity and Tafel–like dependence with shifted onset potential (130 mV) as compared to the planar Cu. The geometric current densities of the mesostructured Cu catalyst and electropolished planar Cu foils show a stable current density during 1 hr of CO_2 electrolysis (Figure 3.7), indicating no deactivation from contamination or poisoning of either the higher-surface area mesostructured catalysts or the planar Cu.

The FE of the mesostructured Cu catalyst as a function of potential is shown in Figure 3.8A, calculated from steady state current density during CA and chemical analysis of the reaction products to establish partial current density for each product, as shown in Figure 3.8B

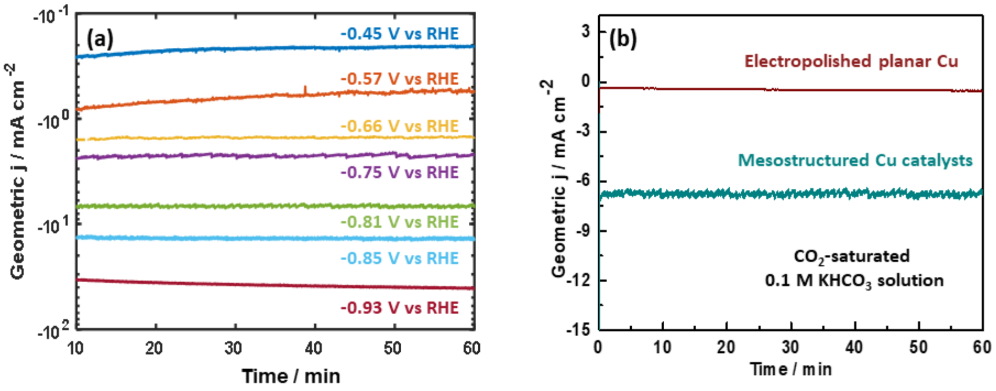

Figure 3.7. Geometric current densities as function of electrolysis time during chronoamperometric measurements for CO_2 reduction. (a) on the mesostructured Cu catalyst with respect to the potential measured. (b) on electropolished planar Cu and mesostructured Cu catalyst at -0.81 V vs RHE

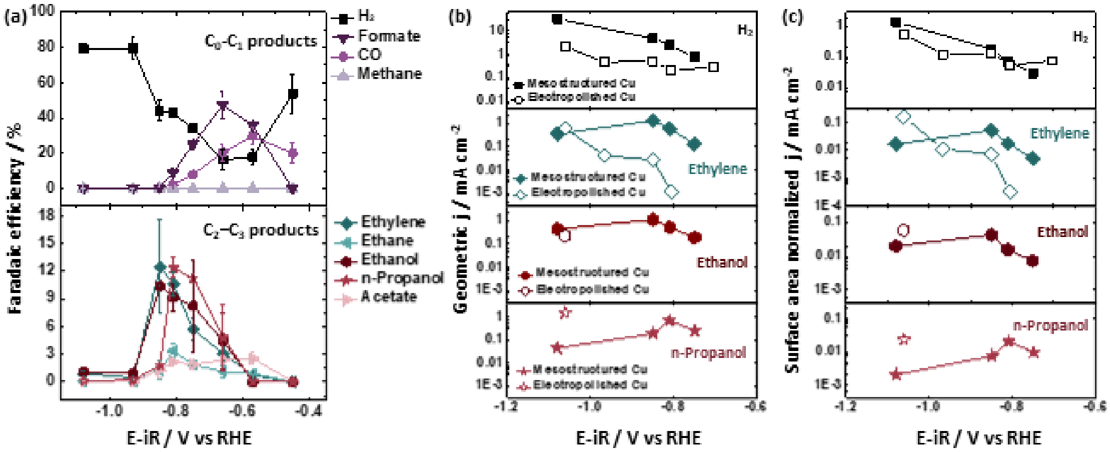

Figure 3.8. Catalytic activity of the mesostructured Cu catalyst. (A) Faradaic efficiencies of each CO_2 reduction product on the mesostructured Cu catalyst as a function of potential. (B) Geometric partial current density and (C) surface area normalized partial current density of mesostructured Cu and electropolished Cu.

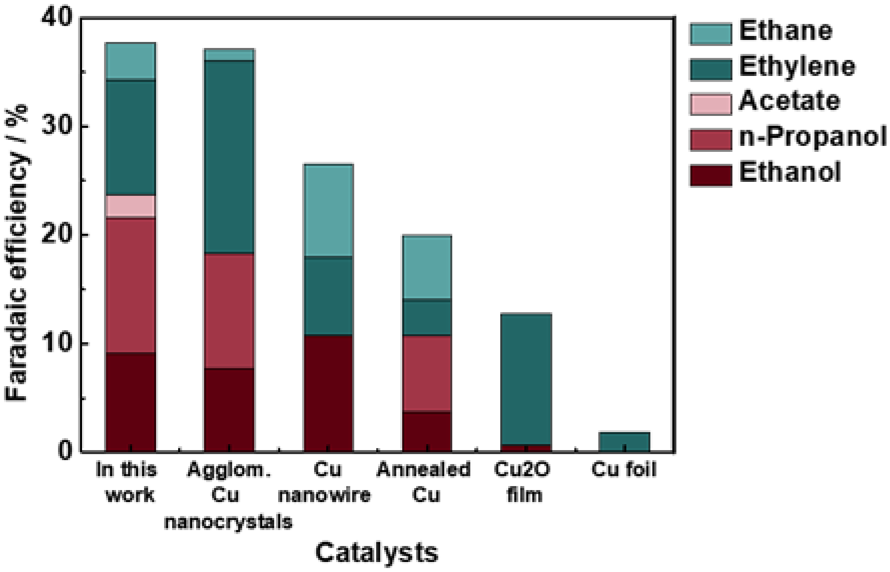

Figure 3.9. Comparison of mesostructured Cu catalysts FE for C_2-C_3 compounds with state-of-the-art Cu-based catalysts. Catalysts compared in this figure: Agglomerated Cu nanocrystals,[105] Cu nanowire,[23] Annealed Cu,[101] Electrodeposited Cu_2O film,[21] Cu foil.[4]

and Figure S4 in Kim et al.[5]. Results are detailed in Table 3.2. In the low overpotential range ($\leq$ -0.75 V vs RHE), CO and formate are predominantly observed, except for a small amount of acetate formation ($\leq 3\%$). To the best of our knowledge, the FE of acetate is reported herein for the first time at such low potential ($\leq$ -0.7 V vs RHE). At the lowest overpotentials only H_2 and CO are produced, due to insufficient overpotential for C-C bond formation. H_2 gas production prevails at the most negative potentials ($\geq$ -0.93 V vs RHE) from the competing hydrogen evolution reaction, suggesting that proton-coupled electron transfer is predominant at such negative potentials.[4, 102, 117] The trend in increased hydrogen evolution at the most negative potentials is consistent with other Cu catalysts active for CO_2 reduction.[4, 101, 105, 23] In general, a significant cause of this transition in the product distribution toward hydrogen are mass transport limitations at the high current densities at higher overpotentials (here for example, 40 mA cm^{-2} at -1.08 V vs RHE). The FE for CH_4 is minimal at all potentials.

The Cu catalysts show a dramatic change in product selectivity toward C_2 and alcohol products at moderate potentials from –0.85 to –0.66 V vs RHE. The maximum FEs for ethylene (12.5%), EtOH (10.4%), n-PrOH (12.4%) and ethane (3.4%) are achieved in this range of moderate overpotential, while CO and formate are suppressed (FE $\leq$ 1%). These maximum FEs for ethylene and EtOH are achieved at potentials similar to previous works.[4, 101, 103, 105, 23, 107] On the other hand, the onset of n-PrOH production and its peak FE are both approximately 100 mV more positive than previous reports for metallic catalysts, indicating enhanced electrocatalytic activity of the mesostructured Cu catalyst. The peak FE for n-PrOH surpasses 12% at -0.81 V vs RHE, also improved relative to the state-of-the-art. From –0.81 to –0.85 V vs RHE, the maximum partial current density for ethylene and ethanol exceeds 1 mA cm^{-2} and that for n-PrOH approaches 0.5 mA cm^{-2} (Figure 3.8B). Figure 3.9 shows a comparison of catalyst selectivity toward C_2-C_3 compounds at -0.81 V vs RHE for the mesostructured Cu catalyst and other state-of-the-art Cu based catalysts.[4, 101, 103, 105, 23] The mesostructured Cu catalyst achieves the highest FE for alcohols (21.5%) and n-PrOH specifically (12.4%). The sum of FEs for the selected C_2-C_3 compounds are 37.7%, 37.1%, 26.6%, 19.9%, 12.8%, and 1.8% for the mesostructured Cu catalyst, agglomerated Cu nanocrystals,[105] Cu nanowire,[23] annealed Cu,[101] electrodeposited Cu_2O film,[103] and Cu foil,[4] respectively. Moreover, by inspection of Figure 3.9, planar catalysts appear incapable of significant formation of n-propanol at this overpotential, while engineering the catalyst morphology appears to lead to an effective environment for forming alcohols.

By normalizing geometric partial current density by roughness factor to examine the surface-area normalized current density -– a better metric of catalyst activity, we find that the mesostructured Cu catalyst shows significantly improved activity toward C_2-C_3 compounds (especially, ethylene, EtOH, and n-PrOH) relative to planar Cu, while its activity toward forming C_1 products is suppressed (Figure 3.8C for major products and Figure S4b[5], minor products). The mesostructured Cu catalyst shows $\sim$56x increased surface-area normalized partial current density of ethylene as compared to planar Cu at -0.81 V vs RHE. Notably, the mesostructured

Cu catalyst shows unprecedented production of EtOH and n-PrOH at the moderate potential ($\leq$ -0.85 V vs RHE), where no alcohol formation occurs on planar Cu. The mesostructured Cu catalyst exhibits maximum surface area normalized partial current densities of EtOH and n-PrOH at $\sim$250 mV more positive potential than those of planar Cu. The enhanced FE of the mesostructured Cu catalyst toward desirable C_2-C_3 compounds can be first accounted for by low H_2 evolution activity in the range of moderate overpotential ($\leq$ -0.85 V vs RHE), as shown in Figure 3.8C.[65] The surface area normalized partial current density of H_2 on the mesostructured Cu catalyst appears to be lower in the moderate potential range ($\leq$ -0.85 V vs RHE) than that of on the electropolished planar Cu electrode. This would suggest that the parasitic H_2 evolution reaction is suppressed on the mesostructured Cu catalyst at moderate overpotentials.

While the local nanostructure is a key component of the shift in selectivity, analyzing roughness factor of various Cu catalysts[4, 101, 103, 105] against their FEs for C_2-C_3 compounds (Table 3.1) illustrates that surface roughness does not account wholly for the improvement of the mesostructured Cu catalyst. An oxide-derived annealed Cu catalyst[101] with a roughness factor of 475 shows an FE for C_2-C_3 compounds of 20%, while a FE of 37% for C_2-C_3 compounds is found on agglomerated Cu nanocrystals[105] with a roughness factor of only 24. The mesostructured Cu catalyst produced in situ at -0.81 V vs RHE has a roughness factor of 37.3, but an FE for C_2-C_3 compounds of $\geq$ 37.7%. Little trend of C_2-C_3 selectivity with roughness factor is evident.

Comparing Tafel slopes of the mesostructured Cu catalysts against previously-reported Cu-based catalysts indicates that the rate determining step may be similar to other nanostructured catalysts (Figure 3.10). The Tafel plot shows that the mesostructured Cu catalysts have a lower Tafel slope (266 mV dec^{-1}) than Cu foil[4] (492 mV dec^{-1}), but a slope similar to agglomerated Cu nanocrystals[105] (270 mV dec^{-1}) in the potential range of high C_2-C_3 production (-0.7 to -0.9 V vs RHE). Although difficult to interpret for complex multi-step reactions such as CO_2 reduction, the Tafel analysis highlights the significance of the structure produced by in situ reduction to Cu^0 on reaction kinetics.[105]

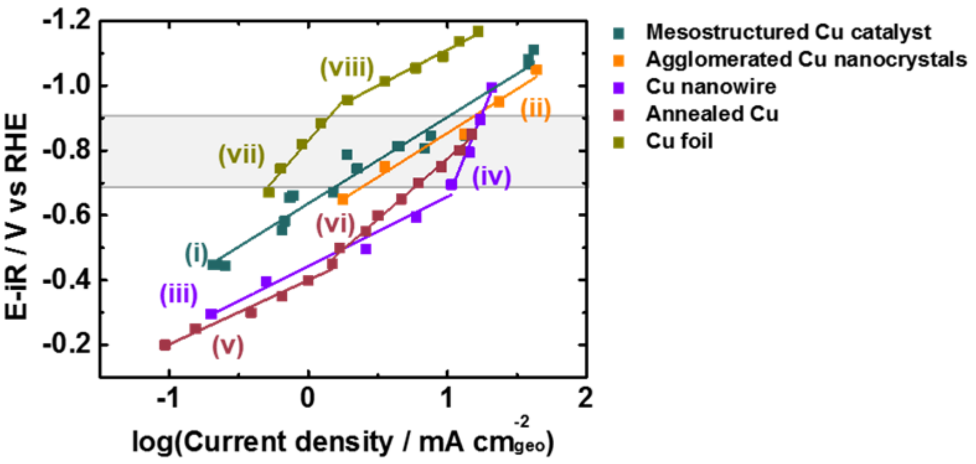

(i) Mesostructured Cu catalyst: 266 mV dec^{-1} ($R^2 = 0.96$)

(ii) Agglomerated Cu nanocrystals : 270 mV dec^{-1} ($R^2 = 0.97$)

(iii) Cu nanowire : 190 mV dec^{-1} ($R^2 = 0.96$)

(iv) Cu nanowire : 1047 mV dec^{-1} ($R^2 = 0.97$)

(v) Annealed Cu : 197 mV dec^{-1} ($R^2 = 0.97$)

(vi) Annealed Cu : 373 mV dec^{-1} ($R^2 = 0.99$)

(vii) Cu foil : 492 mV dec^{-1} ($R^2 = 0.97$)

(viii) Cu foil : 221 mV dec^{-1} ($R^2 = 0.99$)

Figure 3.10. Comparison of Tafel slope with Cu-based CO_2 reduction catalysts of various morphologies. Catalysts compared in this figure: Agglomerated Cu nanocrystals,[105] Cu nanowire,[23] Annealed Cu,[101] and Cu foil.[4] The intermediate overpotential region where significant C_2-C_3 production is seen is highlighted in gray.

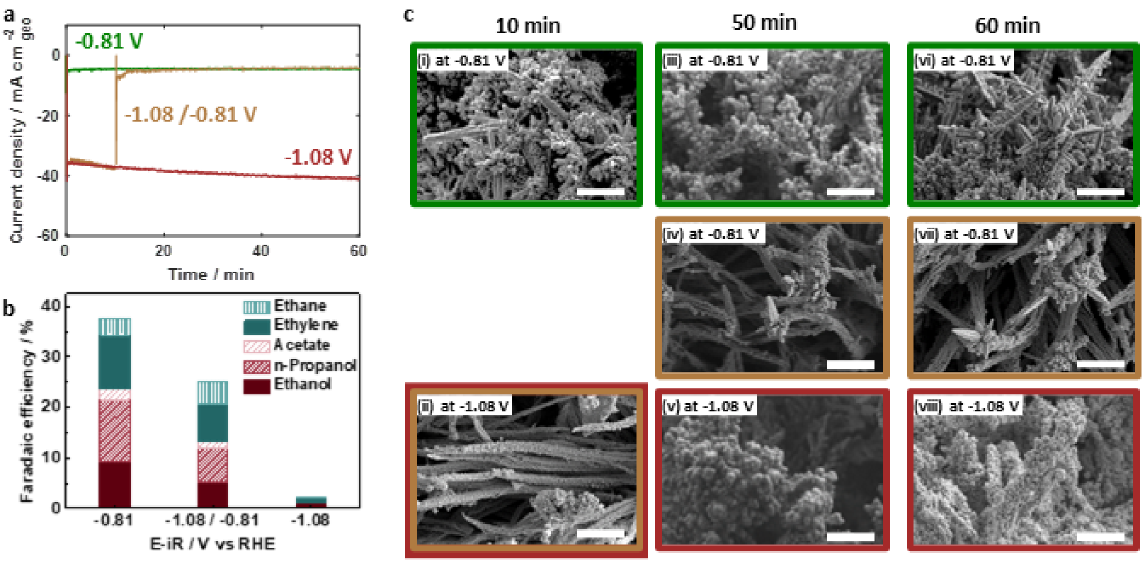

Figure 3.11. Investigation of the effect of catalyst morphology on selectivity for CO_2 reduction products. (A) Geometric current density vs. time for catalysts held at -0.81 V for 1 hr (green), -1.08 V for 10 min and -0.81 V for 50 min (yellow), and -1.08 V for 1 hr (red). (B) FE of C_2-C_3 compounds with respect to the applied potential during catalyst formation and during electrolysis. (left) Catalyst formation and bulk CO_2 electrolysis at -0.81 V vs RHE. (center) Catalyst formation at -1.08 V vs RHE and bulk CO_2 electrolysis at -0.81 V vs RHE. (right) Catalyst formation and bulk CO_2 electrolysis at -1.08 V vs RHE. (C) SEM images of the catalysts after electrolysis for: (i) 10 min at -0.81 V vs RHE, (ii) 10 min at -1.08 V vs RHE, (iii) 50 min at -0.81 V vs RHE, (iv) 10 min at -1.08 V vs RHE and 40 min at -0.81 V vs RHE (v) 50 min at -1.08 V vs RHE, (vi) 60 min at -0.81 V vs RHE (vii) 10 min at -1.08 V vs RHE and 50 min at -0.81 V vs RHE, and (viii) 60 min at -1.08 V vs RHE. Scale bar 1 μm for all images.

The improved FE of the mesostructured Cu catalyst toward C_2-C_3 production at intermediate potentials may be attributable to the particular mesostructure morphology that develops *operando*. We observed that a hierarchical structure only appears on the catalysts that experienced moderate potentials -0.75, -0.81, and -0.85 V vs RHE (Figure 3.5B-D), and these potentials are those where the formation of C_2-C_3 compounds is favored. In contrast, the catalysts exposed lower and higher overpotentials (-0.45 and -1.08 V vs RHE) show only agglomerated nanoparticles on the surface (Figure 3.5A and E). The dominant formation of gases (H_2 and CO) at low or high overpotential may collapse developing mesostructure, leading to relatively featureless nanoparticulate surfaces outside the mid-overpotential range that will be discussed in detail below.

To test the hypothesis that the hierarchical mesostructured morphology that is produced in situ at a moderate overpotential is responsible for enhanced C_2-C_3 production, we reduced $Cu(OH)_2$ nanowires at higher potential (-1.08 V vs RHE) for 10 min to produce a more wire-like geometry and then tested the selectivity during CO_2 electrolysis at the optimal potential of -0.81 V vs RHE. Figure 3.11A and B shows a comparison of the FE for C_2-C_3 compounds for three cases: (1) a mesostructured Cu catalyst formed and tested at -0.81 V vs RHE for 1 hr (2) a Cu catalyst held at -1.08 V vs RHE for 10 minutes and then tested during extended CO_2 reduction electrolysis for 50 min at -0.81 V vs RHE, and (3) a Cu catalyst formed and tested at -1.08 V vs RHE for 1 hr.

The morphology of the catalyst held at -0.81 V vs RHE retains a complex nanoparticle/nanorod surface in a mesostructured morphology throughout (Figure 3.11 top row, i, iii, and vi). On the other hand, it is clear that the surface morphology at -1.08 V vs RHE does not retain its structure during 1 hr of electrolysis (Figure 3.11 bottom row, ii, v, and viii). The initial wire-like morphology collapses during the time period of 10-50 min of electrolysis into an agglomerated nanoparticle structure, with continued minor evolution of the structure until the end of testing at 60 min. This collapse of mesostructured is consistent with the low surface roughness seen in Figure 3.5F. This structural collapse may be due to the significant H_2 gas generation on the electrode surface at -1.08 V vs RHE (Figure 3.8A), resulting in an agglomerated nanoparticulate morphology. The catalyst formed at -1.08 V vs RHE but held at -0.81 V vs RHE for extended CO_2 electrolysis largely retains the initial wire-like structure during bulk extended electrolysis at -0.81 V vs RHE (Figure 3.11 ii, iv, and vii). By the end of electrolysis, it shows a somewhat intermediate structure between those held the entire time at -0.81 V and -1.08 V vs RHE (cf. Figure 3.11 (vi) and 3 (viii)), suggesting that the surface morphology may evolve slightly during CO_2 reduction at -0.81 V vs RHE perhaps due to product evolution from the surface.

We find that the sum of FE for C_2-C_3 products at -0.81 V vs RHE for the catalyst with the complex nanoparticle/nanorod morphology (Figure 3.11vi) is $\sim$150% of that for the catalyst with the wire-like morphology (Figure 3.11vii) operating at the same CO_2 electrolysis potential.

Because a large fraction of the current during the first minutes of electrolysis ($\leq$ 10 min) is consumed to reduce the $Cu(OH)_2$ electrode surface and form the *operando* mesostructured catalyst, these differences in product distribution arise predominantly from the different selectivity of these catalysts during extended electrolysis at –0.81 V vs RHE. The enhanced C_2–C_3 production from the catalyst formed at –0.81 V vs RHE can therefore likely be attributed to the particular hierarchical morphology of this catalyst. The production of C_2–C_3 compounds with the catalyst formed at –1.08 V vs RHE and tested at –0.81 V vs RHE is still an order of magnitude higher than that of on the catalyst formed and tested at –1.08 V vs RHE ($\sim$2%), indicating that the CO_2 electrolysis potential is of course still a strong determinant in product selectivity toward C_2-C_3 compounds.

These findings demonstrate that the enhanced selectivity of CO_2 reduction to C_2–C_3 compounds and especially alcohols at moderate overpotentials using a mesostructured Cu catalyst can be attributed to the formation of a favorable, potential-dependent morphology. This structure may lead to an increased local pH, which has been found previously to favor the formation of C_2–C_3 compounds,[86, 97, 105, 106] and increased local concentrations of reaction intermediates near the surface. In parallel, the volume change during the in situ reduction from $Cu(OH)_2$ to produce the catalyst may induce significant surface strains and generate active defect sites.[105] Further study is needed to fully attribute the mechanisms underlying the enhanced C_2-C_3 formation seen here to atomic-scale effects on the catalyst surface or mesoscale chemical reaction kinetics of the intermediates and products within the complex 3D structure of the catalyst.

The mesostructured Cu catalyst is robust against degradation during extended bulk CO_2 electrolysis at -0.81 V vs RHE, as shown in Figure 3.12. The current density maintains a steady value of $\sim$ -4.4 mA cm^{-2} throughout the duration of the test. The FEs of CO_2 reduction gas products exhibit a 1% decrease (Figure 3.12A), while that of H_2 fluctuates around 40%, indicating steady electrocatalytic activity favoring CO_2 rather than H_2O reduction. The FE for n-PrOH remains remarkably stable, retaining $\geq$ 98% of its original value over 24 hrs, $\geq$ 94% over 40 hrs,

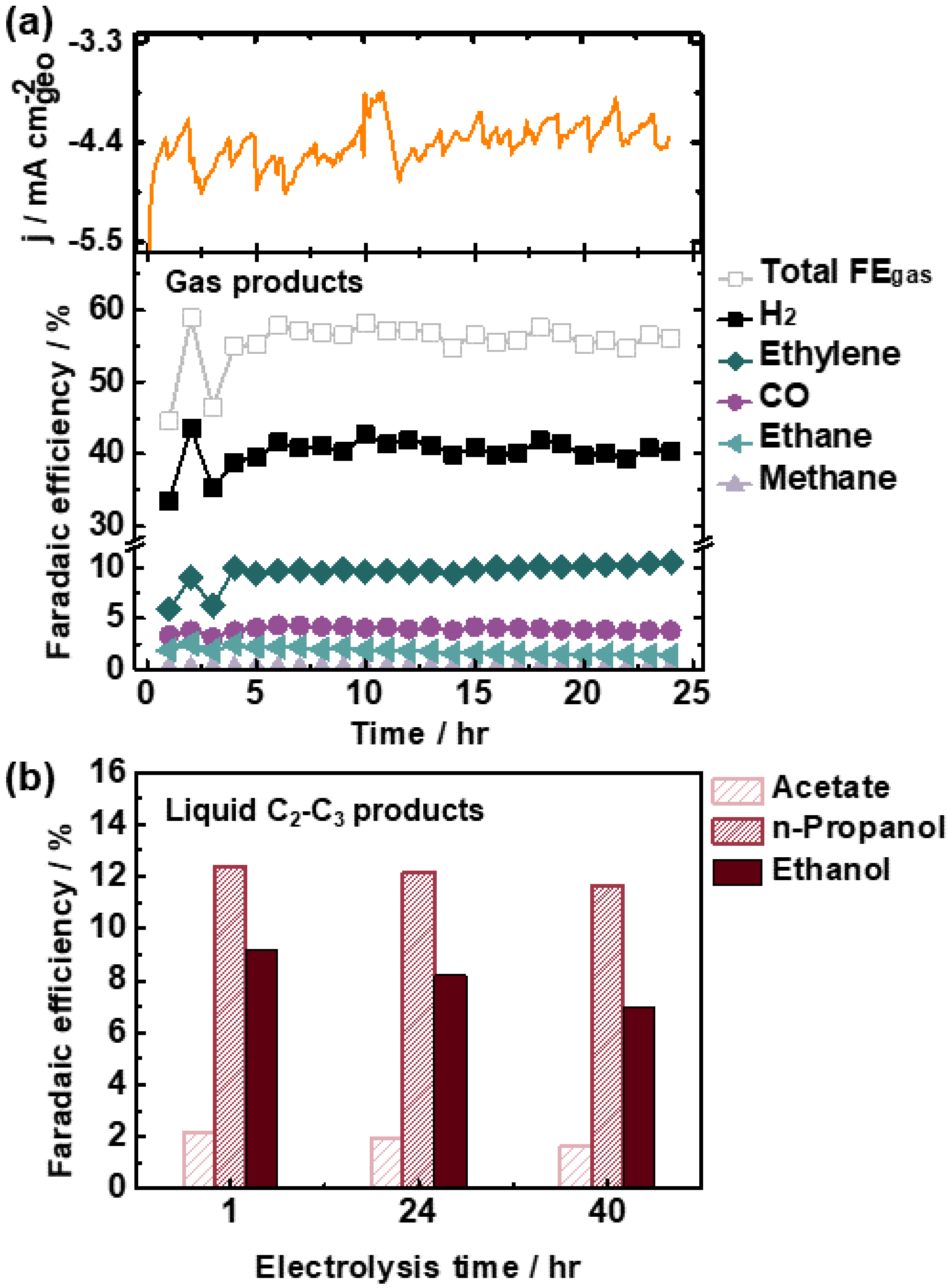

Figure 3.12. Long-term CO_2 electrolysis using the mesostructured Cu catalyst. (A) Total current density and Faradaic efficiencies of gas products for 24 hrs. (B) Faradaic efficiency of liquid C_2-C_3 compounds with respect to CO_2 electrolysis time.

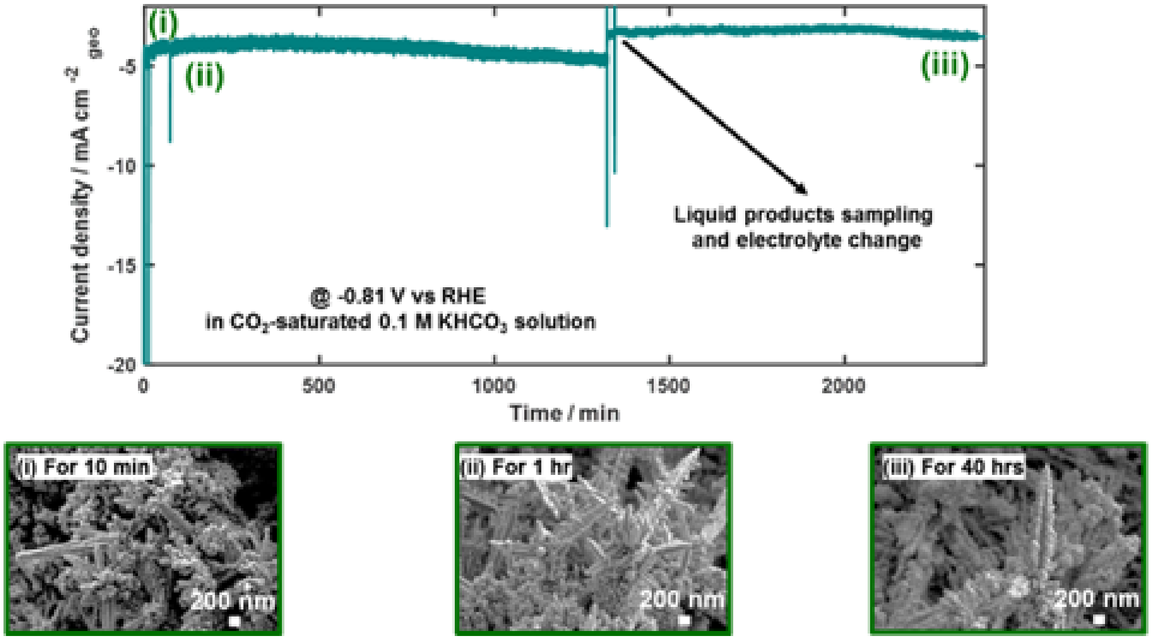

Figure 3.13. SEM images of the *operando* Cu catalyst after increasing electrolysis time (i) 10 min, (ii) 1 hr, and (iii) 40 hrs.

as shown in Figure 3.12B. The FE of EtOH and acetate also remain relatively stable throughout the CO_2 electrolysis. The low propensity toward methane generation (Figure 3.12A) may limit poisoning of the nanostructured catalysts by the intermediates in CH_4 production.[105, 108, 118] The decrease in the FE of these liquid products cannot be attributed solely to the activity of the electrode itself, as membrane crossover and subsequent oxidation during the long CO_2 electrolysis may occur. The counter electrode compartment contents are included in the NMR analysis and routinely indicate liquid products (e.g. formate and acetate) have crossed over. In general, the degree of purity in the electrolyte can affect the deactivation of catalyst for CO_2 reduction.[119, 27] The mesostructured Cu catalysts appear robust to such effects. We further note that the morphological alteration of the catalyst itself (Figure 3.5B-D) does not reflect an ongoing degradation of the electrode, but represents a systemic change that appears after 10 min of CO_2 electrolysis. The catalyst retains its physical structure over 40 hrs of CO_2 electrolysis, as shown in Figure 3.13.

3.6 Summary

The electrocatalytic activity and selectivity for CO_2 reduction of *operando* Cu catalysts prepared from $Cu(OH)_2$ nanowires are strongly governed by a potential-dependent mesostructure. Tuning the morphology produces catalysts with Faradaic yields for C_2–C_3 compounds, and especially alcohols, that are enhanced at lower overpotentials relative to state-of-the-art catalysts. Total FE for C_2–C_3 products reaches 38% at moderate potentials (–0.81 V RHE). The mesostructured Cu catalyst shifts selectivity from C_0–C_1 to C_2–C_3 products relative to planar Cu electrodes after formation of a hierarchical nanorod/nanoparticule morphology that creates an effective reaction environment for forming C_2–C_3 compounds. Furthermore, the mesostructured Cu catalysts maintained activity and selectivity for 40 hrs of CO_2 electrolysis, indicating stable catalysis. These findings highlight the potential opportunity to use multiple length scales in catalyst design from the immediate interactions at the surface atomic scale to the mesoscale morphology to construct active and selective electrocatalysts for difficult multi-electron reactions such as CO_2 reduction.

3.7 Acknowledgement

Chapter 3, in full, is a reprint of the material ”Enhancing C_2–C_3 Production from CO_2 on Copper Electrocatalysts via a Potential-Dependent Mesostructure” as it appears in ACS Applied Energy Materials, Taewoo Kim, Alireza Kargar, Yanqi Luo, Ragad Mohammed, Erick Martinez-Loran, Aditi Ganapathi, Priyasha Shah, and David P. Fenning, 2018, 1 (5), 1965. The dissertation author was the primary investigator and author of this material.

Chapter 4

Shifting Chemical State of Sn and Tuning CO_2 Mass Transport to Enhance CO_2-to-formate Conversion

4.1 Introduction

Electrochemical CO_2 transformation is an attractive way to meet carbon neutrality and introduce a new route to supply valuable carbonaceous chemicals. With emerging penetration of intermittent renewable energy into the grid, electrochemical recycling of waste CO_2 can also offer larger–scale storage of renewable electricity in chemical bonds.[120, 121] Among possible value-added electrochemical CO_2 conversion products, formate is of particular interest to meet net negative carbon emissions[10] since electrochemical synthesis of formate requires less energy than producing multi-carbon products. Integrating the e-synthesized formate into formic acid fuel cells enables the formate to be an alternative energy-dense carrier.[122]

Sn is one of the attractive transition metals for electrochemical CO_2-to-formate conversion. Sn has an optimal binding energy of *OCHO rather than *COOH among transition metals,[24] which suppresses the reaction path toward CO, hydrocarbon or alcohols. Also, its low cost can take advantages of larger–scale application.[123] Comparing the overall activity of CO_2-to-formate, oxide-derived Sn catalysts shows improved Faradaic efficiency and geometric current density of formate relative to metallic Sn catalyst.[25] It is also reported that the catalyst surface where SnO and SnO_2 are co-existing shows improved Faradaic efficiency as compared to the surface where only SnO_2 or metallic Sn is present.[26] Despite of those efforts to unravel fundamental insights on the catalytic material, the industrially feasible electrochemical CO_2-to-formate system is yet-to-be-developed due to lack of integration of fundamental understanding on materials and electrolysis system. A bottleneck of bridging the knowledge gap is originated from the mass transport limitation of CO_2 into the catalytic sites in the conventional electrolysis system.

For decades, many efforts have been made to understand the reaction mechanisms in a batch-type electrochemical reactor, relying on solubilized CO_2 in an aqueous electrolyte.[11] Larger-scale operations that requires high current density are limited due to the low solubility of CO_2.[124] To overcome the solubility issue, utilizing the gas diffusion layer (GDL) should be highlighted as it facilitates the direct feed of gaseous CO_2 to the electrode surface where the catalyst layer and an electrolyte interfaces.[59, 58] A challenge is remained as including electrolyte in the cathode chamber inevitably dilutes the liquid-phase products, which causes a necessity for the separation process. To date, membrane electrode assembly (MEA) type electrolyzer where cathode and membrane contacts without a catholyte has been considered as a promising alternative although more experimental perspectives are necessary to understand engineering parameters for larger-scale device performance.[125, 126, 127, 128] Also, investigation of the effect of partially concentrated CO_2 stream on the overall catalytic activity is necessary as the flue gas contains less than 15% of CO_2 in general.[129]

In this work, we report a strategy to promote electrochemical conversion of CO_2 to formate in a catholyte-free electrolyzer via modulating chemical state of the Sn oxides layer and controlling mass transport of the CO_2 stream. Post-heat treatment shifts the initial oxidation state of the thermally evaporated Sn oxide layer from co-existing of SnO and SnO_2 to SnO_2-rich environment, which is consistent with our previous work.[130] We find a promoted Faradaic efficiency toward formate on the Sn oxide layer ($\sim$83%) where SnO and SnO_2 were co-existed as compared to the SnO_2-rich layer (FE $\sim$74%). The calculated energy efficiency also appears to be improved up to 36% at -3.0 V of cell voltage when SnO is present at the beginning of the CO_2 electrolysis. With partially concentrated CO_2 stream, to explore flue gas composition, the energy efficiency and geometric partial current density of formate is linearly decreased along with decreasing CO_2 concentration. We find that increasing flow rate of CO_2 stream can overcome the lower CO_2 availability and improve reaction kinetics as it facilitates rapid CO_2 feed onto the catalytic sites. This work demonstrates that the energy efficiency and activity of electrochemical CO_2 reduction to formate on Sn oxide layer can be promoted by modulating the initial oxidation states and flow rate of CO_2 stream even at low CO_2 concentration.

4.2 Experimental Procedures

Electrode preparation To prepare Sn oxides electrodes, SnO_2 nanoparticles (99.7% purity, 35-55 nm, US Research Nanomaterials) are placed in an alumina-coated tungsten boat in a high vacuum ($< 7\text{x}10^{-7}$ mTorr) chamber for thermal evaporation at a rate of 0.14-0.2 Å s^{-1} onto GDLs. GDLs are purchased from Fuelcellstore (AvCarb GDS2230) and cut into 1 cm^2 sized pieces. The cut GDLs are used with no further pre-treatment. The thickness of the Sn oxides layers is monitored via quartz crystal microbalance (QCM). For the post-heat treated electrodes, the as-prepared electrodes are annealed at 300 ^{o}C for 5 hrs in the muffle furnace. The surface morphologies of the as-prepared electrodes are characterized by scanning electron microscopy (SEM, Zeiss, Sigma 500). Surface valence band and core-level electronic structure of the as-prepared electrode are characterized by X-ray photoelectron spectroscopy (XPS) with a 90° emission angle with respect to electrode surface (Kratos, AXIS Supra) Al Kα radiations at vacuum levels below 5×10^{-8} Torr. The XPS spectra are recorded using pass energies of 160 eV for the XPS survey and 20 eV for the narrow scans. The binding energies are calibrated using both Fermi edge (0.06 eV) and the Au 4f7/2 second-order peak (84 eV). The Ir oxides anode is prepared via modified thermal pyrolysis.[131, 132] Surface-etched Ti meshes (Fuelcellstore) are used as substrates. The meshes are cut into 1 cm^2 sized pieces that are sonicated in a mixture of acetone/IPA/DI water (6:3:1 v/v), followed by DI water for 10 min each. The cleaned substrates are etched in 20 vol.% of HCl solution for 5 min and then transferred to 10 wt.% boiling oxalic acid solution for 10 min prior to final cleaning with DI water in a bath sonication. A precursor solution is prepared by dissolving 26 mg of Iridium (III) chloride hydrate (99.9% purity, Sigma Aldrich) in a mixture of 6.71 ml IPA and 2 ml of concentrated HCl solution. The precursor solution is subsequently dropped onto surface-etched Ti meshes that are pre-heated to 125 ^{o}C until the total loading of 1.0 mg cm^{-2} is achieved. The electrodes are finally annealed at 500 ^{o}C for 3 hrs in a muffle furnace. The contact angles of H_2O are measured using a Goniometer (rame-hart^{TM} Model 200). The crystalline structure of the Sn oxide electrodes are characterized by X-ray diffractometry (XRD, Rigaku, Smartlab) with parallel beam configuration.

Electrolyzer configuration A customized catholyte-free electrolyzer (Fuel Cell Technologies, Inc) with an active area of 1 cm^2 is used for all CO_2 electrolysis. The interdigitated flow channels are applied to both graphite and Ti current collectors (for cathode and anode, respectively). A Nafion 117 is used as a membrane to transport protons from the anode chamber to the cathode surface. Ir oxides on Ti mesh electrodes are used as anode. Prior to CO_2 electrolysis, the membrane is rinsed and sonicated with DI water, and then immersed in the anolyte solution for at least overnight. PTFE sheets (0.01 inch) were used as gaskets. The electrolzyer is compressed with 8 hex screws sequentially torqued (8-10-12 N m) with an electronic torque wrench.

Carbon Dioxide electrolysis The electrochemical analysis is performed in the two-electrode system using a potentiostat (VSP-300, biologic). Prepared cathodes, the Nafion membrane, and Ir oxides anode are positioned and sandwiched together via current collectors with PTFE gaskets. 40 ml of 0.5 M sodium phosphate buffer (98% purity, Fisher scientific) solution (pH 3) is circulated using a peristaltic pump through the backside of the Ti flow channels on the anode side. Research-grade CO_2 gas is supplied to the backside of the graphite flow channels on the cathode side through a home-made bubbler setup at the rate of 200 ml min^{-1} unless otherwise mentioned. The flow rate is controlled by a mass flow controller (Smart

Track 100, Sierra). The partially concentrated CO_2 stream (3 and 15% of CO_2) is formulated via balanced with research-grade N_2 gas. At least three electrolysis are carried out at each experimental condition for repeatability.

Online quantification for gas products is started after 20 min of initial electrolysis to account stabilization of the cathode. All gas products produced from the cathode are collected directly into a gas-sampling loop and quantified by gas chromatography (GC, SRI 8610C, SRI) with a molecular sieve of 5A and a Haysep D column, a TCD/FID detector equipped with a methanizer, and using Ar as a carrier gas. The partial current density of each gas product is averaged over 4 GC injections during 1 hr electrolysis with chronoamperometry. The liquid product is quantified at the end of each electrolysis using ^{1}H nuclear magnetic resonance (NMR) spectroscopy with a 500 MHz spectrometer (ECA500, JEOL). The water peak is suppressed via a presaturation sequence. Additional details can be found in our previous work.[126] Raman analysis is applied to identify salt after 1hr of CO_2 electrolysis. Raman spectra are taken on an inVia confocal Raman microscope (Renishaw) using a 633 nm excitation laser and 600 l/mm. Each spectrum is summed from 25 scans across a $2 \times 2 mm^2$ area with 2 seconds of exposure per scan.

4.3 Controlling Chemical States of Sn Oxide Electrodes

The chemical state of the 100 nm Sn oxide electrodes on GDL are controlled by post-heat treatment (at 300 ^oC for 5 hrs in air), and the corresponding oxidation states are determined via X-ray photoelectron spectroscopy (XPS). The O 1s core-level spectra in Figure 4.1A reveals that the as-prepared Sn oxide surface consists of co-existing SnO and SnO_2 while the annealed Sn oxide surface is SnO_2 predominant, which is consistence with our previous work.[130] Comparing the valance band maximum (VBM) spectra in Figure 4.1B further supports that SnO is present on the as-prepared Sn electrode and it disappears after heat treatment. To note, semiconducting metal oxide layers growing through thermal evaporation exhibit oxygen

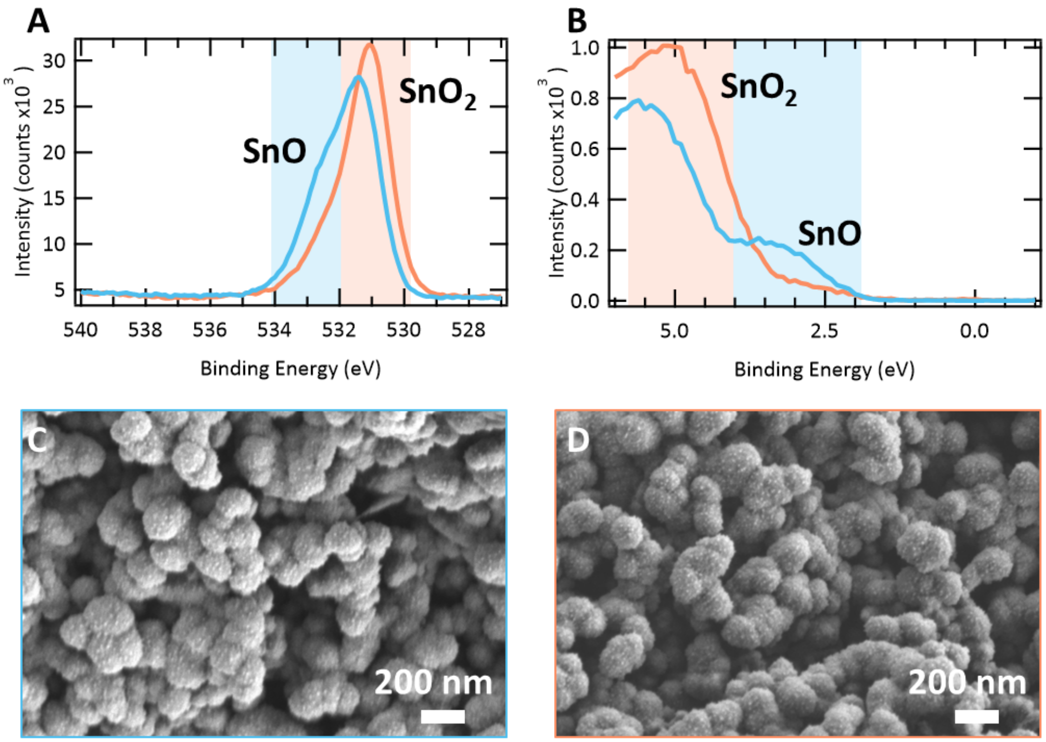

Figure 4.1. Structural properties of Sn oxide electrodes. X-ray photoelectron spectroscopy (XPS) of (A) O 1s core level and (B) valence band maximum (VBM) spectra. Scanning electron microscopy (SEM) images of (C) as-prepared and (D) annealed Sn oxide electrode.

deficiency in general.[133, 134]

Surface morphology is sustained regardless of heat treatment. The Sn oxide electrodes shows accumulated spherical particles with gaps between the features (Figure 4.1C–D), similar to the surface structure of the GDL (Figure 4.2). The annealing temperature is decided based on the contact angles of H_2O on the series of the annealed GDL surfaces to ensure no structural changes on the GDL during heat treatment (Figure 4.3).

No crystalline structure of the Sn oxides on GDL is detected from X-ray diffractometry (XRD) regardless of heat treatment as shown in Figure 4.4. This is due to the close proximity of the Bragg diffraction angles of graphite to SnO_2 (110), SnO (102), and SnO_2 (220), which results in a single Bragg diffraction for all samples that we are not able to confidently distinguished. On the basis of these observations, the as-prepared and the annealed Sn oxides electrodes are

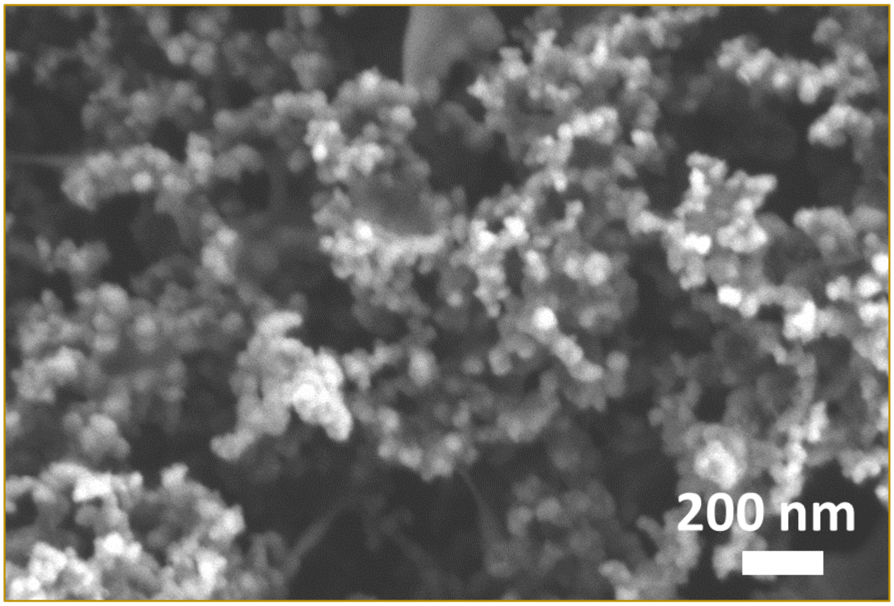

Figure 4.2. Scanning electron microscopy (SEM) image of bare gas diffusion layer (AvCarb GDS2230).

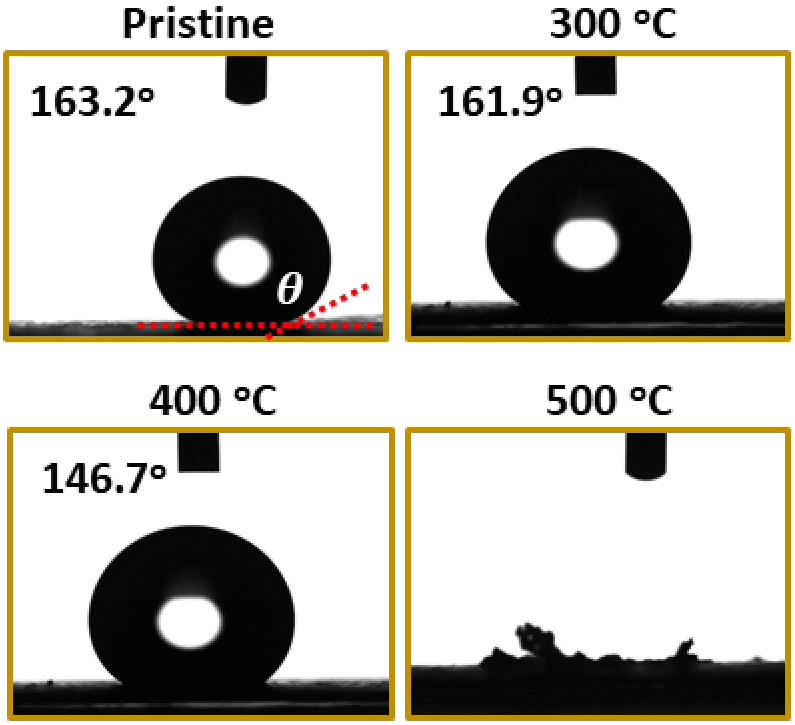

Figure 4.3. The contact angle of H_2O on the gas diffusion layers along with increasing annealing temperature. The contact angle on the GDLs annealed above 300 ^{o}C decreases or the surface is deformed during the measurement, indicating degradation of the structural property

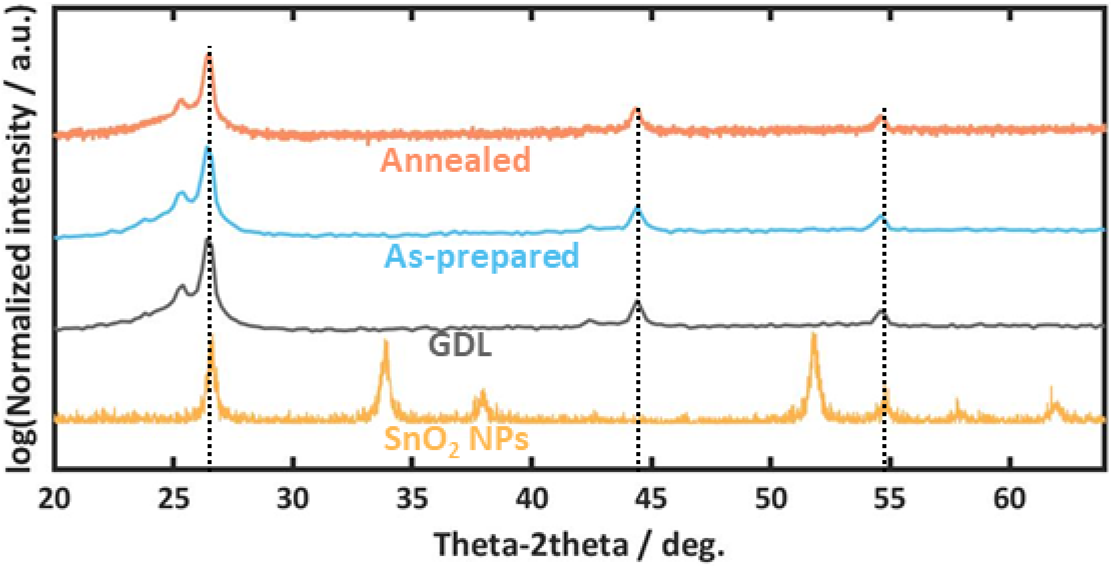

Figure 4.4. The crystalline structure of the Sn oxide electrodes, bare gas diffusion layer, and SnO_2 nanoparticles.

hereafter denoted as SnO-rich and SnO_2-rich catalysts, respectively.

4.4 Effect of the Chemical State of Sn Oxide Catalysts on the CO_2 Electrolysis

Shifting the oxidation state of Sn modulates the catalytic activities as shown in Figure 4.5. In the range of cell voltage from -3.0 to -3.4 V, formate appears to be the major CO_2 reduction products with marginal formation of CO and hydrogen on the Sn oxide catalysts (Figure 4.5A). The calculated geometric partial current density of formate on the SnO-rich catalyst increases with more negative cell voltage (from -3.0 to -3.4 V) up to 34.9 mA cm_{geo}^{-2}, while that of CO is rather consistent (< 1.6 mA cm_{geo}^{-2}). The SnO_2-rich catalyst shows similar activities for formate and CO, and slightly more activity of formate generation at -3.4 V of cell voltage (46.3 mA cm_{geo}^{-2}). Although the parasitic hydrogen evolution tends to increase along with more negative cell voltage and maximize at the most negative cell voltage (-3.4 V) on both Sn oxide catalysts, formate is still the predominant product. This indicates that: 1) the Sn oxide catalysts prepared in this work are active for CO_2-to-formate reaction and 2) kinetically facile hydrogen evolution may start competing CO_2 reduction reaction and perhaps the limited mass transport of CO_2 at high current density may promote hydrogen evolution at such high potential. Overall, shifting oxidation state of the Sn oxide catalysts does not show distinguishable changes in the geometric partial current densities.

However, the SnO-rich catalyst shows improved selectivity toward formate as compared to the SnO_2-rich catalyst, as shown in Figure 4.5B. The Faradaic efficiency of formate on SnO-rich catalysts appears to be 80.0$\sim$82.7% in the given cell voltages. An opposite trend of Faradaic efficiency of CO and hydrogen on the cell voltage is observed, and their maximum Faradaic efficiencies are 7.3% and 13.0% at -3.0 and -3.4 V of cell voltage, respectively. On the SnO_2-rich catalysts, Faradaic efficiency of formate is suppressed down to $\sim$74.0% in the given cell voltages. Similar to the SnO-rich catalyst, Faradaic efficiencies of CO and hydrogen are swapped, which suggests that CO and hydrogen formation on the Sn oxide catalysts are sensitive to the cell voltage while formate generation is rather governed by the oxidation state of Sn oxides. The observed Faradaic efficiency and geometric partial current density of formate on the SnO-rich catalyst is comparable with the state-of-the-art catalysts (Figure 4.6).[128, 135, 125] Corresponding energy efficiency of formate in Figure 4.5C shows that SnO-rich catalysts outcompete the SnO_2-rich catalyst over the range of cell voltage, with 36.0% of maximum energy efficiency at -3.0 V of cell voltage. This catalytic activity may offer a possible nearest-term path to carbon-negative CO_2 electrolysis with given grid intensity in California (0.2 $mTCO_2/MWh$).[9, 10]

Post-electrolysis XPS is performed to examine the changes in the chemical state of the Sn oxides after 1 hr of CO_2 electrolysis, as shown in Figure 4.7. The O 1s core-level spectra shows upshifted binding energy of O 1s on both Sn oxide catalysts after electrolysis, indicating that a portion of SnO_2 are reduced to SnO during CO_2 electrolysis (Figure 4.7A). Interestingly, the SnO_2-rich catalyst remains a distinctive shoulder peak which is corresponds to SnO_2 even

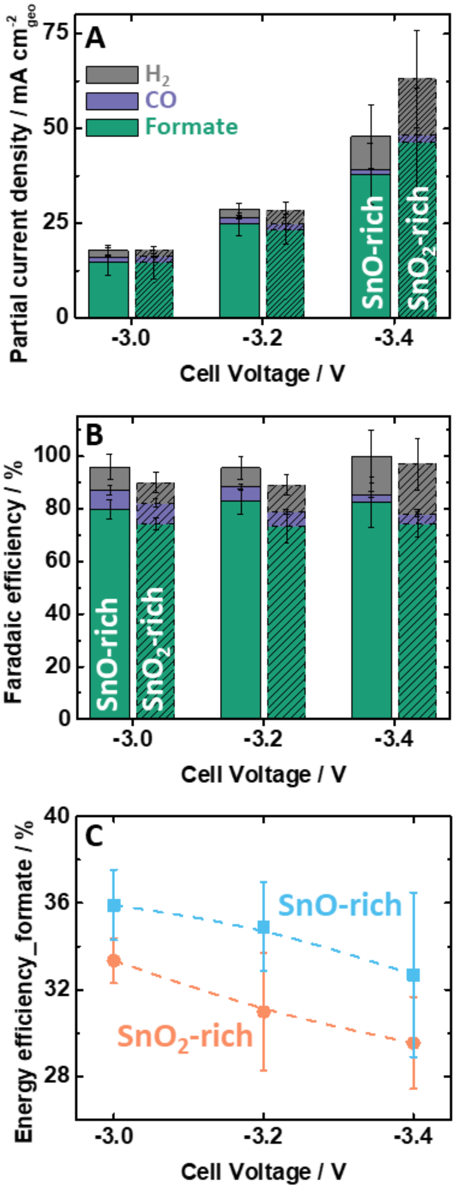

Figure 4.5. CO_2 reduction activities of SnO-rich and SnO_2-rich catalysts as a function of cell voltage. The filled box is for the SnO-rich and the dashed box is for the SnO_2-rich catalyst. (A) Geometric partial current densities and (B) Faradaic efficiencies of Hydrogen, CO, and formate. (C) Energy efficiency of formate on the SnO-/SnO_2-rich catalysts.

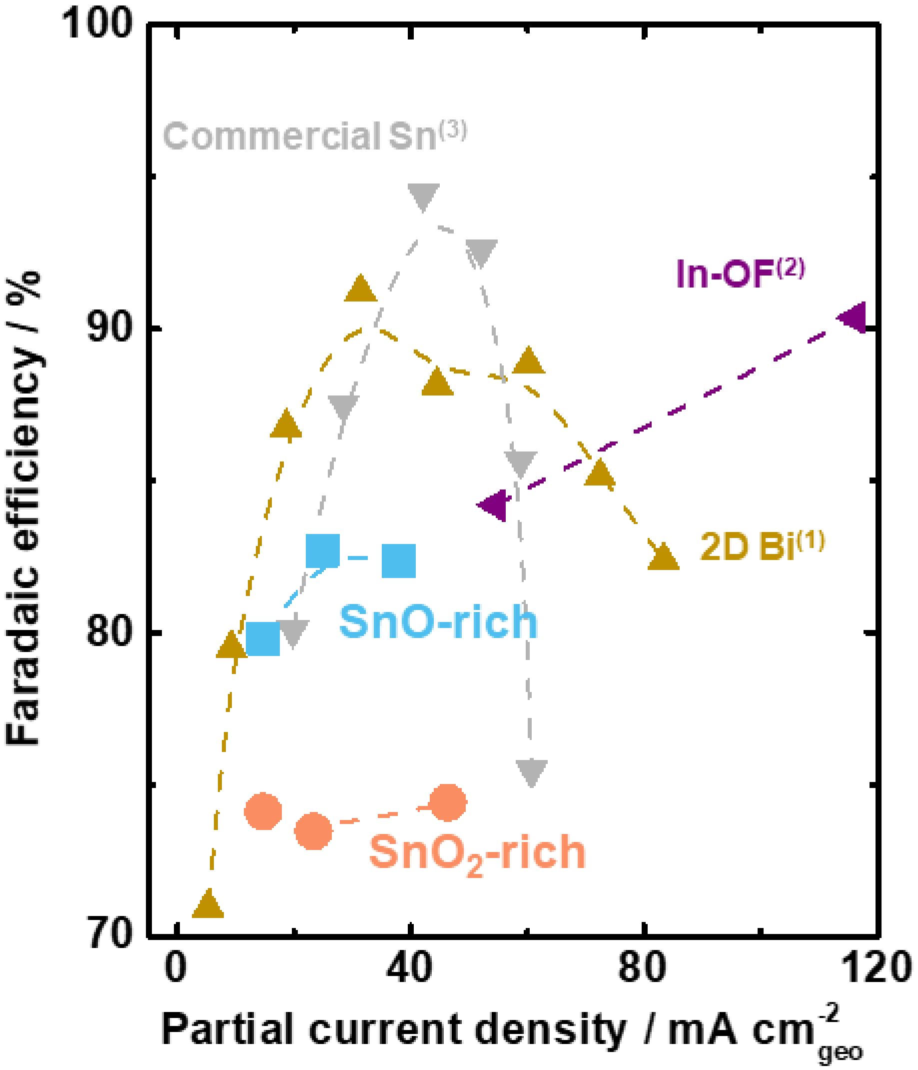

Figure 4.6. Comparison of Faradaic efficiency and geometric partial current density on the Sn oxides catalyst with the state-of-the-art catalysts.

after electrolysis, suggesting that the SnO_2 species generated from post-annealing might be resistive to electrochemically reducing environment, at least on the surface. The peak appeared at around 537 eV is presumably originated from the bicarbonate salt, confirmed by Raman spectra (Figure 4.8). VBM spectra in Figure 4.7B indicates the presence of metallic Sn on both Sn oxide catalysts after electrolysis. However, the portion of metallic Sn relative to SnO_2 on the surface of the SnO_2-rich catalyst after electrolysis is remarkably higher than the surface of the SnO-rich catalyst. On the basis of these observations, we tentatively speculate that the suppressed Faradaic efficiency of formate on the SnO_2-rich catalysts is attributed to the evolution of metallic Sn and remaining SnO_2 during the CO_2 electrolysis as compared to the SnO-rich catalyst, which is consistent with literature.[26]

We assume that the parasitic hydrogen evolution is possibly originated from GDL exposure during electrolysis. Figure 4.9A shows agglomerated particles on both Sn oxide catalysts after electrolysis, which indicates that the surface morphology evolves during electrolysis. Comparing contact angle of H_2O suggests the agglomerated surface morphology exposes GDL to the surface (Figure 4.9B–C), which is further confirmed from energy-dispersive X-ray spectroscopy (SEM-EDS), as shown in Figure 4.10. Figure 4.11 exhibits that purely hydrogen is only product on the surface of bare GDL without any marginal formation CO_2 reduction products. We conjecture that the parasitic hydrogen evolution originated from the partial exposure of GDL during electrolysis slightly impedes the formate selectivity.

4.5 Effect of CO_2 Concentration and Its Flow Rate on the CO_2 Electrolysis

Overall CO_2 conversion activity on the SnO-rich catalyst is curtailed as the concentration of CO_2 stream is reduced from 100% to 3% since the available CO_2 at vicinity of catalyst surface is limited with partially concentrated CO_2, as shown in Figure 4.12A–B. The geometric partial current density of formate decreases from 11.1 to 0.8 mA cm^{-2}, and that of CO also

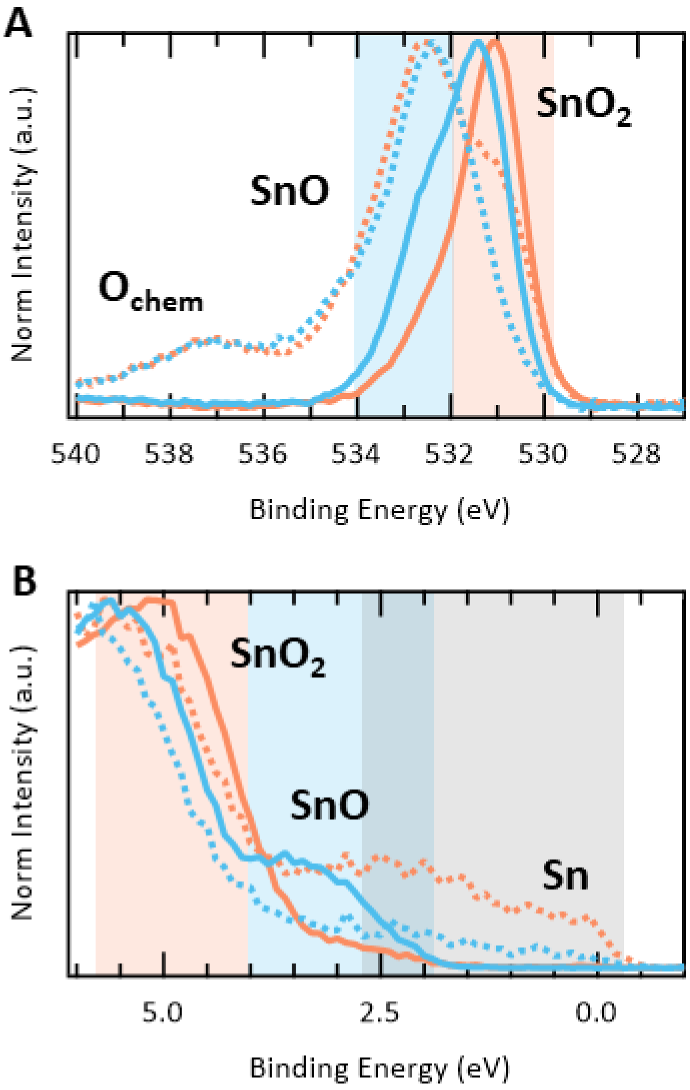

Figure 4.7. XPS after 1 hr of CO_2 electrolysis on SnO-rich (blue) and SnO2-rich (orange). The solid line is for before electrolysis and the dashed line is for after electrolysis. The intensities are normalized.

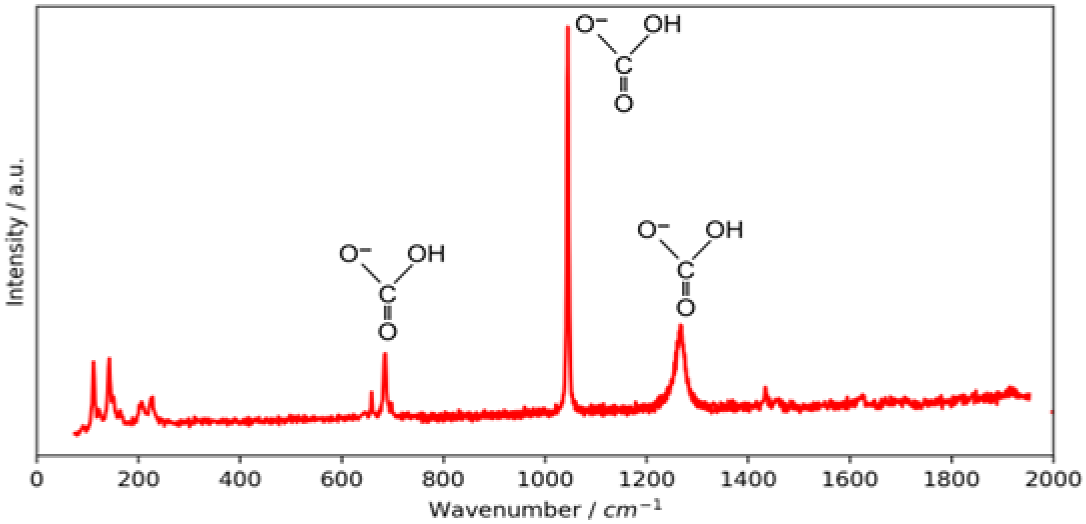

Figure 4.8. Raman spectra on the surface of the representative Sn oxide electrode after 1hr of CO_2 electrolysis.

substantially reduces down to < 1 mA cm^{-2} at a CO_2 flow rate of 100 ml min^{-1}. In general, the partial current density of CO is 10 times smaller than that of formate over the range of CO_2 concentration, which confirms that, regardless of the CO_2 concentration, the CO_2-to-formate reaction is predominant on the SnO-rich catalyst and it is most likely competing with the parasitic hydrogen evolution instead of CO generation. The hydrogen evolution reaction is promoted with lower CO_2 concentration which is probably due to the limited mass transport of CO_2 (Figure 4.12C).

Increasing flow rate of the pure and partially concentrated CO_2 stream from 100 to 200 ml min^{-1} results in $\times\sim1.5$ times improved partial current density of formate while marginally increased partial current densities of CO and H_2 (~1.1 times) are observed at the increased flow rate. We speculate that the improved formate activity is largely attributed to the rapid mass transport of CO_2 to the catalytic sites. Possibly, the increased flow rate of CO_2 may help diffusing out of the generated formate on the catalyst surface to the flow field, which further facilitates CO_2 transport.[125]

It is known that the electrochemical CO_2 conversion to formate is the first order reaction

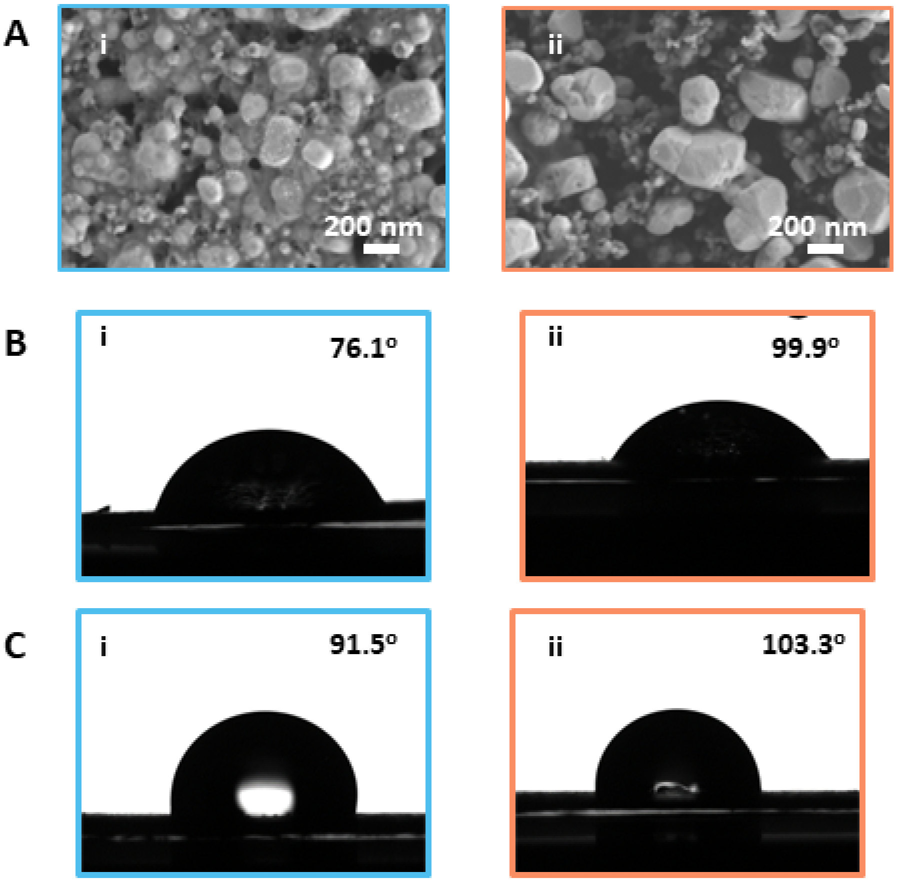

Figure 4.9. Post-electrolysis characterizations. SEM image of A(i) SnO-rich and A(ii) SnO_2-rich catalyst after electrolysis The contact angle of H_2O on SnO-rich B(i) before and C(i) after electrolysis and on SnO_2-rich B(ii) before and C(ii) after electrolysis. The electrolysis is performed for an hour at -3.0 V of cell voltage.

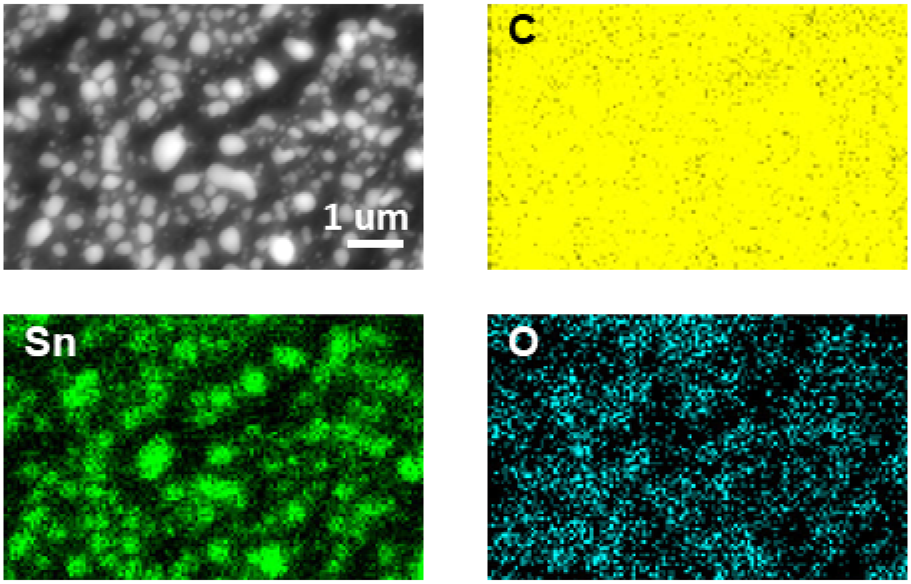

Figure 4.10. SEM-EDS on the SnO-rich catalyst after electrolysis.

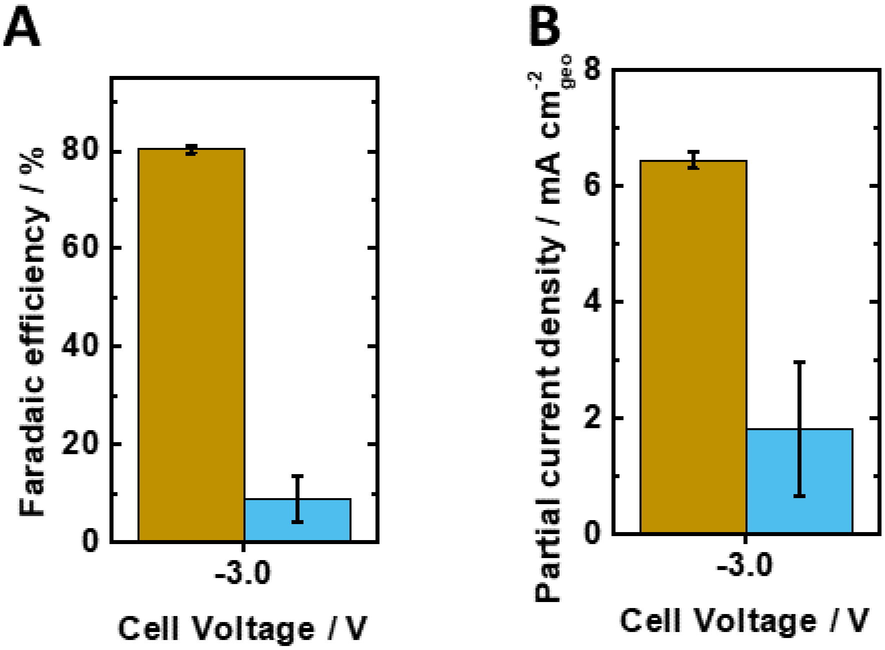

Figure 4.11. Comparison of hydrogen evolution on bare GDL and SnO-rich catalyst. No CO_2 reduction products are detected on the bare GDL. (A) Faradaic efficiency and (B) geometric partial current density of hydrogen.

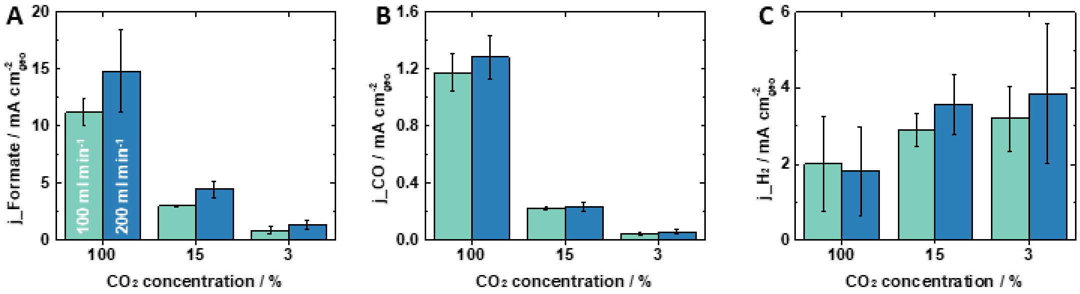

Figure 4.12. Effect of CO_2 flow rate on the catalytic activity with partially concentrated CO_2 stream. The geometric Partial current densities of (A) formate, (B) CO, and (C) hydrogen at a flow rate of 100 and 200 ml min^{-1} of partially concentrated CO_2 stream (100, 15, and 3%). The CO_2 electrolysis is performed on the SnO-rich catalyst at -3.0 V of cell voltage.

as the reaction rate is proportional to the CO_2 concentration,[136], indicating that reaction kinetics of formate generation can be improved with facile CO_2 mass transport. Increasing temperature would enhance kinetics but it will decrease the amount of dissolved CO_2 in the thin liquid layer on the catalyst surface which results in hampered CO_2 transport (Figure 4.13). Considering the three-phase interface system of $CO_{2(g)}$-aqueous medium-catalyst in our CO_2 conversion system, in which the CO_2 diffuses through a very thin liquid layer (=water by osmotic drag through membrane) to reach to the catalyst surface, it is important to account the internal CO_2 mass transfer.[125, 127] In the three-phase interface system, the internal CO_2 mass transfer flux, N, is a function of mass transfer coefficient and the CO_2 concentration gradient, which is proportional to the current density:[137]

$$\Delta C = [CO2]_{bulk} - [CO2]_{interface} \tag{4.1}$$

$$N = k \cdot \Delta C \simeq j_{formate}/nF \tag{4.2}$$

where Δ C is the CO_2 concentration gradient, $[CO_2]_{bulk}$ and $[CO_2]_{interface}$ are the CO_2 concentration in the bulk gas phase and the interface, respectively, k is the mass transfer co-

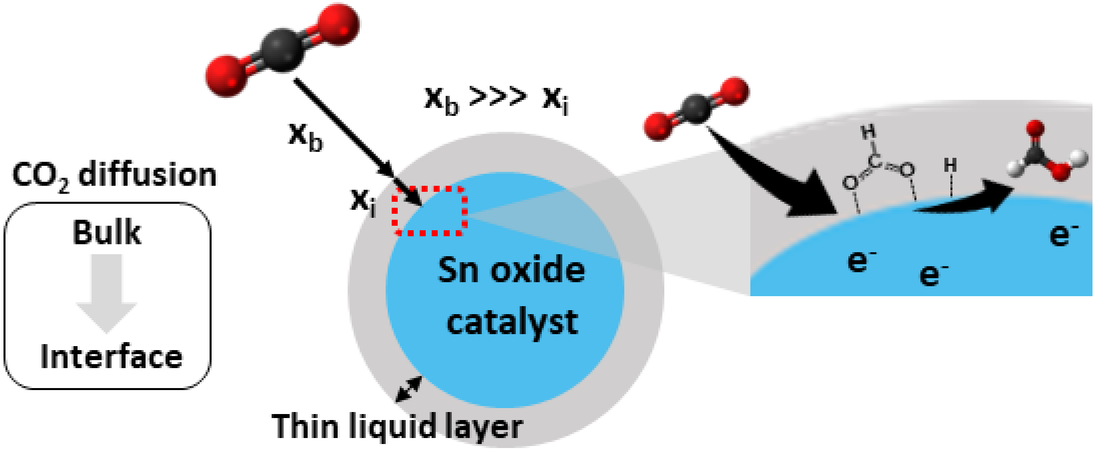

Figure 4.13. Scheme of the simplified CO$_2$ mass transportation to the catalyst surface. The humidified CO$_2$ is diffused to the catalyst surface through GDL (bulk) and the thin liquid layer (interface). *OCHO is the reaction intermediate to the formate.

efficient, $j_{formate}$ is partial current density of formate, n is the number of electrons (=2 for CO$_2$-to-formate), and F is the Faraday constant.

The diffusivity of CO$_2$ during electrochemical CO$_2$ conversion is one of the key factors that affects *k*. Diffusion of CO$_2$ to the thin liquid layer through gas diffusion electrode (GDE) has higher CO$_2$ diffusion coefficient than the solubilized CO$_2$ (16 and 0.0016 mm^2 s^{-1}, respectively), suggesting an improved CO$_2$ transport in the GDE-incorporated CO$_2$ electrolysis system relative to the batch-type reactor.[138] Also, it is assumed that the CO$_2$ mass transfer flux in the gas phase is identical to that in the liquid because the diffusion length, x_i, is negligibly thin as compared to the bulk diffusion length, x_b, as shown in Figure 4.13, which means that the internal CO$_2$ mass transport is not the reaction limiting step and the CO$_2$ mass transfer flux is proportional to the partial current density of formate (equation 4.2).

According to Shi et al.,[137] the mass transfer coefficient, *k*, is shown to be approx. 10 times higher in the three-phase interface system relative to the two-phase inter face system (liquid - solid, batch-type reactor), indicating facile CO$_2$ mass transport in the GDE-incorporated CO$_2$

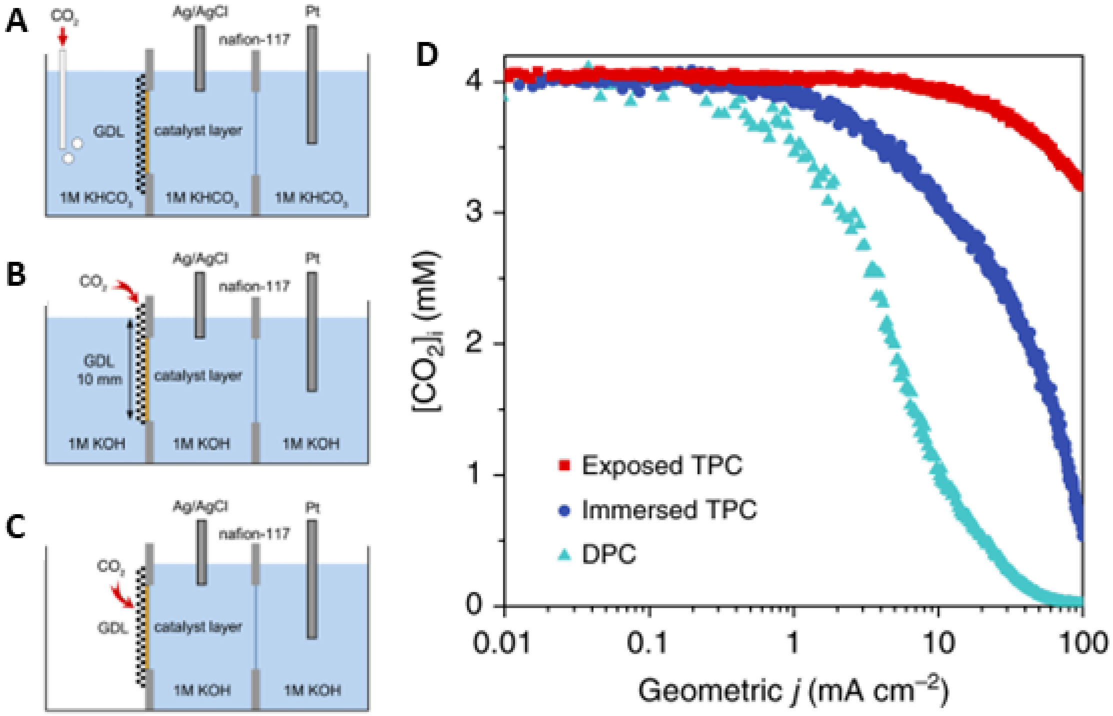

Figure 4.14. Effect of CO_2 transportation on the CO_2 conversion. (A) liquid-solid double-phase contact interface system (DPC) and gas-liquid-solid three-phase contact interface system (B) GDE immersed in electrolyte (Immersed TPC) and (C) GDE exposed to gas (Exposed TPC). (D) CO_2 concentration at the interface as a function of geometric current density. Reproduced with permission from Shi et al Copyright 2020, Springer Nature.

electrolysis system. Figure 4.14 shows that the interface CO_2 concentration is rather sustained even at the higher current density (> 50 mA cm^{-2}) in the three-phase interface system while the double-phase interface system shows rapid decrease in the CO_2 concentration at around 5 mA cm^{-2}. This confirms that the entire CO_2 mass transport is the rate limiting step, as shown in Figure 4.12. In the meantime, the cell voltage is consistent at -3.0 V to keep the effect of the electrochemical reaction rate away from the consideration. Overall, we conclude that the rapid mass transport of CO_2 is a critical factor of designing CO_2 electrolysis system to enhance CO_2 conversion activity.

4.6 Summary

The selectivity and energy efficiency of the electrochemical CO_2 conversion to formate can be enhanced via controlling the initial chemical state of Sn species on the thermally evaporated Sn oxide surface. The improved formate selectivity (83%) is observed as SnO and SnO_2 are co-existed on the surface of GDE at the beginning of CO_2 electrolysis, which leads to 36% of energy efficiency for formate generation at -3.0 V of cell voltage, offering nearest-term net negative CO_2 conversion system. Also, increasing CO_2 flow rate enhances reaction kinetics toward formate generation even at partially concentration CO_2 stream in the catholyte-free electrolyzer, which confirms that sufficient CO_2 mass transport to the catalytic site is a critical design parameter for CO_2 electrolysis reactor. These findings showcase the importance of controlling chemical state of the catalyst and facile mass transport of CO_2 to achieve carbon negative electrochemical CO_2 conversion system.

4.7 Acknowledgement

Chapter 4, in part, is currently being prepared for submission for publication of the material ”Tuning oxidation state of Sn oxides for electrochemical CO_2 to formate conversion in the catholyte–free electrolzyer”, Taewoo Kim, Vivek S. Devalla, Sean P. Dunfield, Sara Dorr,

Moses Kudor, and David P. Fenning. The dissertation author was one of the primary investigators and author of this material.

Chapter 5

Conclusion

To date, there has been many efforts made to improve overall efficiency of CO_2 conversion system to meet carbon neutrality. To increase the efficiency, in–depth understanding of reaction mechanisms and their relationship with physico-chemical properties of catalytic materials are necessary. Also, optimization of electrolyzer design is critical to deliver the insights from the micro-environment to the practical operations, which eventually enables net negative carbon emission.

This thesis provides strategies to design catalytic materials by engineering from nano– to micro–scale characteristics of the materials that shift selectivity and energy efficiency of CO_2 conversion system. Furthermore, this thesis builds bridges between the fundamental understandings and electrolyzer engineering to lessen the knowledge gap to encourage further development in the CO_2 electrolysis field. The main contributions of this thesis include:

- CO_2 reduction reaction pathway can be tuned by surface strain. Modulating the surface strain of a model Cu (001) catalysts epitaxially grown on a single crystal Si (001) substrate shows significant changes in the formation rate of the single carbon products. With increasing tensile strain, the partial current density of single carbon products are suppressed while that of multi–carbon products are rather maintained which gives relatively increased selectivity toward highly energy dense products.
- The changes in the reaction pathway is derived from the electronic structure. The increase

in tensile strain upshifts the Cu 3*d* band center position. This strengthens the binding energy of $*$CO and $*$H to the surface, resulting in promoted coupling reaction between $*$CO and its protonation that eventually suppresses sing carbon products formation. Along with increased $*$H adsorption energy due to the scaling relation, however, the parasitic hydrogen evolution is also promoted that should be addressed to increase energy efficiency.

- Engineering surface morphology can further increase selectivity toward multi–carbon products. The operando restructuring of the micro– and nanoscale morphology of Cu–based catalyst shows enhanced selectivity shifting away from single carbon products but toward multi–carbon products.
- The enhanced selectivity can be attributed to the increased surface defects from structural evolution. As the $Cu(OH)_2$ nanowire catalysts are electrochemically reduced at moderated CO_2 electrolysis potential, a hierarchical morphology appears that provides sufficient surface defects such as surface strain from the volume expansion. Also, increased local pH on the evolve surface structure that favors multi–carbon products formation.
- Tuning the chemical state of catalysts is also a possible way to modulate CO_2 products selectivity. Shifting initial surface oxidation state of tin oxides catalyst from SnO_2-rich to co-existing SnO and SnO_2 shows an improved selectivity and energy efficiency to formate in a MEA-type electrolyzer, which bridges fundamental level strategies to quasi-practical scale research. The improved energy efficiency on the SnO-SnO_2 catalysts in the MEA-type electrolyzer provides a promising approach toward net negative carbon emission.
- Providing a rapid mass transport of CO_2 to the catalyst sites via increasing the flow rate of feed gas can facilitate the CO_2-to-formate reaction kinetics on the tin oxides catalyst even at the partially concentrated CO_2 stream, which is relevant to the flue gas composition. It is experimentally confirmed that the CO_2 mass transport is the rate limiting

step as the electrochemical CO_2-to-formate reaction is known to be the first order reaction, proportional to the CO_2 concentration, which is consistent with our findings.

Of course, many questions could be raised by this work to find the breakthrough of the remaining challenges on designing catalyst and the electrolyzer. For future work, integrating the designing strategies provided by this thesis into preparing nanoparticulate catalysts will be the first mission to apply these insights onto larger scale application. This will require multiple scale characterization and performance evaluation to examine catalytic activities and stability. High throughput screening system might be helpful to test already-existing knowledge and convey them into the catalyst synthesis.

It is critical to avoid parasitic hydrogen evolution reaction during CO_2 conversion to improve overall efficiency of the system. Introducing secondary component (i.e., bimetallic composition) or promoter that has intrinsically low activities toward hydrogen evolution but toward *CO could be an approach. A compressive strain on the single crystal Cu surface might be an interesting research to avoid hydrogen evolution. As the compressive strain lowers $3d$-band center, it reduces binding energy of both *CO and *H according to the scaling relation that could increase CO selectivity and suppress hydrogen evolution on its surface.

Lastly, it is necessary to have in-depth study of electrochemical CO_2 conversion in the composition of flue gas where CO_2 concentration is limited and oxygen is present. Fundamental understandings originated from usages of pure CO_2 are certainly limited to be more practical (e.g., installation of the CO_2 conversion system at the end of point sources, such as power plant). The presence of oxygen induces the other parasitic oxygen reduction reaction, which requires further investigation to increase local CO_2 concentration via ligand engineering such as incorporating amine functional group to leverage its high affinity to CO_2.

Bibliography

[1] National Aeronautics and Space Administration (NASA), "Global Temperature," 2022.

[2] National Aeronautics and Space Administration (NASA), "The Keeling Curve," 2022.

[3] Z. W. Seh, J. Kibsgaard, C. F. Dickens, I. Chorkendorff, J. K. Norskov, and T. F. Jaramillo, "Combining theory and experiment in electrocatalysis: Insights into materials design," *Science*, vol. 355, no. 6321, p. 1, 2017.

[4] K. P. Kuhl, E. R. Cave, D. N. Abram, and T. F. Jaramillo, "New insights into the electrochemical reduction of carbon dioxide on metallic copper surfaces," *Energy & Environmental Science*, vol. 5, pp. 7050–7059, 2012.

[5] T. Kim, A. Kargar, Y. Luo, R. Mohammed, E. Martinez-Loran, A. Ganapathi, P. Shah, and D. P. Fenning, "Enhancing C_2C_3 Production from CO_2 on Copper Electrocatalysts via a Potential- Dependent Mesostructure," *ACS Applied Energy Materials*, vol. 1, no. 5, pp. 1965–1972, 2018.

[6] O. S. Bushuyev, P. D. Luna, C. T. Dinh, L. Tao, G. Saur, J. v. d. Lagemaat, S. O. Kelley, and E. H. Sargent, "What Should We Make with CO2 and How Can We Make It?," *Joule*, vol. 2, no. 5, pp. 825–832, 2018.

[7] S. Verma, B. Kim, H. R. M. Jhong, S. Ma, and P. J. A. Kenis, "A Gross-Margin Model for Defining Technoeconomic Benchmarks in the Electroreduction of CO_2," *ChemSusChem*, vol. 9, no. 15, pp. 1972–1979, 2016.

[8] T. Burdyny and W. A. Smith, "CO_2 Reduction on Gas-Diffusion Electrodes and Why Catalytic Performance Must Be Assessed at Commercially-Relevant Conditions," *Energy & Environmental Science*, vol. 12, no. 5, pp. 1442–1453, 2019.

[9] California Independent System Operator (ISO), "Price map," 2022.

[10] P. De Luna, H. C, H. D., J. S. A., J. T. F., and S. E. H., "What would it take for renewably powered electrosynthesis to displace petrochemical processes?," *Science*, vol. 364, no. 350, 2019.

[11] S. Nitopi, E. Bertheussen, S. B. Scott, X. Liu, A. K. Engstfeld, S. Horch, B. Seger, I. E. L. Stephens, K. Chan, C. Hahn, J. K. Nørskov, T. F. Jaramillo, and I. Chorkendorff, "Progress

and Perspectives of Electrochemical CO_2 Reduction on Copper in Aqueous Electrolyte," *Chemical Reviews*, vol. 119, no. 12, pp. 7610–7672, 2019.

[12] J. Tymoczko, F. Calle-Vallejo, W. Schuhmann, and A. S. Bandarenka, "Making the hydrogen evolution reaction in polymer electrolyte membrane electrolysers even faster," *Nature Communications*, vol. 7, no. 1, p. 10990, 2016.

[13] Y. Hori, I. Takahashi, O. Koga, and N. Hoshi, "Selective Formation of C_2 Compounds from Electrochemical Reduction of CO_2 at a Series of Copper Single Crystal Electrodes," *The Journal of Physical Chemistry B*, vol. 106, no. 1, pp. 15–17, 2002.

[14] K. P. Kuhl, T. Hatsukade, E. R. Cave, D. N. Abram, J. Kibsgaard, and T. F. Jaramillo, "Electrocatalytic Conversion of Carbon Dioxide to Methane and Methanol on Transition Metal Surfaces," *Journal of the American Chemical Society*, vol. 136, no. 40, pp. 14107–14113, 2014.

[15] T. Bligaard and J. Nørskov, "Heterogeneous Catalysis. In Chemical Bonding at Surfaces and Interfaces," *Chemical Bonding at Surfaces and Interfaces*, pp. 255–321, 2008.

[16] A. Verdaguer-Casadevall, C. W. Li, T. P. Johansson, S. B. Scott, J. T. McKeown, M. Kumar, I. E. L. Stephens, M. W. Kanan, and I. Chorkendorff, "Probing the Active Surface Sites for CO Reduction on Oxide-Derived Copper Electrocatalysts," *Journal of the American Chemical Society*, vol. 137, no. 31, pp. 9808–9811, 2015.

[17] K. Jiang, Y. Huang, G. Zeng, F. M. Toma, W. Goddard, and A. T. Bell, "Effects of Surface Roughness on the Electrochemical Reduction of CO_2 over Cu," *ACS Energy Letters*, vol. 5, no. 4, pp. 1206–1214, 2020.

[18] R. B. Sandberg, J. H. Montoya, K. Chan, and J. K. Nørskov, "CO-CO Coupling on Cu Facets: Coverage, Strain and Field Effects," *Surface Science*, vol. 654, pp. 56–62, 2016.

[19] R. Reske, M. Duca, M. Oezaslan, K. J. P. Schouten, M. T. M. Koper, and P. Strasser, "Controlling Catalytic Selectivities during CO_2 Electroreduction on Thin Cu Metal Overlayers," *The Journal of Physical Chemistry Letters*, vol. 4, no. 15, pp. 2410–2413, 2013.

[20] H. Huang, H. Jia, Z. Liu, P. Gao, J. Zhao, Z. Luo, J. Yang, and J. Zeng, "Understanding of Strain Effects in the Electrochemical Reduction of CO_2: Using Pd Nanostructures as an Ideal Platform," *Angewandte Chemie International Edition*, vol. 56, no. 13, pp. 3594–3598, 2017.

[21] W. Tang, A. A. Peterson, A. S. Varela, Z. P. Jovanov, L. Bech, W. J. Durand, S. Dahl, J. K. Norskov, and I. Chorkendorff, "The Importance of Surface Morphology in Controlling the Selectivity of Polycrystalline Copper for CO_2 Electroreduction," *Physical Chemistry Chemical Physics*, vol. 14, no. 1, pp. 76–81, 2012.

[22] M. R. Goncalves, A. Gomes, J. Condeco, R. Fernandes, T. Pardal, C. A. C. Sequeira, and J. B. Branco, "Selective Electrochemical Conversion of CO_2 to C_2 Hydrocarbons," *Energy Conversion and Management*, vol. 51, no. 1, pp. 30–32, 2010.

[23] D. Raciti, K. J. Livi, and C. Wang, "Highly Dense Cu Nanowires for Low-Overpotential CO_2 Reduction," *Nano Letters*, vol. 15, no. 10, pp. 6829–6835, 2015.

[24] J. T. Feaster, C. Shi, E. R. Cave, T. Hatsukade, D. N. Abram, K. P. Kuhl, C. Hahn, J. K. Nørskov, and T. F. Jaramillo, "Understanding Selectivity for the Electrochemical Reduction of Carbon Dioxide to Formic Acid and Carbon Monoxide on Metal Electrodes," *ACS Catalysis*, vol. 7, no. 7, pp. 4822–4827, 2017.

[25] Y. Chen and M. W. Kanan, "Tin oxide dependence of the CO2 reduction efficiency on tin electrodes and enhanced activity for tin/tin oxide thin-film catalysts," *Journal of the American Chemical Society*, vol. 134, no. 4, pp. 1986–1989, 2012.

[26] A. Dutta, A. Kuzume, M. Rahaman, S. Vesztergom, and P. Broekmann, "Monitoring the Chemical State of Catalysts for CO2 Electroreduction: An In Operando Study," *ACS Catalysis*, vol. 5, no. 12, pp. 7498–7502, 2015.

[27] Y. Hori, H. Konishi, T. Futamura, A. Murata, O. Koga, H. Sakurai, and K. Oguma, ""Deactivation of copper electrode" in electrochemical reduction of CO_2," *Electrochimica Acta*, vol. 50, no. 27, pp. 5354–5369, 2005.

[28] Y. Y. Birdja, E. Pérez-Gallent, M. C. Figueiredo, A. J. Göttle, F. Calle-Vallejo, and M. T. M. Koper, "Advances and Challenges in Understanding the Electrocatalytic Conversion of Carbon Dioxide to Fuels," *Nature Energy*, vol. 4, no. 9, pp. 732–745, 2019.

[29] L. Wang, S. A. Nitopi, E. Bertheussen, M. Orazov, C. G. Morales-guio, X. Liu, D. C. Higgins, K. Chan, J. K. Nørskov, C. Hahn, and T. F. Jaramillo, "Electrochemical Carbon Monoxide Reduction on Polycrystalline Copper: Effects of Potential, Pressure, and PH on Selectivity toward Multicarbon and Oxygenated Products," *ACS Catalysis*, vol. 8, no. 8, pp. 7445–7454, 2018.

[30] Y. Zheng, A. Vasileff, X. Zhou, Y. Jiao, M. Jaroniec, and S. Qiao, "Understanding the Roadmap for Electrochemical Reduction of CO_2 to Multi-Carbon Oxygenates and Hydrocarbons on Copper-Based Catalysts," *Journal of the American Chemical Society*, vol. 141, no. 19, pp. 7646–7659, 2019.

[31] D. Ren, J. Fong, and B. S. Yeo, "The Effects of Currents and Potentials on the Selectivities of Copper toward Carbon Dioxide Electroreduction," *Nature Communications*, vol. 9, no. 1, p. 925, 2018.

[32] A. J. Garza, A. T. Bell, and M. Head-Gordon, "Mechanism of CO_2 Reduction at Copper Surfaces: Pathways to C_2 Products," *ACS Catalysis*, vol. 8, no. 2, pp. 1490–1499, 2018.

[33] J. D. Goodpaster, A. T. Bell, and M. Head-gordon, "Identification of Possible Pathways for CC Bond Formation during Electrochemical Reduction of CO_2: New Theoretical Insights from an Improved Electrochemical Model," *The Journal of Physical Chemistry Letters*, vol. 7, no. 8, pp. 1471–1477, 2016.

[34] F. Calle-Vallejo and M. T. M. Koper, "Theoretical Considerations on the Electroreduction of CO to C_2 Species on Cu(100) Electrodes. ," *Angewandte Chemie International Edition*, vol. 52, no. 28, pp. 7282–7285, 2013.

[35] R. Reske, H. Mistry, F. Behafarid, B. Roldan Cuenya, and P. Strasser, "Particle Size Effects in the Catalytic Electroreduction of CO_2 on Cu Nanoparticles," *Journal of the American Chemical Society*, vol. 136, no. 19, pp. 6978–6986, 2014.

[36] D. Higgins, A. T. Landers, Y. Ji, S. Nitopi, C. G. Morales-guio, L. Wang, K. Chan, C. Hahn, and T. F. Jaramillo, "Guiding Electrochemical Carbon Dioxide Reduction toward Carbonyls Using Copper Silver Thin Films with Interphase Miscibility," *ACS Energy Letters*, vol. 3, no. 12, pp. 2947–2955, 2018.

[37] R. P. Jansonius, L. M. Reid, C. N. Virca, and C. P. Berlinguette, "Strain Engineering Electrocatalysts for Selective CO_2 Reduction," *ACS Energy Letters*, vol. 4, no. 4, pp. 980–986, 2019.

[38] J. K. Norskov, F. Abild-pedersen, F. Studt, and T. Bligaard, "Density Functional Theory in Surface Chemistry and Catalysis," *Proceedings of the National Academy of Sciences*, vol. 108, no. 3, pp. 937–943, 2011.

[39] M. Mavrikakis, B. Hammer, and J. K. Nørskov, "Effect of Strain on the Reactivity of Metal Surfaces," *Physical Review Letters*, vol. 81, no. 13, pp. 2819–2822, 1998.

[40] M. Luo and S. Guo, "Strain-Controlled Electrocatalysis on Multimetallic Nanomaterials," *Nature Reviews Materials*, vol. 2, no. 11, p. 17059, 2017.

[41] S. Ma, M. Sadakiyo, M. Heim, R. Luo, R. T. Haasch, J. I. Gold, M. Yamauchi, and P. J. A. Kenis, "Electroreduction of Carbon Dioxide to Hydrocarbons Using Bimetallic Cu-Pd Catalysts with Different Mixing Patterns," *Journal of the American Chemical Society*, vol. 139, no. 1, pp. 47–50, 2017.

[42] Y. Huang, A. Handoko, P. Hirunsit, and B. S. Yeo, "Electrochemical Reduction of CO_2 Using Copper Single-Crystal Surfaces: Effects of CO^* Coverage on the Selective Formation of Ethylene," *ACS Catalysis*, vol. 7, no. 3, pp. 1749–1756, 2017.

[43] C. Hahn, T. Hatsukade, Y.-G. Kim, A. Vailionis, J. H. Baricuatro, D. C. Higgins, S. A. Nitopi, M. P. Soriaga, and T. F. Jaramillo, "Engineering Cu Surfaces for the Electrocatalytic Conversion of CO_2: Controlling Selectivity toward Oxygenates and Hydrocarbons," *Proceedings of the National Academy of Sciences*, vol. 114, no. 23, pp. 5918–5923, 2017.

[44] J. Resasco, L. D. Chen, E. Clark, C. Tsai, C. Hahn, T. F. Jaramillo, K. Chan, and A. T. Bell, "Promoter Effects of Alkali Metal Cations on the Electrochemical Reduction of Carbon Dioxide," *Journal of the American Chemical Society*, vol. 139, no. 32, pp. 11277–11287, 2017.

[45] J. H. Montoya, C. Shi, K. Chan, and J. K. Nørskov, "Theoretical Insights into a CO Dimerization Mechanism in CO_2 Electroreduction," *The Journal of Physical Chemistry Letters*, vol. 6, no. 11, pp. 2032–2037, 2015.

[46] C. Shi, H. A. Hansen, A. C. Lausche, and J. K. Nørskov, "Trends in Electrochemical CO_2 reduction Activity for Open and Close-Packed Metal Surfaces," *Physical Chemistry Chemical Physics*, vol. 16, no. 10, p. 4720, 2014.

[47] D. Lee, A. Yoon, S. Y. Jang, j. Yoon, J. Chung, M. Kim, J. F. Scott, and T. W. Noh, "Giant Flexoelectric Effect in Ferroelectric Epitaxial Thin Films," *Physical Review Letters*, vol. 107, no. 5, p. 057602, 2011.

[48] Z. Lin, C. Mei, L. Wei, Z. Sun, S. Wu, H. Huang, S. Zhang, C. Liu, Y. Feng, H. Tian, H. Yang, J. Li, Y. Wang, G. Zhang, Y. Lu, and Y. Zhao, "Quasi-two-dimensional superconductivity in FeSe 0.3 Te 0.7 thin films and electric-field modulation of superconducting transition," *Scientific Reports*, vol. 5, no. 1, p. 14133, 2015.

[49] A. Wuttig and Y. Surendranath, "Impurity Ion Complexation Enhances Carbon Dioxide Reduction Catalysis," *ACS Catalysis*, vol. 5, no. 7, pp. 4479–4484, 2015.

[50] F. Cemin, D. Lundin, C. Furgeaud, A. Michel, G. Amiard, T. Minea, and G. Abadias, "Epitaxial Growth of Cu(001) Thin Films onto Si(001) Using a Single–Step HiPIMS Process," *Scientific Reports*, vol. 7, no. 1, p. 1655, 2017.

[51] H. Jiang, T. J. Klemmer, J. A. Barnard, and E. A. Payzant, "Epitaxial Growth of Cu on Si by Magnetron Sputtering," *Journal of Vacuum Science Technology A: Vacuum, Surfaces, and Films*, vol. 16, no. 6, pp. 3376–3383, 1998.

[52] C. M. Hull and J. A. Switzer, "Electrodeposited Epitaxial Cu(100) on Si(100) and Lift-Off of Single Crystal-like Cu(100) Foils," *ACS Applied Materials Interfaces*, vol. 10, no. 44, pp. 38596–38602, 2018.

[53] J. W. Matthews and A. E. Blakeslee, "Defects in Epitaxial Multilayers* I. Misfit Dislocations," *Journal of Crystal Growth*, vol. 27, pp. 118–125, 1974.

[54] T. Hofmann, T. H. Yu, M. Folse, L. Weinhardt, M. Bär, Y. Zhang, B. V. Merinov, D. J. Myers, W. A. Goddard, and C. Heske, "Using Photoelectron Spectroscopy and Quantum Mechanics to Determine D-Band Energies of Metals for Catalytic Applications," *The Journal of Physical Chemistry C*, vol. 117, no. 13, pp. 6916–6917, 2013.

[55] J. A. Thornton, "Structure-Zone Models Of Thin Films," *Proc. SPIE*, vol. 821, pp. 95–103, 1988.

[56] R. Messier, A. P. Giri, and R. A. Roy, "Revised Structure Zone Model for Thin Film Physical Structure," *Journal of Vacuum Science Technology A: Vacuum, Surfaces, and Films*, vol. 2, no. 2, pp. 500–503, 1984.

[57] L.-S. Huang and J. Chen, “Analysis of Variance, Coefficient of Determination And F–Test for Local Polynomial Regression,” *Annals of Statistics*, vol. 36, no. 5, pp. 2085–2109, 2008.

[58] K. Liu, W. A. Smith, and T. Burdyny, “Introductory Guide to Assembling and Operating Gas Diffusion Electrodes for Electrochemical CO_2 Reduction,” *ACS Energy Letters*, vol. 4, no. 3, pp. 639–643, 2019.

[59] D. Higgins, C. Hahn, C. Xiang, T. F. Jaramillo, and A. Z. Weber, “Gas-Diffusion Electrodes for Carbon Dioxide Reduction: A New Paradigm,” *ACS Energy Letters*, vol. 4, no. 1, pp. 317–324, 2019.

[60] K. Liu, M. Ma, L. Wu, M. Valenti, D. Cardenas-Morcoso, J. P. Hofmann, J. Bisquert, S. Gimenez, and W. A. Smith, “Electronic Effects Determine the Selectivity of Planar Au-Cu Bimetallic Thin Films for Electrochemical CO2 Reduction,” *ACS Applied Materials Interfaces*, vol. 11, no. 18, pp. 16546–16555, 2019.

[61] M. B. Ross, C. T. Dinh, Y. Li, D. Kim, P. De Luna, E. H. Sargent, and P. Yang, “Tunable Cu Enrichment Enables Designer Syngas Electrosynthesis from CO_2,” *Journal of the American Chemical Society*, vol. 139, no. 27, pp. 9359–9363, 2017.

[62] A. Bagger, L. Arnarson, M. H. Hansen, E. Spohr, and J. Rossmeisl, “Electrochemical CO Reduction: A Property of the Electrochemical Interface,” *Journal of the American Chemical Society*, vol. 141, no. 4, pp. 1506–1514, 2019.

[63] W. Luo, X. Nie, M. J. Janik, and A. Asthagiri, “Facet Dependence of CO_2 Reduction Paths on Cu Electrodes,” *ACS Catalysis*, vol. 6, no. 1, pp. 219–229, 2016.

[64] T. Cheng, H. Xiao, and W. A. Goddard, “Nature of the Active Sites for CO Reduction on Copper Nanoparticles; Suggestions for Optimizing Performance,” *Journal of the American Chemical Society*, vol. 139, no. 34, pp. 11642–11645, 2017.

[65] C. W. Li, J. Ciston, and M. W. Kanan, “Electroreduction of Carbon Monoxide to Liquid Fuel on Oxide-Derived Nanocrystalline Copper,” *Nature*, vol. 508, no. 7497, pp. 504–507, 2014.

[66] R. G. Mariano, K. McKelvey, H. S. White, and M. W. Kanan, “Selective Increase in CO_2 Electroreduction Activity at Grain–Boundary Surface Terminations,” *Science*, vol. 358, no. 6367, pp. 1187–1192, 2017.

[67] X. Feng, K. Jiang, S. Fan, and M. W. Kanan, “A Direct Grain- Boundary-Activity Correlation for CO Electroreduction on Cu Nanoparticles,” *ACS Central Science*, vol. 2, no. 3, pp. 169–174, 2016.

[68] L. Zhang, Y. Yuan, J. Lapano, M. Brahlek, S. Lei, B. Kabius, V. Gopalan, and R. Engel-Herbert, “Continuously Tuning Epitaxial Strains by Thermal Mismatch,” *ACS Nano*, vol. 12, no. 2, pp. 1306–1312, 2018.

[69] K. A. Bush, N. Rolston, A. Gold-parker, S. Manzoor, J. Hausele, Z. J. Yu, J. A. Raiford, R. Cheacharoen, Z. C. Holman, M. F. Toney, R. H. Dauskardt, and M. D. Mcgehee, “Controlling Thin- Film Stress and Wrinkling during Perovskite Film Formation,” *ACS Energy Letters*, vol. 3, no. 6, pp. 1225–1232, 2018.

[70] M. A. Moram and M. E. Vickers, “X-Ray Diffraction of III-Nitrides,” *Reports on Progress in Physics*, vol. 72, no. 3, p. 036502, 2009.

[71] A. E. Romanov, W. Pompe, G. Beltz, and J. S. Speck, “Modeling of Threading Dislocation Density Reduction in Heteroepitaxial Layers,” *physica status solidi (b)*, vol. 198, no. 2, pp. 599–613, 1996.

[72] J. E. Ayers, “The Measurement of Threading Dislocation Densities in Semiconductor Crystals by X-Ray Diffraction,” *Journal of Crystal Growth*, vol. 135, no. 1–2, pp. 71–77, 1994.

[73] W. J. Durand, A. A. Peterson, F. Studt, F. Abild-pedersen, and J. K. Nørskov, “Surface Science Structure Effects on the Energetics of the Electrochemical Reduction of CO_2 by Copper Surfaces,” *Surface Science*, vol. 605, no. 15–16, pp. 1354–1359, 2011.

[74] Y. Zheng, A. Vasileff, X. Zhou, Y. Jiao, M. Jaroniec, and S. Z. Qiao, “Understanding the Roadmap for Electrochemical Reduction of CO_2 to Multi–Carbon Oxygenates and Hydrocarbons on Copper–Based Catalysts,” *Journal of the American Chemical Society*, vol. 141, no. 19, pp. 7646–7659, 2019.

[75] S. Bai, Q. Shao, P. Wang, Q. Dai, X. Wang, and X. Huang, “Highly Active and Selective Hydrogenation of CO_2 to Ethanol by Ordered Pd–Cu Nanoparticles,” *Journal of the American Chemical Society*, vol. 139, no. 20, pp. 6827–6830, 2017.

[76] T. Cheng, H. Xiao, and W. A. Goddard, “Reaction Mechanisms for the Electrochemical Reduction of CO_2 to CO and Formate on the Cu(100) Surface at 298 K from Quantum Mechanics Free Energy Calculations with Explicit Water,” *Journal of the American Chemical Society*, vol. 138, no. 42, pp. 13802–13805, 2016.

[77] W. Ma, S. Xie, T. Liu, Q. Fan, J. Ye, F. Sun, Z. Jiang, Q. Zhang, J. Cheng, and Y. Wang, “Electrocatalytic Reduction of CO_2 to Ethylene and Ethanol through Hydrogen–Assisted C-C Coupling over Fluorine-Modified Copper,” *Nature Catalysis*, vol. 3, no. 6, pp. 478–487, 2020.

[78] W. Ma, S. Xie, X. G. Zhang, F. Sun, J. Kang, Z. Jiang, Q. Zhang, D. Y. Wu, and Y. Wang, “Promoting Electrocatalytic CO_2 Reduction to Formate via Sulfur-Boosting Water Activation on Indium Surfaces,” *Nature Communications*, vol. 10, no. 1, p. 892, 2019.

[79] X. Wang, A. Xu, F. Li, S. Hung, D. Nam, C. M. Gabardo, Z. Wang, Y. Xu, A. Ozden, A. S. Rasouli, A. H. Ip, D. Sinton, and E. H. Sargent, “Efficient Methane Electrosynthesis Enabled by Tuning Local CO_2 Availability,” *Journal of the American Chemical Society*, vol. 142, no. 7, pp. 3525–3531, 2020.

[80] T. Sanford, P. C. Frumhoff, A. Luers, and J. Gulledge, “The Climate Policy Narrative for a Dangerously Warming World,” *Nature Climate Change*, vol. 4, no. 3, pp. 164–166, 2014.

[81] G. P. Peters, R. M. Andrew, T. Boden, J. G. Canadell, P. Ciais, C. Le Quere, G. Marland, M. R. Raupach, and C. Wilson, “The Challenge to Keep Global Warming below 2 °C,” *Nature Climate Change*, vol. 3, no. 1, pp. 4–6, 2013.

[82] A. Harriman, “Prospects for Conversion of Solar Energy into Chemical Fuels: The Concept of a Solar Fuels,” *Philosophical Transactions of the Royal Society A: Mathematical, Physical and Engineering Sciences*, vol. 371, no. 1996, p. 20110415, 2013.

[83] M. Aresta, A. Dibenedetto, and A. Angelini, “Catalysis for the Valorization of Exhaust Carbon: from CO_2 to Chemicals, Materials, and Fuels. Technological Use of CO_2,” *Chemical Reviews*, vol. 114, no. 3, pp. 1709–1742, 2014.

[84] M. Peters, B. Kohler, W. Kuckshinrichs, W. Leitner, P. Markewitz, and T. E. Muller, “ Chemical Technologies for Exploiting and Recycling Carbon Dioxide into the Value Chain,” *ChemSusChem*, vol. 4, no. 9, pp. 1216–1240, 2011.

[85] Y. Hori, H. Wakebe, T. Tsukamoto, and O. Koga, “Electrocatalytic Process of CO Selectivity in Electrochemical Reduction of CO2 at Metal Electrodes in Aqueous Media,” *Electrochimica Acta*, vol. 39, no. 11–12, pp. 1833–1839, 1994.

[86] M. Gattrell, N. Gupta, and A. Co, “A Review of the Aqueous Electrochemical Reduction of CO_2 to Hydrocarbons at Copper,” *Journal of Electroanalytical Chemistry*, vol. 594, no. 1, pp. 1–19, 2006.

[87] C. Costentin, M. Robert, and J.-M. Saveant, “Catalysis of the Electrochemical Reduction of Carbon Dioxide,” *Chemical Society Reviews*, vol. 42, no. 6, pp. 2423–2436, 2013.

[88] G. A. Mills and E. E. Ecklund, “Alcohols As Components of Transportation Fuels,” *Annual Review of Energy*, vol. 12, pp. 47–80, 1987.

[89] H. Shapouri, J. A. Duffield, and M. Wang, “The Energy Balance of Corn Ethanol Revisited,” *Energy Policy*, vol. 35, no. 2, pp. 1414–1416, 2007.

[90] A. Frassoldati, A. Cuoci, T. Faravelli, U. Niemann, E. Ranzi, R. Seiser, and K. Seshadri, “An Experimental and Kinetic Modeling Study of N-Propanol and Iso-Propanol Combustion,” *Combustion and Flame*, vol. 157, no. 1, pp. 2–16, 2010.

[91] A. E. Farrell, R. J. Plevin, B. T. Turner, A. D. Jones, M. O’Hare, and D. M. Kammen, “Ethanol Can Contribute to Energy and Environmental Goals,” *Science*, vol. 311, no. 5760, pp. 506–508, 2006.

[92] G. A. Olah, A. Goeppert, and G. K. S. Prakash, “Chemical Recycling of Carbon Dioxide to Methanol and Dimethyl Ether: From Greenhouse Gas to Renewable,” *The Journal of Organic Chemistry*, vol. 74, no. 2, pp. 487–498, 2009.

[93] X. Wang, Y. Zhu, A. Vasileff, Y. Jiao, S. Chen, L. Song, B. Zheng, Y. Zheng, and S.-Z. Qiao, “Strain Effect in Bimetallic Electrocatalysts in the Hydrogen Evolution Reaction,” *ACS Energy Letters*, vol. 3, no. 5, pp. 1198–1204, 2018.

[94] R. Shiratsuchi, Y. Aikoh, and G. Nogami, “Pulsed Electroreduction of CO_2 on Copper Electrodes,” *Journal of The Electrochemical Society*, vol. 140, no. 12, pp. 3479–3482, 1993.

[95] J. Yano, T. Morita, K. Shimano, Y. Nagami, and S. Yamasaki, “Selective ethylene formation by pulse-mode electrochemical reduction of carbon dioxide using copper and copper-oxide electrodes,” *Journal of Solid State Electrochemistry*, vol. 11, no. 4, pp. 554–557, 2007.

[96] S. Sen, D. Liu, and G. T. R. Palmore, “Electrochemical Reduction of CO_2 at Copper Nanofoams,” *ACS Catalysis*, vol. 4, no. 9, pp. 3091–3095, 2014.

[97] Q. Lu, J. Rosen, Y. Zhou, G. S. Hutchings, Y. C. Kimmel, J. G. Chen, and F. Jiao, “A Selective and Efficient Electrocatalyst for Carbon Dioxide Reduction,” *Nature Communications*, vol. 5, no. 1, p. 3242, 2014.

[98] T. Kim, G.-P. Kim, J. Jang, S. E. Shim, W.-S. Ahn, and S.-H. Baeck, “An Investigation on the Selective Hydrodealkylation of C_9^+ Aromatics over Alkali–Treated Pt/H–ZSM–5 Zeolites,” *Catalysis Science Technology*, vol. 6, no. 14, pp. 5599–5607, 2016.

[99] D. Lim, J. Jang, T. Kim, S. E. Shim, and S.-H. Baeck, “Selective Hydrodealkylation of C_9^+ Aromatics to Benzene, Toluene, and Xylenes (BTX) over a Pt/H–ZSM–5 Catalyst,” *Journal of Molecular Catalysis A: Chemical*, vol. 407, pp. 147–151, 2015.

[100] H. Boo, S. Park, B. Ku, Y. Kim, J. H. Park, H. C. Kim, and T. D. Chung, “Ionic Strength-Controlled Virtual Area of Mesoporous Platinum Electrode,” *Journal of the American Chemical Society*, vol. 126, no. 14, pp. 4524–4525, 2004.

[101] C. W. Li and M. W. Kanan, “CO_2 Reduction at Low Overpotential on Cu Electrodes Resulting from the Reduction of Thick Cu_2O Films,” *Journal of the American Chemical Society*, vol. 134, no. 17, pp. 7231–7234, 2012.

[102] C. S. Chen, J. H. Wan, and B. S. Yeo, “Electrochemical Reduction of Carbon Dioxide to Ethane Using Nanostructured Cu2O-Derived Copper Catalyst and Palladium(II) Chloride,” *The Journal of Physical Chemistry C*, vol. 119, no. 48, pp. 26875–26882, 2015.

[103] D. Ren, Y. Deng, A. D. Handoko, C. S. Chen, S. Malkhandi, and B. S. Yeo, “Selective Electrochemical Reduction of Carbon Dioxide to Ethylene and Ethanol on Copper(I) Oxide Catalysts,” *ACS Catalysis*, vol. 5, no. 5, pp. 2814–2821, 2015.

[104] R. Kas, R. Kortlever, A. Milbrat, M. T. M. Koper, G. Mul, and J. Baltrusaitis, “Electrochemical CO 2 Reduction on Cu 2 O-Derived Copper Nanoparticles: Controlling the Catalytic Selectivity of Hydrocarbons,” *Physical Chemistry Chemical Physics*, vol. 16, no. 24, pp. 12194–12201, 2014.

[105] D. Ren, N. T. Wong, A. D. Handoko, Y. Huang, and B. S. Yeo, "Mechanistic Insights into the Enhanced Activity and Stability of Agglomerated Cu Nanocrystals for the Electrochemical Reduction of Carbon Dioxide to N-Propanol," *The Journal of Physical Chemistry Letters*, vol. 7, no. 1, pp. 20–24, 2016.

[106] M. Ma, K. Djanashvili, and W. A. Smith, "Selective Electrochemical Reduction of CO 2 to CO on CuO-Derived Cu Nanowires," *Physical Chemistry Chemical Physics*, vol. 17, no. 32, pp. 20861–20867, 2015.

[107] M. Ma, K. Djanashvili, and W. A. Smith, "Controllable Hydrocarbon Formation from the Electrochemical Reduction of CO 2 over Cu Nanowire Arrays," *Angewandte Chemie International Edition*, vol. 55, no. 23, pp. 6680–6684, 2016.

[108] R. Kas, R. Kortlever, H. Yilmaz, M. T. M. Koper, and G. Mul, "Manipulating the Hydrocarbon Selectivity of Copper Nanoparticles in CO_2 Electroreduction by Process Conditions," *ChemElectroChem*, vol. 2, no. 3, pp. 354–358, 2015.

[109] N. Gupta, M. Gattrell, and B. MacDougall, "Calculation for the Cathode Surface Concentrations in the Electrochemical Reduction of CO_2 in $KHCO_3$ Solutions," *Journal of Applied Electrochemistry*, vol. 36, no. 2, pp. 161–172, 2006.

[110] W. Zhang, X. Wen, S. Yang, Y. Berta, and Z. L. Wang, "Single-Crystalline Scroll-Type Nanotube Arrays of Copper Hydroxide Synthesized at Room Temperature," *Advanced Materials*, vol. 15, no. 10, pp. 822–825, 2003.

[111] Z. Li, Y. Xin, Z. Zhang, H. Wu, and P. Wang, "Rational Design of Binder-Free Noble Metal/metal Oxide Arrays with Nanocauliflower Structure for Wide Linear Range Nonenzymatic Glucose Detection," *Scientific Reports*, vol. 5, no. 1, p. 10617, 2015.

[112] X. Chen, L. Kong, D. Dong, G. Yang, L. Yu, J. Chen, and P. Zhang, "Fabrication of Functionalized Copper Compound Hierarchical Structure with Bionic Superhydrophobic Properties," *The Journal of Physical Chemistry C*, vol. 113, no. 14, pp. 5396–5401, 2009.

[113] S. Cheng and M. Chen, "Fabrication, Characterization, and Kinetic Study of Vertical Single-Crystalline CuO Nanowires on Si Substrates," *Nanoscale Research Letters*, vol. 7, no. 1, p. 119, 2012.

[114] G. Hatui, G. Nayak, G. Udayabhanu, Y. K. Mishra, and D. D. Pathak, "Template-Free Single Pot Synthesis of SnS_2 @Cu_2O/reduced Graphene Oxide (rGO) Nanoflowers for High Performance Supercapacitors," *New Journal of Chemistry*, vol. 41, pp. 2702–2716, 2017.

[115] S. Nalini, S. Nandini, M. B. Reddy, G. S. Suresh, J. S. Melo, S. E. Neelagund, H. N. NaveenKumar, and S. Shanmugam, "A Novel Bioassay Based Gold Nanoribbon Biosensor to Aid the Preclinical Evaluation of Anticancer Properties," *RSC Advances*, vol. 6, pp. 60693–60703, 2016.

[116] C. E. Sunday, M. Bilibana, S. Qakala, O. Tovide, K. M. Molapo, G. Fomo, C. O. Ikpo, T. Waryo, G. Mbambisa, B. Mpushe, A. Williams, P. G. L. Baker, S. Vilakazi, R. Tshikhudo, and E. I. Iwuoha, " Modulation of the Matrix Effect of Nafion on Tris(bipyridine) ruthenium(II) Electrochemical Probes by Functionalisation with 4-Nitrophenylazo Graphene-Gold Nanocomposite," *Electrochim Acta*, vol. 128, pp. 128–137, 2014.

[117] S. A. Vilekar, I. Fishtik, and R. Datta, "Kinetics of the Hydrogen Electrode Reaction," *Journal of The Electrochemical Society*, vol. 157, no. 7, pp. B1040–B1050, 2010.

[118] J. F. Xie, Y. X. Huang, W. W. Li, X. N. Song, L. Xiong, and H. Q. Yu, "Efficient electrochemical CO_2 reduction on a unique chrysanthemum–like Cu nanoflower electrode and direct observation of carbon deposite," *Electrochimica Acta*, vol. 139, pp. 137–144, 2014.

[119] C. S. Chen, A. D. Handoko, J. H. Wan, L. Ma, D. Ren, and B. S. Yeo, "Stable and Selective Electrochemical Reduction of Carbon Dioxide to Ethylene on Copper Mesocrystals," *Catalysis Science Technology*, vol. 5, no. 1, pp. 161–168, 2015.

[120] M. B. Ross, P. De Luna, Y. Li, C. T. Dinh, D. Kim, P. Yang, and E. H. Sargent, "Designing Materials for Electrochemical Carbon Dioxide Recycling," *Nature Catalysis*, vol. 2, no. 8, pp. 648–658, 2019.

[121] G. Li, T. Yan, X. Chen, H. Liu, S. Zhang, and X. Ma, "Electrode Engineering for Electrochemical CO_2 Reduction," *Energy Fuels*, vol. 36, no. 8, pp. 4234–4249, 2022.

[122] Z. Ma, U. Legrand, E. Pahija, J. R. Tavares, and D. C. Boffito, "From CO_2 to Formic Acid Fuel Cells," *Industrial Engineering Chemistry Research*, vol. 60, no. 2, pp. 803–815, 2021.

[123] C. Oloman and H. Li, "Electrochemical Processing of Carbon Dioxide," *ChemSusChem*, vol. 1, no. 5, pp. 385–391, 2008.

[124] J. T. Billy and A. C. Co, "Experimental Parameters Influencing the Hydrocarbon Selectivity During the Electrochemical Conversion of CO2," *ACS Catalysis*, vol. 7, no. 12, pp. 8467–8479, 2017.

[125] W. Lee, Y. E. Kim, M. H. Youn, S. K. Jeong, and K. T. Park, "Catholyte-Free Electrocatalytic CO2 Reduction to Formate," *Angewandte Chemie*, vol. 130, no. 23, pp. 6999–7003, 2018.

[126] D. Kim, W. Choi, H. W. Lee, S. Y. Lee, Y. Choi, D. K. Lee, W. Kim, J. Na, U. Lee, Y. J. Hwang, and D. H. Won, "Electrocatalytic Reduction of Low Concentrations of CO2 Gas in a Membrane Electrode Assembly Electrolyzer," *ACS Energy Letters*, vol. 6, no. 10, pp. 3488–3495, 2021.

[127] D. S. Ripatti, T. R. Veltman, and M. W. Kanan, “Carbon Monoxide Gas Diffusion Electrolysis That Produces Concentrated C2 Products with High Single-Pass Conversion,” *Joule*, vol. 3, no. 1, pp. 240–256, 2019.

[128] C. Xia, P. Zhu, Q. Jiang, Y. Pan, W. Liang, E. Stavitsk, H. N. Alshareef, and H. Wang, “Continuous Production of Pure Liquid Fuel Solutions via Electrocatalytic CO2 Reduction Using Solid-Electrolyte Devices,” *Nature Energy*, vol. 4, no. 9, pp. 776–785, 2019.

[129] U. Legrand, U.-P. Apfel, D. Boffito, and J. Tavares, “The effect of flue gas contaminants on the CO2 electroreduction to formic acid,” *Journal of CO2 Utilization*, vol. 42, p. 101315, 2020.

[130] M. Kodur, Z. Dorfman, R. A. Kerner, J. H. Skaggs, T. Kim, S. P. Dunfield, A. Palmstrom, J. J. Berry, and D. P. Fenning, “Electrochemical Screening of Contact Layers for Metal Halide Perovskites,” *ACS Energy Letters*, vol. 7, no. 2, pp. 683–689, 2022.

[131] J. Li, A. Ozden, M. Wan, Y. Hu, F. Li, Y. Wang, R. R. Zamani, D. Ren, Z. Wang, Y. Xu, D. H. Nam, J. Wicks, B. Chen, X. Wang, M. Luo, M. Graetzel, F. Che, E. H. Sargent, and D. Sinton, “Silica-Copper Catalyst Interfaces Enable Carbon-Carbon Coupling towards Ethylene Electrosynthesis,” *Nature Communications*, vol. 12, no. 1, p. 2808, 2021.

[132] T. Kim, G. Kim, D. Lee, Y. Kim, S. E. Shim, and S. Baeck, “Electrochemical Oxidation of Organic Matter in the Prepared via Sol–Gel Methods,” *Journal of Nanoscience and Nanotechnology*, vol. 16, no. 10, pp. 1–6, 2016.

[133] X. S. Peng, G. W. Meng, X. F. Wang, Y. W. Wang, J. Zhang, X. Liu, and L. D. Zhang, “Synthesis of Oxygen-Deficient IndiumTin-Oxide (ITO) Nanofibers,” *Chemistry of Materials*, vol. 14, no. 11, pp. 4490–4493, 2002.

[134] J. G. Partridge, M. R. Field, J. L. Peng, A. Z. Sadek, K. Kalantar-zadeh, J. Du Plessis, and D. G. McCulloch, “Nanostructured SnO2 films prepared from evaporated Sn and their application as gas sensors,” *Nanotechnology*, vol. 19, no. 12, p. 125504, 2008.

[135] Z. Wang, Y. Zhou, C. Xia, W. Guo, B. You, and B. Y. Xia, “Efficient Electroconversion of Carbon Dioxide to Formate by a Reconstructed Amino-Functionalized Indium–Organic Framework Electrocatalyst,” *Angewandte Chemie International Edition*, vol. 60, no. 35, pp. 19107–19112, 2021.

[136] S. Zhang, P. Kang, and T. J. Meyer, “Nanostructured Tin Catalysts for Selective Electrochemical Reduction of Carbon Dioxide to Formate,” *Journal of the American Chemical Society*, vol. 136, no. 5, pp. 1734–1737, 2014.

[137] R. Shi, J. Guo, X. Zhang, G. I. N. Waterhouse, Z. Han, Y. Zhao, L. Shang, C. Zhou, L. Jiang, and T. Zhang, “Efficient wettability-controlled electroreduction of CO2 to CO at Au/C interfaces,” *Nature Communications*, vol. 11, no. 1, pp. 1–10, 2020.

[138] M. Alfath and C. W. Lee, “Recent Advances in the Catalyst Design and Mass Transport Control for the Electrochemical Reduction of Carbon Dioxide to Formate,” *Catalysts*, vol. 10, no. 8, p. 589, 2020.